CHAPTER 3

THEORETICAL FRAMEWORK II: DISSOLUTION

"If you wish to make an apple pie from scratch, you must first invent the universe."
—Carl Sagan

The Noyes–Whitney equation, which describes the dissolution phenomena, was introduced more than 100 years ago [1]. Since then, the sciences of dissolution have progressed tremendously. However, there remain many unexplored areas in this field as well. Even though fluid dynamics theories are the basis of dissolution phenomena, they were merely discussed in the textbooks of pharmaceutical sciences. In this section, the sciences of dissolution are discussed using fluid dynamics theories.

Diffusion and convection govern the mass transfer phenomena. From a microscopic viewpoint, diffusion is a random walk process. For example, when a drop of ink is put into a glass of water, it gradually spreads in the water (Fig. 3.1a). After a long time, the solution becomes homogeneous. The same phenomena determines the dissolution of a drug by diffusion (Fig. 3.1b). Even though diffusion is the random walk process, there is a net movement of molecules from a high concentration region to a low concentration region. Therefore, the concentration gradient is often referred to as the *driving force of diffusion* (Fig. 2.8). The diffusion kinetics is described by Fick's laws of diffusion. On the other hand, the convection (flow) also affects the mass transfer. If we stir the water, it becomes homogeneous faster. The motion of a fluid is described by the Navier–Stokes equation.

Biopharmaceutics Modeling and Simulations: Theory, Practice, Methods, and Applications, First Edition. Kiyohiko Sugano.

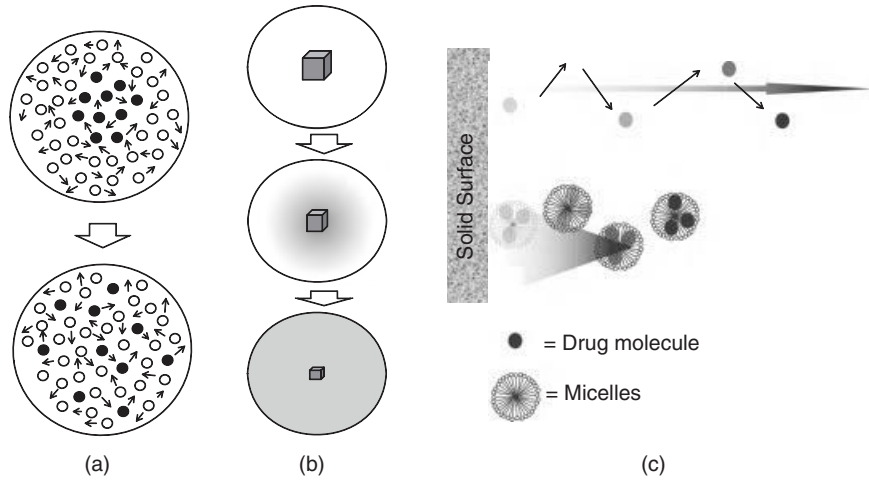

Figure 3.1 Diffusion process. (a) diffusion of a drop of ink, (b) dissolution of a drug under unstirred condition, and (c) diffusion of monomer and bile-micelle drug.

The mass transfer equation is derived from the Fick's laws of diffusion and the Navier–Stokes equation. The derivation of the mass transfer equation from these two equations is found elsewhere (Chapters 1 to 7 of the book "Mass Transfer: Basics and Application" by Kohichi Asano). In this section, we start with the obtained equation and discuss its application in biopharmaceutical modeling. Diffusion coefficient is first discussed, followed by a discussion on the convection process.

3.1 DIFFUSION COEFFICIENT

3.1.1 Monomer

A diffusion coefficient has a dimension of square length per time, for example, square centimeter per second. Several equations have been reported to calculate the diffusion coefficient of a monomer (D_{mono}) in an aqueous media. Avdeef [2] proposed the following equation to calculate the diffusion coefficient of a monomer drug molecule in water at 37 °C.

$$D_{\text{mono}}(\text{cm}^2/\text{s},\ 37\,^{\circ}\text{C}) = 9.9 \times 10^{-5}\ \text{MW}^{-0.453} \tag{3.1}$$

For MW = 350 D_{mono} is calculated to be 7.3×10^{-6} cm^2/s. The average error of this equation is ca. 20%.

When a molecular volume parameter is available, various other methods can also be used, for example, Hayduk and Laudie equation,

$$D_{\text{mono}}(\text{cm}^2/\text{s}, 25^{\circ}\text{C}) = \frac{13.26 \times 10^{-5}}{\eta^{1.4} {v_{\text{B}}}^{0.589}} \tag{3.2}$$

This equation has a 13% error. By using Abraham solute descriptor,

$$\log D_{\text{mono}}(\text{cm}^2/\text{s}, 25^\circ\text{C}) = 0.13 - 0.027\ A_{\text{H}} - 0.36\ V_x \tag{3.3}$$

where A_{H} is the hydrogen-donor strength and V_x is the McGowans molecular volume. Compared to the other drug parameters such as S_0, the estimation error of D_{mono} from the molecular structure is much smaller.

3.1.2 Bile Micelles

The diffusion coefficient of bile-micelles depends on the bile micelle concentration (Fig. 3.2). The diffusion coefficient of bile micelles is ca. 8–80 times smaller than that of a monomer molecule. In the case of taurocholic acid (TC)–egg lecithin (EL) 4:1 system, the bile-micelle diameter (d_{bm}) and diffusion coefficient of bile-micelle-bound drug (D_{bm}) can be predicted as [3, 4]

$$d_{\text{bm}}(\text{nm}) = \frac{700}{-7.90 \times C_{\text{bile}}(\text{mM}) + 37.1} \cdots C_{\text{bile}} \leq 3.98\ \text{mM} \tag{3.4}$$

$$d_{\text{bm}}(\text{nm}) = \frac{1}{0.143 \times C_{\text{bile}}(\text{mM}) - 0.562} + 5.31 \cdots C_{\text{bile}} > 3.98\ \ \text{mM} \tag{3.5}$$

$$D_{\text{bm}}(\text{cm}^2/\text{s}) = \frac{6.63}{d_{\text{bm}}(\text{nm})} \times 10^{-6} \tag{3.6}$$

where C_{bile} is the concentration of TC. For example, for the fasted state simulated intestinal fluid (FaSSIF, TC = 3 mM) [5], $d_{\text{bm}} = 52$ nm and $D_{\text{bm}} = 0.13 \times 10^{-6}$ cm^2/s. It would be worth noting that D_{bm} could be different for each GI (gastrointestinal tract) position or each animal species, depending on the concentration and the composition of bile micelles. Furthermore, as a concentrated bile is diluted,

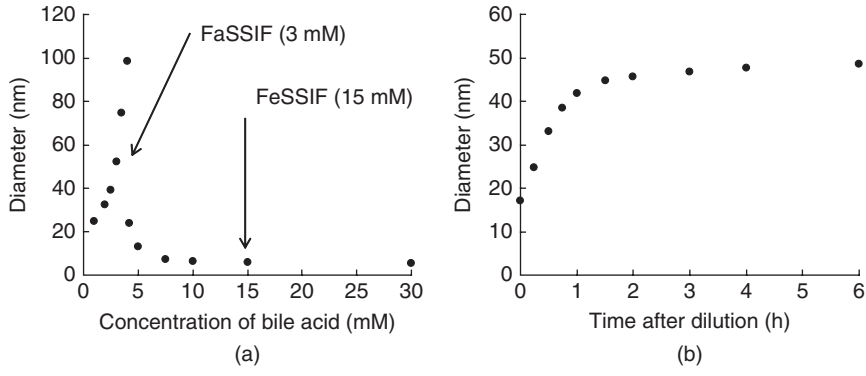

Figure 3.2 (a) Bile-micelle diameter and concentration and (b) time-dependent diameter change after dilution of concentrated FaSSIF (TC = 30 mM).

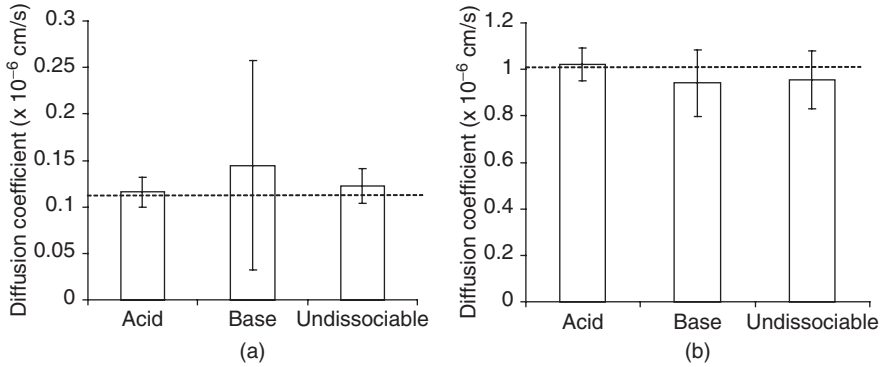

Figure 3.3 Drug inclusion and bile micelle diffusion coefficient. (a) FaSSIF and (b) FeSSIF. Acid: N = 8 drugs. Base: N = 12 drugs. Undissociable N = 23 drugs.

the bile-micelle diameter changes [4]. This dilution process might also occur in the intestine, as the bile secreted from the gall bladder is diluted in the intestine. After dilution of concentrated bile micelles, the micelles transform to liposome-like structures [6]. Okazaki et al. [7] investigated the effect of drug inclusion on the diffusion coefficient of the bile micelles (Fig. 3.3). In the case of some basic compounds, drug inclusion had a large effect on the diffusion coefficient of bile micelles, whereas undissociable and acidic compounds had little effect. Diffusion coefficient of bile micelles can be easily measured by dynamic laser scattering (Section 7.4.3).

When the bile acid concentration is less than 3 mM, the effective diffusion coefficient in the mucus layer was reported to be three times larger compared to that in water [8].

3.1.3 Effective Diffusion Coefficient

The effective diffusion coefficient (D_{eff}) is determined using diffusion coefficients and fractions of monomer and bile-micelle-bound molecules (Fig. 3.1c) [9–14]:

$$D_{\text{eff}} = D_{\text{mono}} f_{\text{u}} + D_{\text{bm}} f_{\text{bm}} \tag{3.7}$$

$$f_{\text{u}} + f_{\text{bm}} = 1 \tag{3.8}$$

where f_{u} and f_{bm} are the fractions of unbound monomer and bile-micelle-bound molecules, respectively.

3.2 DISSOLUTION AND PARTICLE GROWTH

Figure 2.8 shows the schematic representation of dissolution of a solid in a fluid. Two steps are involved in the dissolution from the solid surface. The first step

is the detachment of a molecule from the solid surface. The second step is the diffusion of the detached molecule across the diffusion layer adjacent to the solid surface. In most cases, rapid equilibrium (i.e., saturation) is achieved at the solid surface. Therefore, the second step determines the dissolution rate in most cases.[1] The basic diffusion-controlled model was first described by Noyes and Whitney and later modified by Nernst and Brunner [1].

3.2.1 Mass Transfer Equations: Pharmaceutical Science Versus Fluid Dynamics

The dissolution and particle growth[2] of a drug are the mass transfer from/into the surface of a substance. The mass transfer rate is represented by the Noyes–Whitney equation as[3]

$$\frac{dX_{API}}{dt} = -SA_{API}\, k_{mass} \Delta C \tag{3.9}$$

where X_{API} is the amount of an undissolved API (active pharmaceutical ingredient), SA_{API} is the surface area of the API, k_{mass} is the mass transfer coefficient, and ΔC is the concentration gradient across the diffusion layer.

The difference between the dissolution and growth of particles depends on whether the concentration gradient around the drug particles is positive or negative. The mass transfer coefficient (k_{mass}) is defined as the ratio of diffusion coefficient (dimension: square length per time) to mass transfer resistance, which has a dimension of length.[4] The mass transfer resistance is usually scaled to the representative length (L)[5] of the substance using the Sherwood number (Sh).

$$k_{mass} = \frac{D_{eff}}{L/Sh} \tag{3.10}$$

In pharmaceutical science, the film model has been often used to express the mass transfer (Fig. 3.4) and the mass transfer resistance is represented as the thickness of the film of stagnant layer (h_{API}).

$$k_{mass} = \frac{D_{eff}}{h_{API}} \tag{3.11}$$

[1]This proposition may not be valid for very small particles (e.g., <100 nano scale), as the diffusion resistance (=particle radius) is very small and the diffusion mass transfer process becomes very fast.

[2]Particle growth can occur during the oral absorption process of a free base and salt.

[3]The mass transfer rate per SA is called *flux* (flux $= k_{mass}\Delta C$).

[4]The mass transfer coefficient has the same dimension with permeability (length per time). Both dissolution and passive membrane permeation are governed by the Fick's law.

[5]The representative length is the length of a substance that most largely affects the flow pattern around the substance.

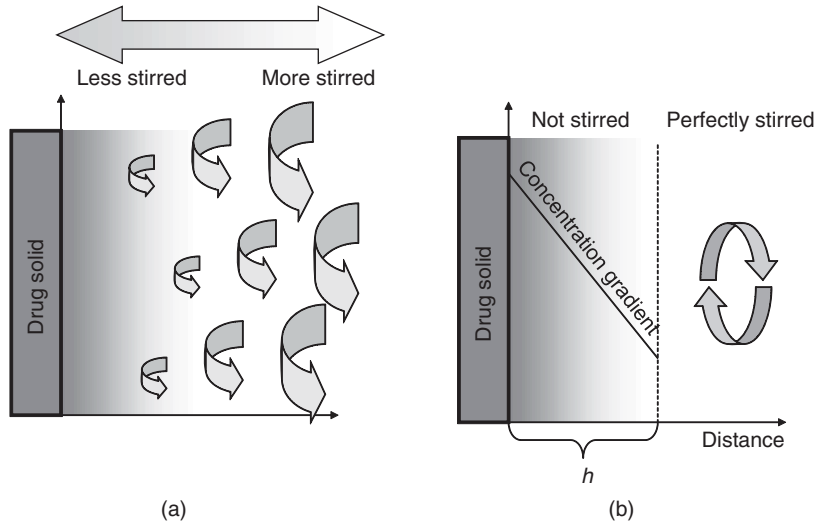

Figure 3.4 (a) Fluid dynamic and (b) pharmaceutical science views for the unstirred water layer.

By comparing Equations 3.10 and 3.11, it is trivial that

$$h_{\mathrm{API}} = \frac{L}{Sh} \tag{3.12}$$

This is the key equation to translate the concept of fluid dynamics to pharmaceutical science. However, as discussed later, several important factors of fluid dynamics are lost in this translation. For example, the effect of fluid viscosity, agitation strength, particle density, and particle shape on the diffusion layer thickness cannot be handled by the pharmaceutical science expression. Therefore, in this book, the fluid dynamical expression of mass transfer is mainly employed.

The mass transfer rate is expressed as

$$\frac{\mathrm{d}X_{\mathrm{API}}}{\mathrm{d}t} = -\mathrm{SA}\frac{D_{\mathrm{eff}}}{L/Sh}\Delta C \tag{3.13}$$

3.2.2 Dissolution Equation with a Lump Sum Dissolution Rate Coefficient (k_{diss})

Before going into the thorough discussions of mechanistic dissolution model equations, to have an overview of the dissolution models, a simple equation using a lump sum dissolution rate coefficient (k_{diss}) is first discussed.

As the SA of particles is a function of the drug amount remaining undissolved, it would be appropriate to speculate that SA is approximately in proportion

to X_{API}. At the beginning of the dissolution, little amount has been dissolved from the particles and X_{API} is close to the initial dose. Therefore,

$$\mathrm{SA} = kX_{\mathrm{API}} = k_{\mathrm{Dose}} \tag{3.14}$$

where k is a coefficient temporary used in this equation. At the initial time of dissolution, the concentration of the fluid is close to 0. Therefore, ΔC can be approximated as

$$\Delta C \approx S_{\mathrm{surface}} \tag{3.15}$$

where S_{surface} is the solubility of a drug at the solid surface. By using Equations 3.14 and 3.15, Equation 3.13 can be rearranged to

$$\begin{aligned}\frac{\mathrm{d}X_{\mathrm{API}}}{\mathrm{d}t} &= -\mathrm{SA}_{\mathrm{API}}\, k_{\mathrm{mass}}\, \Delta C = -k_{\mathrm{Dose}}\, k_{\mathrm{mass}} S_{\mathrm{surface}} \\ &= -k_{\mathrm{Dose}} \frac{D_{\mathrm{eff}}}{h_{\mathrm{API}}} S_{\mathrm{surface}} = -k_{\mathrm{diss}}\, \mathrm{Dose}\end{aligned} \tag{3.16}$$

The lump sum coefficient, k_{diss}, is called the *dissolution rate coefficient*. When an experimental dissolution data is available, k_{diss} can be back calculated from the initial slope of the dissolved drug concentration–time profile. In the following sections, the mechanistic model equations to estimate k_{diss} from the properties of a drug molecule and API are discussed in detail. k_{diss} is the function of solid surface solubility (S_{surface}), diffusion coefficient (D_{eff}), initial particle radius ($r_{\mathrm{p,ini}}$), particle shape, and true density of the drug (ρ_{p}), as well as the agitation strength (ε), viscosity (μ), and density (ρ_{f}) of the fluid. k_{diss} can be calculated from these data (for simple cases, $k_{\mathrm{diss}} = 3D_{\mathrm{eff}} S_{\mathrm{surface}} / {r_{\mathrm{p,ini}}}^2 \rho_{\mathrm{p}}$). However, the estimation errors of each parameter are accumulatively propagated to k_{diss}. Therefore, a direct measurement of this lump sum parameter from a dissolution test is practically useful (Section 8.5.1).

3.2.3 Particle Size and Surface Area

3.2.3.1 Monodispersed Particles. The SA of particles is one of the main determinants of a mass transfer rate from/into particles. We start with the calculation of the SA of a monodispersed particle. The weight of one particle is the product of the volume of one particle (V_{p}) and the particle density (ρ_{p}). The number of particles in a dose (N_{p}) can be calculated by dividing the weight of the dose (Dose) by the weight of one particle. In the case of spherical particles with an initial particle radius ($r_{\mathrm{p,ini}}$), N_{p} can be calculated as

$$N_{\mathrm{p}} = \frac{\mathrm{Dose}}{V_{\mathrm{p}} \rho_{\mathrm{p}}} = \frac{\mathrm{Dose}}{\left(\frac{4}{3}\pi {r_{\mathrm{p,ini}}}^3\right) \rho_{\mathrm{p}}} \tag{3.17}$$

In biopharmaceutical modeling, N_p is operationally set to be unchanged from the initial value, whereas X_{API} and r_p change with the time elapsed. A complete dissolution of a particle is represented by $r_p = 0$ or $X_{API} = 0$.

The SA of one particle (SA_p) with a particle radius (r_p) at time t is

$$SA_p = 4\pi {r_p}^2 \tag{3.18}$$

The total SA at time t is then calculated as the product of the SA of one particle and the number of the particles in the dose. Therefore,

$$SA_{API}(t) = SA_p N_p = 4\pi {r_p}^2 \frac{\text{Dose}}{\left(\frac{4}{3}\pi {r_{p,ini}}^3\right)\rho_p} \tag{3.19}$$

Note that r_p is not the initial particle radius, but the particle radius at time t after dissolution of the particles has occurred ($r_p < r_{p,ini}$).

Especially, at $t = 0$, this equation can be simplified as

$$SA_{API}(t = 0) = \frac{3\text{Dose}}{r_{p,ini}\ \rho_p} \tag{3.20}$$

We can see in this equation that the total SA of a dose is reciprocal to the particle size (Fig. 3.5).

Example The number of particles in 100 mg dose with $\rho_p = 1.2$ g/cm^3, diameter (d_p) = 10 and 1 μm (assuming a spherical particle) can be calculated as follows:

$$SA = \frac{3\text{Dose}}{r_{p,ini}\ \rho_p} = \frac{3 \times 100}{0.0005 \times 1200} = 500 \text{ cm}^2$$

$$SA = \frac{3\text{Dose}}{r_{p,ini}\ \rho_p} = \frac{3 \times 100}{0.00005 \times 1200} = 5000 \text{ cm}^2$$

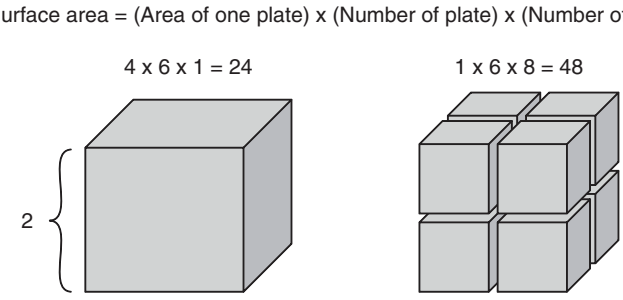

Figure 3.5 Particle size and surface area.

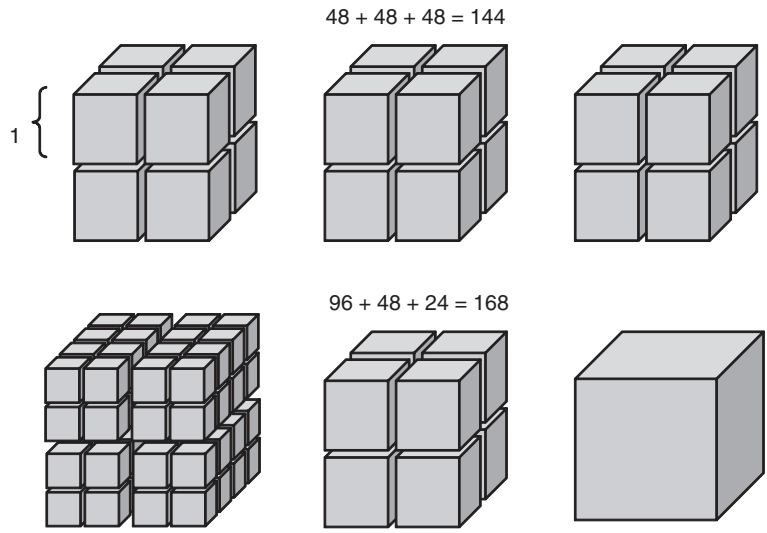

Figure 3.6 Particle size distribution and surface area.

The total SA of a dose can be very large when compared with the intestinal tube SA (the smooth tube-based SA of the entire small intestine is $2 \times 3.14 \times R_{GI}$ (1.5 cm) $\times L_{GI}$ (300 cm) $= 2826\ cm^2$), which is important for the particle drifting effect (Section 4.7.2).

3.2.3.2 Polydispersed Particles. Particle size distribution can be expressed as the volume percentage of each particle size bin (f_{PSB}) with the particle radius ($r_{p,PSB}$)

$$N_{p,PSB} = \frac{f_{PSB}\text{Dose}}{V_p \rho_p} = f_{PSB} \frac{\text{Dose}}{\left(\frac{4}{3}\pi {r_{p,ini,PSB}}^3\right)\rho_p} \tag{3.21}$$

$$\text{SA}(t=0) = \frac{3\text{Dose}}{\rho_p} \sum^{PBS} \frac{f_{PSB}}{r_{p,ini,PSB}} \tag{3.22}$$

As shown in Figure 3.6, as the particle size distribution becomes dispersed, the total SA increases. The effect of the standard deviation of particle size distribution on the SA is shown in Figure 3.7.

3.2.4 Diffusion Layer Thickness I: Fluid Dynamic Model

In this section, the diffusion layer thickness is explained based on fluid dynamics. The advantages of the fluid dynamic model are that the effects of agitation strength, fluid viscosity, and particle density are explicitly taken into

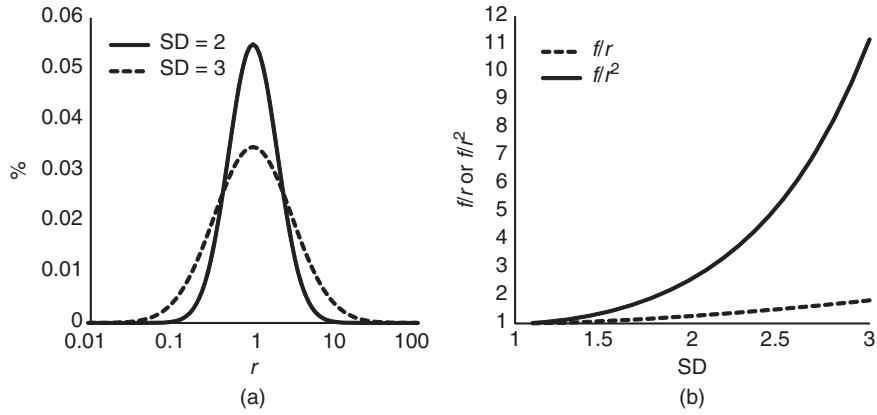

Figure 3.7 (a) Particle size distribution and (b) surface area expansion ratio.

account in the equation, and it offers a scientifically correct understanding of the mass transfer phenomena [15]. However, for most cases, the simple empirical equations, such as the Hintz–Johnson model, would offer practically appropriate accuracy (Section 3.2.5).

3.2.4.1 Reynolds and Sherwood Numbers. The mass transfer resistance around an object has a dimension of length and is usually scaled to the representative length (L) of the object using the Sherwood number (Sh) (Fig. 3.8). The Sherwood number can be calculated from the Reynolds number (Re) and the Schmitt number (Sc) based on the Prandtl's boundary layer theory as

$$Sh \propto Re^{1/2} Sc^{1/3} \tag{3.23}$$

The Reynolds number (Re) is defined as

$$\mathrm{Re} = \frac{U \rho_\mathrm{f} L}{\mu} = \frac{UL}{\nu} \tag{3.24}$$

where U is the flow speed around an object, ρ_f is the density of the fluid, μ is the viscosity of the fluid, and ν is the kinematic viscosity of the fluid ($\nu = \mu/\rho_\mathrm{f}$). The *Re*ynolds number is often used to characterize the flow pattern of a system, namely, "laminar flow" or "turbulence." Re is the ratio of inertia of the flow (the numerator)[6] to the viscosity of the fluid (the denominator). When the viscosity surmounts the inertia ($Re < 1$), the fluid flow around the object becomes laminar, whereas when the inertia surmounts the viscosity ($Re \gg 1000$), the fluid flow becomes turbulent. As Re increases from single digit to 3–6 digit order, the flow regimen gradually changes from laminar to turbulent.

[6]Momentum = speed × weight (weight = density × size)

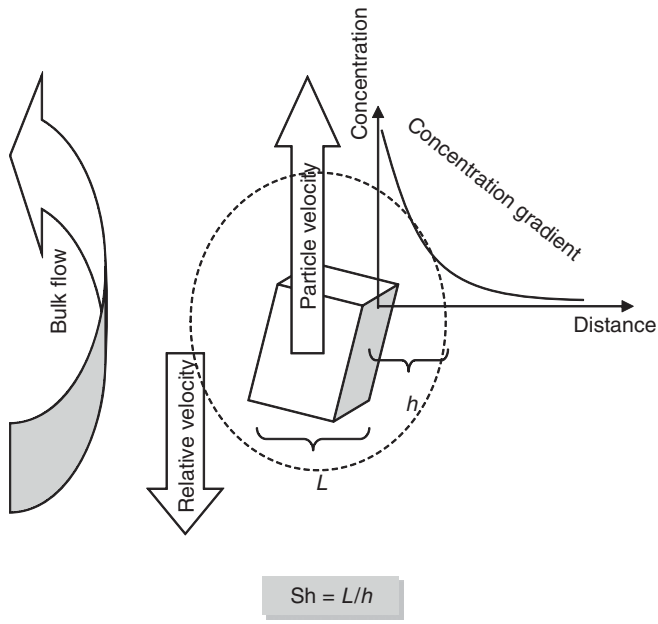

Figure 3.8 Diffusion layer thickness, representative length, and Sherwood number.

Schmidt number (Sc) is defined as the ratio of kinematic viscosity to the diffusion coefficient,

$$Sc = \frac{\nu}{D_{\text{eff}}} \tag{3.25}$$

For example, Sc of a typical drug molecule in water is ca. 1000 (MW = 400, $D_{\text{eff}} = 8 \times 10^{-6}$ cm^2/s, $\nu = 0.007$ cm^2/s in water at 37°C).

By combining Equations 3.23–3.25,

$$Sh \propto Re^{1/2} Sc^{1/3} = \left(\frac{UL}{\nu}\right)^{1/2} \left(\frac{\nu}{D_{\text{eff}}}\right)^{1/3} \tag{3.26}$$

The relationship between Sh, Re, and Sc for various cases are summarized in Table 3.1 and Figure 3.9.

Example The Reynolds number of a column in a water flow can be calculated as follows ($U = 1$ cm/s, $A : L = 1$ cm, $B : L = 10$ μm, $\nu = 0.007$ cm^2/s):

$$Re = \frac{UL}{\nu} = \frac{1 \text{ cm/s} \times 1 \text{ cm}}{0.007 \text{ cm}^2/\text{s}} \approx 143$$

$$Re = \frac{UL}{\nu} = \frac{1 \text{ cm/s} \times 0.001 \text{ cm}}{0.007 \text{ cm}^2/\text{s}} \approx 0.143$$

TABLE 3.1 Summary of Representative Length, Reynolds Number, and Sherwood Number

Object[a]	Representative Length (L)	Reynolds Number (Re)	Mean Sherwood Number (Sh)
Plate in a flow (A)	Plate length (l_{plate})	$Re_{\text{plate}} = \dfrac{Ul_{\text{plate}}}{\nu}$	$Sh_{\text{plate}} = 0.66\, Re_{\text{plate}}^{1/2} Sc^{1/3}$
Rotating disk (B)	Disk diameter (d_{disk})	$Re_{\text{disk}} = \dfrac{\omega d_{\text{disk}}^2}{\nu}$	$Sh_{\text{disk}} = 0.62\, Re_{\text{disk}}^{1/2} Sc^{1/3}$
Cylinder (C)	Cylinder diameter (d_{cylinder})	$Re_{\text{cylinder}} = \dfrac{Ud_{\text{cylinder}}}{\nu}$	$Sh_{\text{cylinder}} = 0.66\, Re_{\text{cylinder}}^{1/2} Sc^{1/3}$
Tube flow (D)	Tube diameter (d_{tube})	$Re_{\text{disk}} = \dfrac{Ud_{\text{tube}}}{\nu}$	$Sh_{\text{tube}} = 1.52\,\text{Gz}^{1/3} = 1.52\left(\dfrac{d_{\text{tube}}}{L_{\text{tube}}}\right)^{1/3} Re_{\text{tube}}^{1/3} Sc^{1/3}$
Sphere in a flow (E)	Sphere diameter (d_{particle})	$Re_{\text{particle}} = \dfrac{Ud_{\text{particle}}}{\nu}$	$Sh_{\text{particle}} = 2 + 0.6\, Re_{\text{particle}}^{1/2} Sc^{1/3}$

[a] The keys are shown in Figure 3.9.

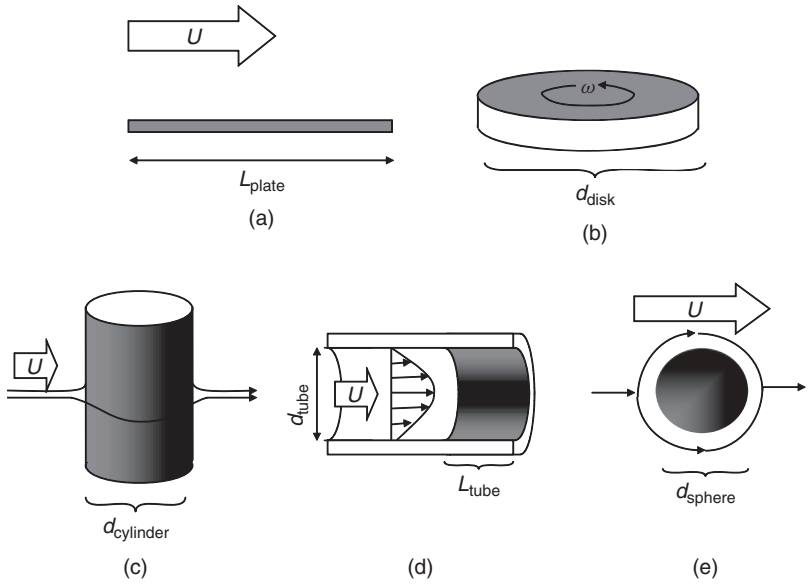

Figure 3.9 Configuration of mass transfer.

The flow pattern behind the column changes from laminar to turbulence via a periodic formation of vortices (Karman's eddy). Even though the two objects are put in the same stream, the flow pattern changes depending on the size of the object. The flow pattern behind the 100 μm object is laminar ($Re = 0.143$). However, behind the 1-cm object ($Re = 143$), periodic formation of vortices is observed. As the Re increases from several hundreds to above several thousands, this periodic vortices transit to turbulent flow.

Similarly, when the GI is considered, the Reynolds number for the drug particles (e.g., $L = r_p = 0.01$ cm) is different for tablets from that of the intestinal tube (for humans, $L = R_{GI} = 1.5$ cm).

3.2.4.2 Disk (Levich Equation). A rotating disk method is often used to measure the intrinsic dissolution rate of a drug (the dissolution rate per SA). The Sherwood number for a rotating disk (Sh_{disk}) is

$$Sh_{disk} \propto {Re_{disk}}^{1/2} Sc^{1/3} = \left(\frac{\pi \mathrm{RPM}/60 \times d_{disk}^2}{\nu} \right)^{1/2} \left(\frac{\nu}{D_{eff}} \right)^{1/3} \tag{3.27}$$

where Re_{disk} is the Reynolds number of a disk, d_{disk} is the disk diameter, and RPM is the rotation speed. Therefore,

$$h_{API} = \frac{d_{disk}}{Sh} \propto \mathrm{RPM}^{-1/2} \nu^{1/6} {D_{eff}}^{1/3} \tag{3.28}$$

This equation is called the *Levich equation*. The disk diameter does not appear in this equation, meaning that it does not affect the thickness of the diffusion layer. Therefore, the intrinsic dissolution rate becomes the same value regardless of the disk diameter. Actually, the μDISS method (3 mm diameter) gave an intrinsic dissolution rate similar to the Wood apparatus method (1 cm diameter) [16]. In the Levich equation, h_{API} is reciprocal of $\mathrm{RPM}^{1/2}$, suggesting that the h_{API} value becomes less sensitive to rotation speed, as it is increased. Therefore, even when the mass transfer rate is not sensitive to an increase in the agitation speed, it cannot be concluded that the diffusion layer is removed. This point is important when analyzing the in vitro permeability data (Section 7.9.8, Fig. 7.33).

3.2.4.3 Tube (Graetz Problem). The mass transfer in the tube with a straight laminar flow (from/into the tube wall) is referred to as the *Graetz problem* (Fig. 3.9d). In this case, the representative length is the tube diameter (d_{tube}). However, the mean Sherwood number is also affected by the tube length (l_{tube}). The Graetz number (Gz) is a dimensionless number, which characterizes the flow pattern in a tube. Equation 3.29 is called the *Leveque equation* and valid at Gz >76. Gz of approximately 1000 or less is the point at which flow would be

considered fully developed for mass transfer.

$$Sh_{\text{tube}} = 1.52\text{Gz}^{1/3} = 1.52\left(\frac{d_{\text{tube}}}{l_{\text{tube}}}\right)^{1/3}\left(\frac{d_{\text{tube}}U}{v}\right)^{1/3}\left(\frac{v}{D_{\text{eff}}}\right)^{1/3} \tag{3.29}$$

Graetz problem has been used to calculate the unstirred water layer thickness in the small intestine (h_{UWL}), especially for the rat in situ perfusion model [17].

3.2.4.4 Particle Fixed to Space (Ranz–Marshall Equation). In the case of the mass transfer from/into the particles, the asymptotic diffusion often becomes significant. The asymptotic diffusion occurs as the concentration gradient is generated by spatial expansion around an object fixed in the space (Fig. 3.10a). The mass transfer by asymptotic diffusion can occur in the absence of flow. The asymptotic diffusion term in Sh for a spherical particle is 2, which can be derived from the concentration gradient around an object induced by spatial expansion (Fig. 3.10a) [detailed derivation of this term is found in Chapters 1 to 7 of the book "Mass Transfer: Basics and Application" by Kohichi Asano]. The effect of convection is then added to the asymptotic diffusion term. The Sherwood number for a spherical particle (Sh_{p}) in a laminar flow is then expressed as

$$Sh_{\text{p}} = 2 + 0.6\,Re_{\text{p}}^{1/2}Sc^{1/3} \tag{3.30}$$

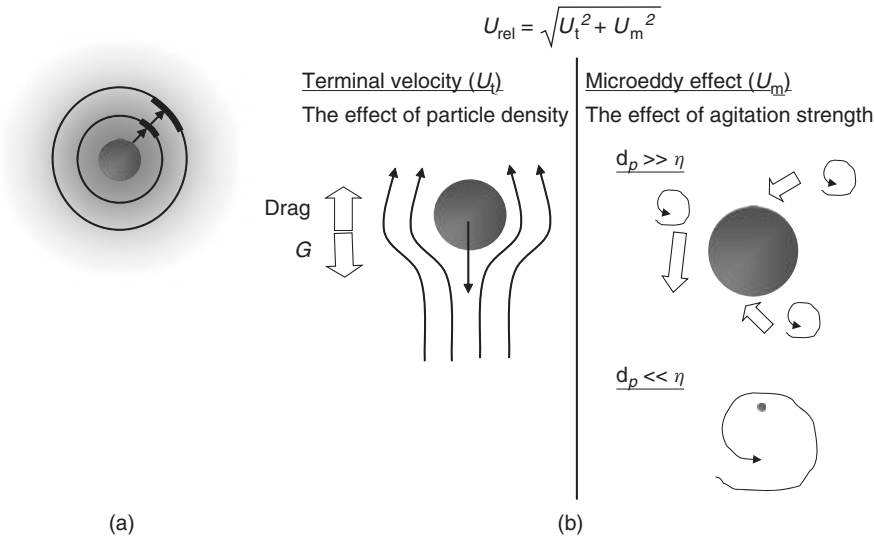

Figure 3.10 A schematic representation of (a) asymptotic diffusion and (b) the terminal sedimentation velocity and microeddy effects.

where Re_p is the Reynolds number of a sphere. This equation is called the *Ranz–Marshall equation*.

Example The Sherwood number and h_{API} of a sphere fixed in space (not freely suspended) in water can be calculated as follows ($U = 0.1$ cm/s, (a) $d_p = 1$ cm, (b) $d_p = 10$ μm, $D_{eff} = 8 \times 10^{-6}$ cm^2/s, $\nu = 0.007$ cm^2/s):

The Sherwood number for a sphere is

$$Sh_p = 2 + 0.6\,Re^{1/2}Sc^{1/3} = 2 + 0.6\left(\frac{Ud_p}{\nu}\right)^{1/2}\left(\frac{\nu}{D_{eff}}\right)^{1/3}$$

Therefore, for particle (a),

$$Sh_p = 2 + 0.6\,Re^{1/2}Sc^{1/3} = 2 + 0.6\left(\frac{1 \times 0.1}{0.007}\right)^{1/2}\left(\frac{0.007}{0.000008}\right)^{1/3} = 18.3$$

$$h_{API} = \frac{L}{Sh} = \frac{d_p}{Sh} = \frac{1}{18.3} = 0.0547 \text{ cm} = 547 \text{ μm}$$

For particle (b),

$$Sh_p = 2 + 0.6\,Re^{1/2}Sc^{1/3} = 2 + 0.6\left(\frac{0.001 \times 0.1}{0.007}\right)^{1/2}\left(\frac{0.007}{0.000008}\right)^{1/3} = 6.09$$

$$h_{API} = \frac{L}{Sh} = \frac{d_p}{Sh} = \frac{1}{6.09} = 0.000164 \text{ cm} = 1.64 \text{ μm}$$

3.2.4.5 Floating Particle. In the above example, the particle is fixed in a space. In this case, the absolute fluid flow equals the flow around the particle. However, in reality, the particles are suspended and float in the fluid when the fluid is agitated. The drug particles move along with the fluid flow in a synchronic manner. In this case, the relative flow velocity ($U_{rel,tot}$) can be approximated as the sum of the terminal sedimentation velocity (U_t) and the microeddy effect velocity (U_e), which is an expedient fluid velocity induced by the microeddy.

$$U_{rel,tot} = \sqrt{U_t^2 + U_e^2} \tag{3.31}$$

The terminal sedimentation velocity is determined as the balance of gravity, buoyancy, and frictional resistance. A schematic representation of the terminal sedimentation velocity is shown in Figure 3.10b. The U_t of a spherical particle can be calculated as

$$U_t = \left(\frac{4(\rho_p - \rho_f)d_p g}{3\rho_f} \times \frac{1}{C_D}\right)^{1/2} \tag{3.32}$$

where g is the gravitational acceleration constant and C_D is the resistance coefficient from the fluid.

When $Re_p < 0.3$, C_D of a spherical particle can be derived from the Navier–Stokes equation with Stokes approximation as

$$C_D = \frac{24}{Re_p} \tag{3.33}$$

$$U_t = \frac{(\rho_p - \rho_f){d_p}^2 g}{18\mu} \tag{3.34}$$

When $Re_p > 0.3$, C_D can be approximated as [18]:

$$C_D = \left(\left(\frac{A}{Re_p}\right)^{1/m} + B^{1/m}\right)^m \tag{3.35}$$

$$U_t = \frac{\nu}{d_p}\left(\sqrt{\frac{1}{4}\left(\frac{A}{B}\right)^{2/m} + \left(\frac{4}{3}\times\frac{{d_{p^*}}^3}{B}\right)^{1/m}} - \frac{1}{2}\left(\frac{A}{B}\right)^{1/m}\right)^m \tag{3.36}$$

$$d_{p^*} = \left(\left(\frac{\rho_p}{\rho_f} - 1\right)\times g \times \left(\frac{1}{\nu}\right)^2\right)^{1/3} d_p \tag{3.37}$$

Various A, B, and m values have been reported depending on the Re_p range and particle shape. $A = 20.5$, $B = 0.310$, and $m = 2.07$ were used for spherical particles in the previous investigation [19].

The flow velocity from the microeddy effect can be calculated as [20, 21]:

$$U_e = 0.195 \times d_p^{1.1}\varepsilon^{0.525}\mu^{-0.575} \tag{3.38}$$

$$\varepsilon = \frac{P_N\rho_f \times \mathrm{RPM}^3 \times {D_{\mathrm{paddle}}}^5}{V} \tag{3.39}$$

where ε is the energy dissipation of turbulence and D_{paddle} is the paddle diameter. The microeddy effect is related to the turbulence and Kolmogorov's minimum eddy scale (η).

$$\eta = \left(\frac{\nu^3}{\varepsilon}\right)^{1/4} \tag{3.40}$$

For example, η is ca. 100 μm for the USP paddle method with 50 rpm ($\varepsilon = 0.004$ m^2/s^3). A schematic representation of the microeddy effect is shown in Figure 3.10b. Particles smaller than this scale are involved within this eddy

(so the flow around the particle looks laminar), whereas for a particle larger than this scale, the eddies agitate the fluid near the surface.

For both terminal velocity and microeddy effects, when the particle size is small, the Reynolds number becomes small and the second term of the Ranz–Marshall equation becomes negligible (both U_t and U_e is negligible). Therefore, for the small particles ($d_p < 60$ μm), the contribution of asymptotic diffusion term becomes predominant and the Sherwood number becomes approximately 2 (for the USP paddle method with <100 rpm). Therefore, h_{API} becomes the radius of the particle ($h_{API} \approx d_p/Sh = r_p$) [19, 22]. This theoretically underwrites the well-known empirical rule in pharmaceutical sciences that h_{API} is close to the particle radius and the agitation strength has little effect on the dissolution rate of small particles. This theory of $h_{API} \approx r_p$ is validated down to 100 nm particles [23].

For coarse particles ($d_p > 60$ μm), h_{API} depends on the agitation strength and the density of particles. As the agitation strength becomes larger, the microeddy effect becomes larger, h_{API} becomes thinner, and the dissolution rate becomes faster. As the true density becomes larger, the terminal sedimentation velocity becomes larger, h_{API} becomes thinner, and the dissolution rate becomes faster. The particle size affects both U_t and U_e. Interestingly, as the result of considering these factors, h_{API} becomes relatively constant (ca. 30 μm) regardless of the particle size (Fig. 3.13).

Equations 3.31–3.40 are an open analytical solution, so that it can be used for biopharmaceutical modeling without slowing down the computational speed. However, the true density of a drug is in the 1.1–1.5 range in most cases and the agitation strength is 10–100 rpm. Therefore, a simple empirical equation with a fixed maximum $h = 30$ μm value would be appropriate for most cases (Section 3.2.5).

3.2.4.6 Nonspherical Particle. In the case of nonspherical particles, the asymmetric term in the Ranz–Marshall equation deviates from 2. It is convenient to introduce a shape factor (Π), which has a dimension of length.

$$\Pi = Sh_{particle}\frac{SA_p}{L} \tag{3.41}$$

In Table 3.2, equations for several particle shapes are shown. However, in most cases, the particle shape is not exactly the same with those listed shapes in the table. For irregularly shaped particles, it is also convenient to use the simple approximation as

$$\Pi = 5.25\,SA_p{}^{1/4}V_p{}^{1/6} \tag{3.42}$$

where V_p is the volume of the particle. Figure 3.11 shows the ratio of the SA and dissolution rate by asymptotic diffusion for a cylindrical particle having a volume equivalent to a sphere. As the shape of a particle deviates from the sphere, the SA and dissolution rate increases. However, the extent of increase in the dissolution

TABLE 3.2 Shape Factor for Irregular Particles

Shape of the Particle	Shape Factor $\Pi = Sh\dfrac{SA}{L}$
Sphere of diameter, d	$2\pi d$
Circular cylinder of a diameter d and length L $(0 < L/d < 8)$	$\left[8 + 4.1\left(\dfrac{2L}{d}\right)^{0.76}\right]\dfrac{d}{2}$
Cube with edge, L	$0.654(2\pi L)$
Thin rectangular plate with sides L_1 and L_2 $(L_1 > L_2)$	$\dfrac{2\pi L_1}{\ln(4L_1/L_2)}$

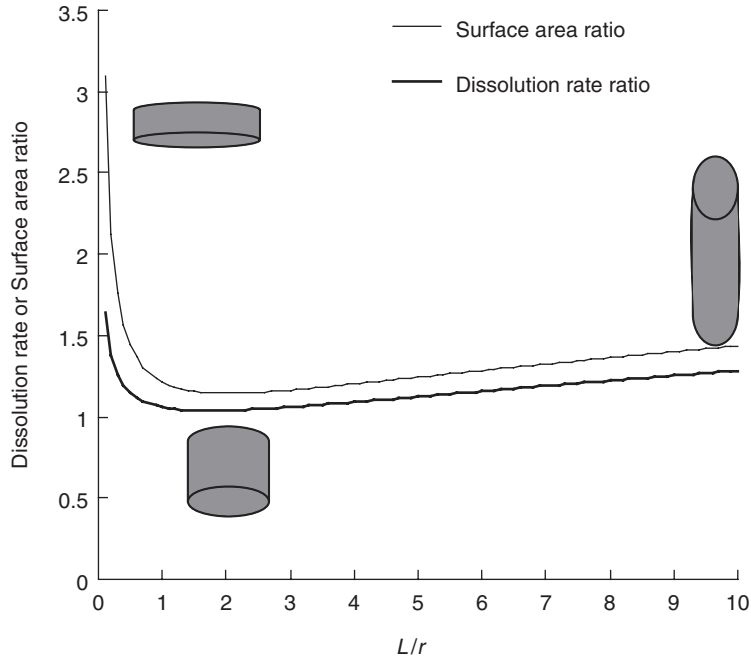

Figure 3.11 Ratio of the surface area to the dissolution rates by asymptotic diffusion for a cylindrical particle having a volume equivalent to a sphere. *Source:* Adapted from Reference 15 with permission.

rate is smaller than that in the SA. According to Equation 3.42, the dissolution rate remains within 2-fold of the spherical particle of the same volume even when the SA is increased by 16-fold. In other words, even when the particle shape deviates from spherical, the boundary layer on the particle remains (semi-) spherical and the effectiveness of SA expansion on the dissolution rate is masked

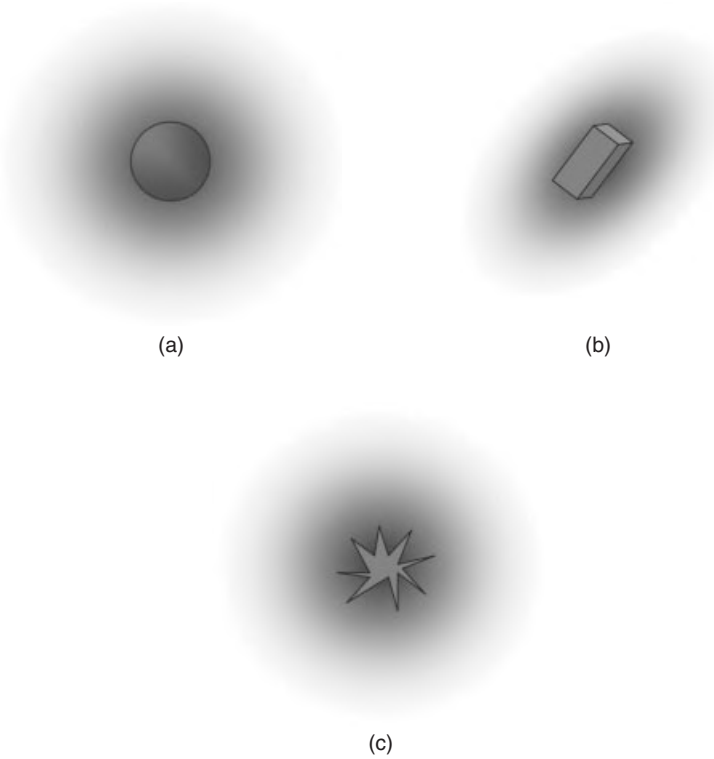

Figure 3.12 Particle shape and asymptotic diffusion. *Source:* Adapted from Reference 15 with permission.

by this semispherical diffusion layer (Fig. 3.12). This theoretically underwrites that the use of spherical approximation is appropriate for most cases.

3.2.4.7 Minimum Agitation Speed for Complete Suspension. When the terminal velocity of particles is larger than the upward flow in a system, the particles would sediment down on the bottom of a flask or the wall of the intestine. The flow around sediment particles is significantly different from that of suspended particles. In this case, estimation of the Sherwood number would be more complicated, especially when the particles are close and affect the flow pattern of each other. A simple equation for this case has not been reported yet.

For a vessel with a paddle, an equation to estimate the minimum agitation speed (RPM_{min}) for complete suspension of spherical particles was reported [24]. The general form of this equation is

$$RPM_{min} = a\left(\frac{D_{vessel}}{D_{paddle}}\right)^{b} \exp\left(c\frac{H_{paddle}}{D_{vessel}}\right) \frac{\left(\frac{\mu_f}{\rho_f}\right)^{0.1} {d_p}^{0.2}}{{D_{paddle}}^{0.85}}$$

$$\times \left(g \frac{\rho_p - \rho_f}{\rho_f} \right)^{0.45} \quad \text{for} \quad \frac{H_{paddle}}{D_{vessel}} > 1.5 \tag{3.43}$$

where D_{vessel} is the diameter of the vessel and H_{paddle} is the height of the paddle from the bottom. The coefficient a, b, and c were estimated to be 104.4, 1.18, and 0.41, respectively. For example, using the geometry of the compendium dissolution test, RPM_{min} for a particle with $d_p = 300$ μm and $\rho_p = 1.2$ g/cm^3 is calculated to be 53. Therefore, a particle larger than 300 μm would form a coning on the bottom of the vessel. However, the coefficients a, b, and c should be fine-tuned for the configuration of compendium paddle methods.

For the small intestine, it is difficult to estimate the critical particle size for complete suspension. For small particles ($d_p < 60$ μm), the dissolution rate would not be affected whether they are suspended or not, as the asymptotic diffusion dominates the dissolution rate. However, for large particles ($d_p > 60$ μm), it would affect the dissolution rate. The $h_{API} = r_p$ assumption tends to give appropriate or over prediction of in vivo oral absorption for many cases ($d_p > 100$ μm), suggesting that the particles may be settling down near the intestinal wall [25] (Section 8.5.2). For more precise biopharmaceutical modeling, it is critically important to improve our understanding about the flow patterns in the GI tract, especially near the boundary layer of the intestinal wall.

3.2.4.8 Other Factors. By using the fluid dynamic expression, the effect of fluid viscosity and density can be also taken into account. The Ranz–Marshall equation itself is validated in the chemical engineering area. However, literature information for a pharmaceutical application is sparse. Recently, the effect of fluid density was suggested to be important for the dissolution of lidocaine [26].

3.2.5 Diffusion Layer Thickness II: Empirical Models for Particles

Several empirical approximate equations have also been proposed to calculate the thickness of the diffusion layer on suspended particles in the USP paddle method. Hintz and Johnson [27] proposed an empirical equation (HJ model).

$$h_{API} = r_p, \quad r_p < h_{c,HJ} \tag{3.44}$$

$$h_{API} = h_{c,HJ}, \quad r_p > h_{c,HJ} \tag{3.45}$$

Wang and Flanagan [28, 29] proposed a semiempirical equation based on the film model with a spherical particle (WF model).

$$\frac{1}{h_{API}} = \frac{1}{r_p} + \frac{1}{h_{c,WF}} \tag{3.46}$$

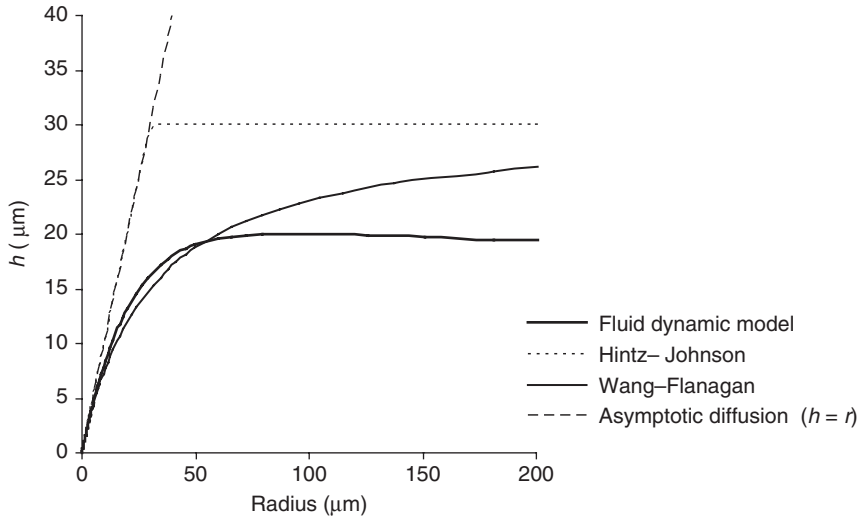

Figure 3.13 Comparison of HJ, WF, and the fluid dynamic models.

Figure 3.13 shows the comparison of HJ, WF, and the fluid dynamic models. Both $h_{c,HJ}$ and $h_{c,WF}$ are set to 30 μm, which is most often used in biopharmaceutical modeling (in the original paper, $h_{c,WF}$ was reported to be 110 μm). For the HJ model, $h_{c,HJ} = 20$ μm would result in a similar plot with the fluid dynamic model. As discussed in the previous sections, from a theoretical perspective, these simple empirical rules would have appropriate accuracy (less than twofold error) for most cases, except for a large and significantly irregular particle (aspect ratio >10) in a strong agitation condition. It should be noted that $h_{c,HJ}$ and $h_{c,WF}$ of 30 μm are for completely suspended particles but not for sediment particles.

3.2.6 Solid Surface pH and Solubility

In the case of dissociable drugs, the solid surface pH can be significantly different from the bulk fluid pH because of the buffering effect of the API. This effect can be significant especially for the dissolution of a free base in the stomach (Section 8.6) [30].

In the case of free acids or bases, chemical reactions occur within the diffusion layer. Therefore, the microclimate pH at the solid surface ($p[H^+]_0$) does not become equal to that in the bulk medium, and the solid surface solubilities ($S_{surface}$) of free acids and bases become smaller than the solubility of a drug in the bulk media ($S_{dissolv}$) (Figs. 3.14 and 3.15). The $p[H^+]_0$ can be obtained by solving the following third-degree equation (the Newton method can be used) [31, 32]:

$$pX^3 + qX^2 + rX + s = 0 \tag{3.47}$$

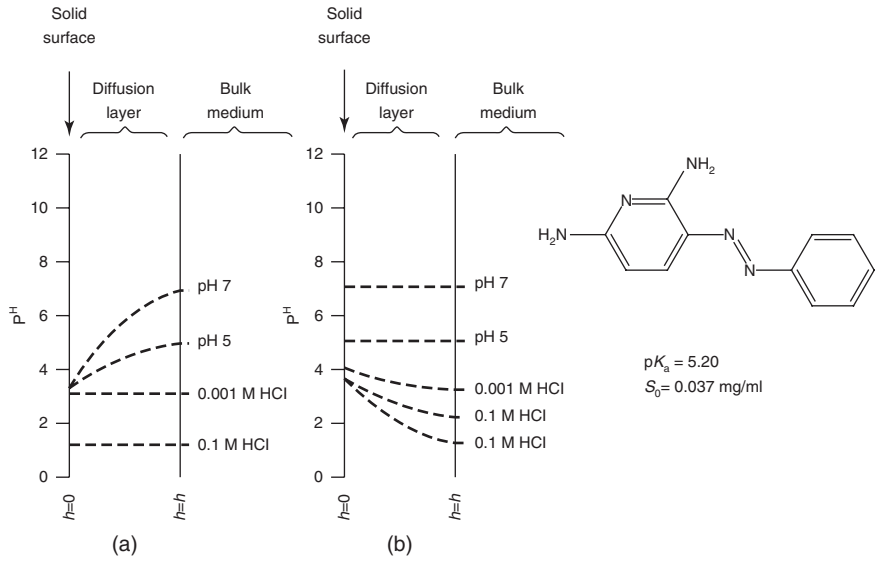

Figure 3.14 Schematic representation of the buffering effect of (a) phenazopyridine HCl and (b) phenazopyridine free base in the diffusion layers of various media. *Source:* Adapted from Reference 33 with permission.

$$p = D_{\mathrm{w}} D_{\mathrm{buf,conj}} K_{\mathrm{a,buf}}^{-I} \sqrt{K_{\mathrm{w}}^{1-I}} \tag{3.48}$$

$$q = D_{\mathrm{w}} D_{\mathrm{buf,unconj}} \sqrt{K_{\mathrm{w}}^{1-I}} + I \times D_{\mathrm{buf,conj}} K_{\mathrm{a,buf}}^{-I} \left(D_{\mathrm{OH}} [\mathrm{OH}^-]_{\mathrm{bulk}} + D_{\mathrm{buf,unconj}} [\text{buf unconj}]_{\mathrm{bulk}} - D_{\mathrm{H}} [\mathrm{H}^+]_{\mathrm{bulk}} \right) \tag{3.49}$$

$$r = I \times D_{\mathrm{buf,unconj}} K_{\mathrm{a,buf}}^{-I} \left(D_{\mathrm{OH}} [\mathrm{OH}^-]_{\mathrm{bulk}} - D_{\mathrm{buf,conj}} [\text{buf conj}]_{\mathrm{bulk}} - D_{\mathrm{H}} [\mathrm{H}^+]_{\mathrm{bulk}} \right) - I \times D_{\mathrm{drug}} D_{\mathrm{buf,conj}} S_0 \left(\frac{K_{\mathrm{a,drug}}}{K_{\mathrm{a,buf}}} \right)^{-I} - D_{\mathrm{w'}} D_{\mathrm{buf,conj}} K_{\mathrm{a,buf}}^{-I} \sqrt{K_{\mathrm{w}}^{1-I}} \tag{3.50}$$

$$r = -D_{\mathrm{w'}} D_{\mathrm{buf,unconj}} \sqrt{K_{\mathrm{w}}^{1-I}} - I \times D_{\mathrm{drug}} D_{\mathrm{buf,unconj}} S_0 K_{\mathrm{a,drug}}^{I} \tag{3.51}$$

$$I = 1, X = [\mathrm{H}^+]_0, W = \mathrm{H}, W' = \mathrm{OH} \quad \text{for free acid}$$

$$I = -1, X = [\mathrm{H}^+]_0^{-1}, W = \mathrm{OH}, W' = \mathrm{H} \quad \text{for free base} \tag{3.52}$$

where D_{N} is the diffusion coefficient of species, N. $[\mathrm{N}]_{\mathrm{bulk}}$ can be calculated from the pH of the bulk and the concentration of the buffer species (e.g., in the

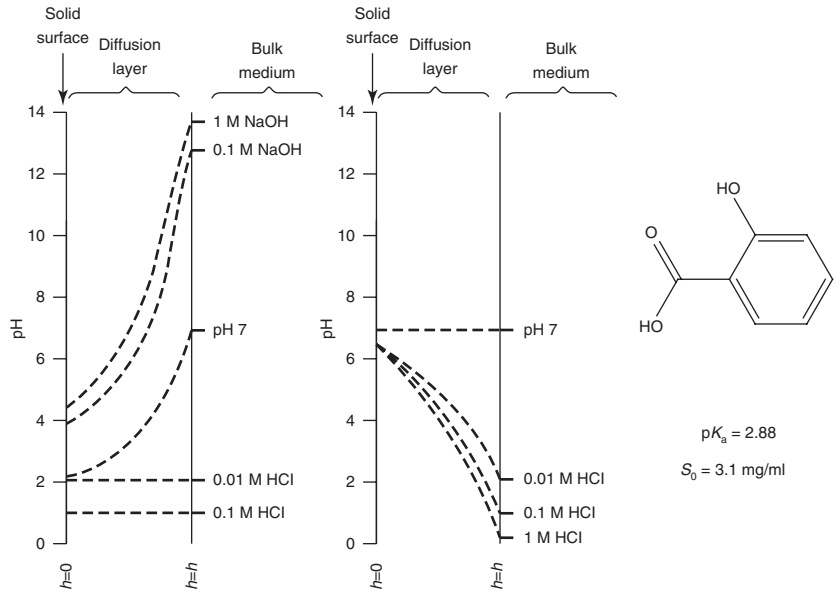

Figure 3.15 Schematic representation of the buffering effect of (a) salicylic acid and (b) sodium salicylate in the diffusion layers of various media. *Source:* Adapted from Reference 34 with permission.

case of the sodium acetate buffer, acetic acid + acetate). The "buf,conj" and "buf,unconj" are the buffer species conjugated and unconjugated to the free acid or base, respectively. For example, for an acetate buffer, "buf,conj" is acetate (CH_3COO^-) and "buf,unconj" is acetic acid (CH_3COOH). For an imidazole buffer, "buf,conj" is free imidazole and "buf,unconj" is protonated imidazole. Once $[H^+]_0$ (pH at the solid surface) is obtained, $S_{surface}$ can be calculated from the theoretical pH–solubility curve as described in Section 2.3.

The pH at the solid surface is affected by the buffer concentration ($[buf,conj]_{bulk}$ and $[buf,unconj]_{bulk}$). Usually, the buffer capacity used for a dissolution test is significantly higher than that observed in the physiological condition. Therefore, the self-buffering effect by a free drug (free acid or base) at the solid surface can be underestimated in the dissolution test [35].

Figure 3.16 shows the effect of pK_a and intrinsic solubility on the solid surface pH for a base drug at pH 1.5 (representing the stomach pH).

To incorporate the solid surface solubility, the Nernst–Brunner equation can be modified as [3]:

$$\frac{dX_{API}}{dt} = -SA \times k_{mass} S_{surface} \left(1 - \frac{C_{dissolv}}{S_{dissolv}}\right) \tag{3.53}$$

This is an approximate equation to simultaneously satisfy the initial dissolution rate and maximum $C_{dissolv}$ in the GI tract.

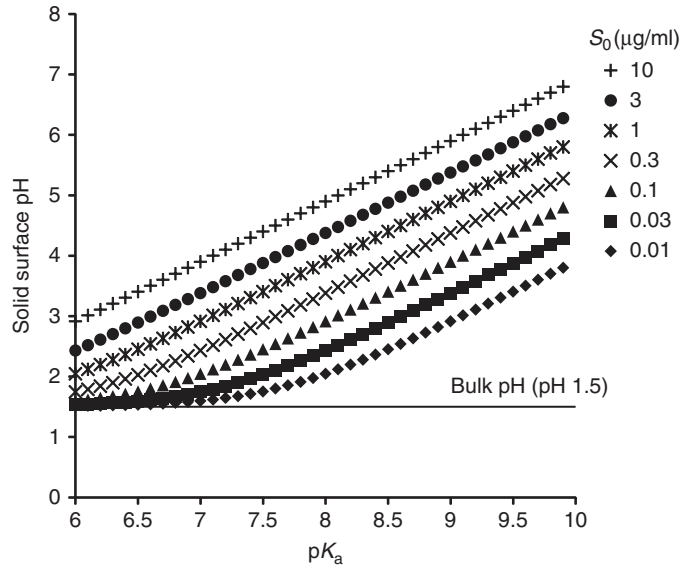

Figure 3.16 Effect of pK_a and intrinsic solubility on the solid surface pH for a free base with MW = 400 and $D_{mono} = 7 \times 10^{-6}$ cm/s at bulk pH 1.5 (with no buffer). *Source:* Calculated based on Reference 31.

3.3 NUCLEATION

In the cases the initial API form converts to another solid form during the oral absorption processes, the nucleation process of a new form has to be taken into account in biopharmaceutical modeling. The examples of API form conversions are as follows:

- salt form to free form (Fig. 3.17)[7]
- amorphous form to crystalline form
- cocrystalline form to free form
- anhydrate form to hydrate form

3.3.1 General Description of Nucleation and Precipitation Process

Figure 3.18 shows the schematic representation of a dissolution time course for a salt of a base drug (see also Figure 11.1). As the salt dissolves ①, the dissolved drug concentration increases. Even after exceeding the saturated solubility of a free base ②, the precipitation of a free base does not occur at this point because the concentration of the free base is not sufficient to induce a significant nucleation speed (in the time scale of oral absorption). As the concentration

[7]The solid form of a precipitant from the supersaturated solution is not necessarily crystalline but can be amorphous (cf. the Ostwald rule of stage).

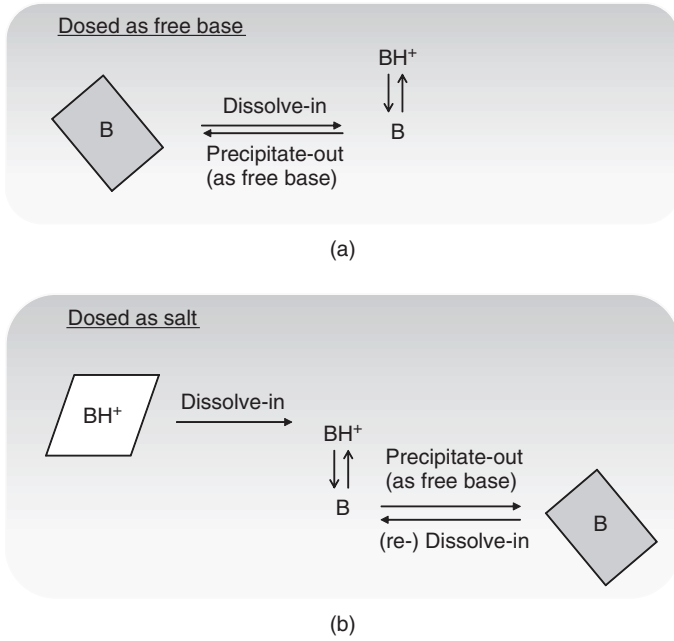

Figure 3.17 (a) Identical form precipitation and (b) different form precipitation.

of the dissolved free base increases, it then reaches the critical supersaturation concentration ③.[8] At this point, nucleation of embryo of free base particles reaches a significant speed. After nuclei are generated, the nuclei particles start to grow, bringing the dissolved free base from the solution to the free base particles ④. This particle growth is the reverse reaction of dissolution. The particle growth continues until the dissolved drug concentration reaches the equilibrium solubility of the free base ⑤.

Because the particle growth process ④ and ⑤ can be expressed by the Noyes–Whitney equation as discussed in the previous section, we focus on the mechanism of the nucleation process in this section.

3.3.2 Classical Nucleation Theory

At present, the nucleation mechanism of a drug in the GI tract are not well understood. However, as the starting point, the classical nucleation theory (CNT) can be used to simulate precipitation in biopharmaceutical modeling [3, 36]. The theory described in this section does not consider other factors such as secondary nucleation and aggregation.

[8]This may not occur when the dose number based on the critical supersaturation concentration is less than 1 or when the intestinal membrane permeation clearance rapidly removes the dissolved drug from the intestinal fluid.

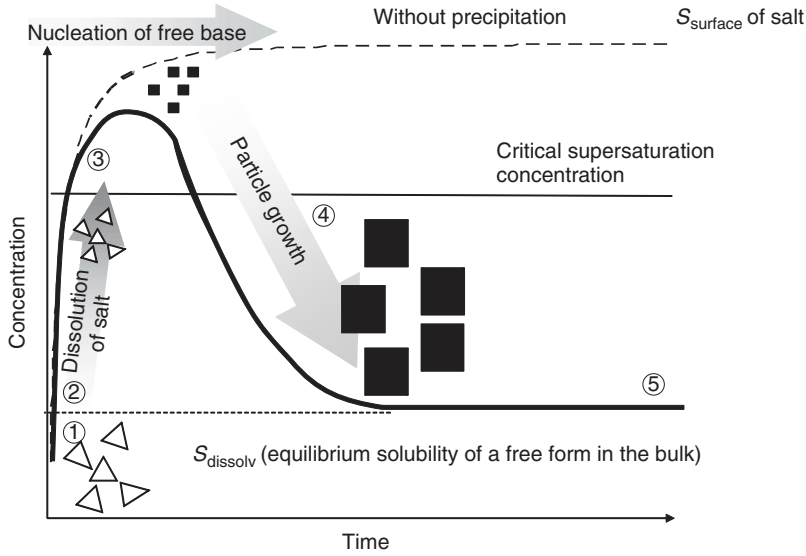

Figure 3.18 Dissolution of a salt and nucleation and particle growth of a free form.

3.3.2.1 Concept of Classical Nucleation Theory. The drug molecules dissolved in a fluid can form agglomers (clusters) (Fig. 3.19). The clusters are in a dynamic equilibrium. The population of each cluster is described by the Boltzmann distribution. Even when the vast majority of the drug molecules exist as a monomer, a very small portion of the molecules can exist as clusters (cf. the Avogadro number is 6.022×10^{23} mol^{-1}). A molecule associates or dissociates to a cluster to form larger or smaller clusters. The critical cluster size at which the growth of the cluster becomes energetically favored depends on the free energy barrier to form the cluster. When the cluster size is smaller than the critical size, the increase in the interfacial energy ($\propto r^2$) by adding one molecule is larger than the decrease in the volume energy ($\propto r^3$). Therefore, in this case, the growth of the cluster is not favored and the cluster cannot grow further. Once the critical size is achieved, the growth of the cluster becomes energetically favored and the nuclei particle continues to grow.

3.3.2.2 Mathematical Expressions. According to the CNT, the primary nucleation rate per volume per time (J_{nc}) can be expressed as

$$\begin{aligned} J_{nc} &= \frac{dN_n}{dt} \\ &= (\text{number of critical cluster}) \\ &\quad \times (\text{frequency of addition of another molecule}) \\ &= C_{nc} \times F_{cn} \end{aligned} \tag{3.53}$$

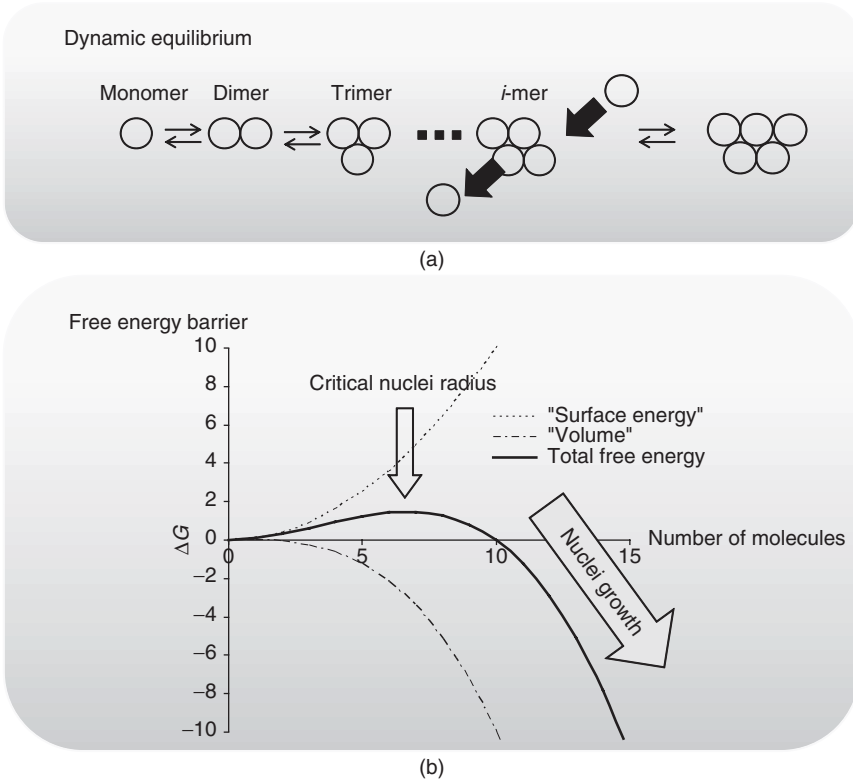

Figure 3.19 Free energy barrier for nucleation.

where N_n is the number of nuclei per volume, C_{nc} is the number of critical cluster per volume, and F_{cn} is the frequency of addition of another molecule to the critical cluster. C_{nc} is determined by the energy barrier for nucleation (ΔG_{nc}) as

$$C_{nc} = (N_A \times C_0) \exp\left(-\frac{\Delta G_{nc}}{k_B T}\right) Z_{ch} \tag{3.54}$$

where N_A is the Avogadro number, C_0 is the concentration of free monomer (mol/l), k_B is the Boltzmann constant, T is the temperature, and Z_{ch} is the Zel'dovich number. $N_A C_0$ is the concentration as the number of molecules per volume. ΔG_{cn} is expressed as (spherical nuclei assumed)

$$\Delta G_{cn} = \frac{16\pi\gamma^3 {v_m}^2}{3 \cdot (k_B T \times \ln(C_b/S_0))^2} \tag{3.55}$$

where γ is the surface energy and v_m is the molecular volume. Z_{ch} is expressed as

$$Z_{ch} = \frac{(k_B T)^{3/2} (\ln(C_0/S_0))^2}{8\pi\gamma^{3/2} v_m} \tag{3.56}$$

The frequency of collision is determined by the critical radius of nuclei ($r_{p,nc}$), D_{mono}, and the interfacial reaction rate correction factor (Ψ_{cn}) as

$$\begin{aligned} F_{cn} &= (\text{Surface area}) \times (\text{Collision rate per area}) \times (\text{Concentration}) \\ &= 4\pi {r_{p,nc}}^2 \times \frac{\varphi_{nc} D_{mono}}{r_{p,nc}} \times N_A C_0 \end{aligned} \tag{3.57}$$

$$r_{p,nc} = \frac{2\gamma v_m}{k_B T \times \ln(C_0/S_0)} \tag{3.58}$$

$$\varphi_{nc} = \frac{h_{pUWL}}{\lambda_{nc} + h_{pUWL}} \tag{3.59}$$

where λ_{nc} represents the contribution of interfacial attachment rate as the length dimension. If the interfacial association is faster than the diffusion, $r_{p,nc} \gg \lambda_{nc}$ and $\Psi_{nc} = 1$. By combining Equations 3.52–3.59

$$J_{nc} = \varphi_{prec,k} D_{mono} (N_A C_0)^2 \left[\frac{k_B T}{\gamma}\right]^{1/2} \ln(C_0/S_0) \exp\left(-\frac{16\pi}{3}\left(\frac{\gamma}{k_B T}\right)^3 \left(\frac{v_m}{\ln(C_0/S_0)}\right)^2\right) \tag{3.60}$$

The nucleation rate depends very steeply on C_0/S_0. C_0/S_0 represents the degree of supersaturation. The C_0/S_0 value that gives $J_{nc} \approx 1$ in the time scale of interest is defined as the *critical supersaturation ratio* (CSSR).[9] CSSR is mainly determined by γ. No nucleation occurs where $C_0/S_0 <$ CSSR in the time scale of interest. The concentration range of $S_0 < C_0 < S_0 \times$ CSSR is called the *metastable zone*.

Equation 3.60 is the theoretical equation for homogeneous precipitation. However, usually heterogeneous precipitation is more popular. In addition, γ is difficult to obtain. For heterogeneous nucleation, the lump constant (β) of the foreign particle number, sticking provability, and an apparent surface energy (γ') are introduced [37]:

$$J_{nc} = \beta D_{mono} (N_A C_0)^2 \left[\frac{k_B T}{\gamma'}\right]^{1/2} \ln(C_0/S_0) \exp\left(-\frac{16\pi}{3}\left(\frac{\gamma'}{k_B T}\right)^3 \left(\frac{v_m}{\ln(C_0/S_0)}\right)^2\right) \tag{3.61}$$

[9]CSSR depends on the time scale. Even when the degree of supersaturation is small, after a long time elapse, nucleation occurs. This time lag is called *induction period*. This induction period is a probabilistic process that would follow the Boltzmann distribution.

where β and γ' are the drug parameters for heterogeneous nucleation. The γ' value is very difficult to measure and is usually not available during drug discovery. Therefore, it would be practical to estimate γ' from a measured CSSR value. Another unknown drug parameter, λ_{prec} can be obtained from the particle growth rate of seeded nuclei in the metastable zone [38]. The γ' and β values can be obtained by simulation fitting to in vitro precipitation experiment data, which mimics the fluid transfer from the stomach to the small intestine.

3.3.3 Application of a Nucleation Theory for Biopharmaceutical Modeling

The nucleation rate in each GI position can be calculated using a nucleation theory. Once the size and number of nuclei are calculated, a virtual particle bin can be assigned with the information of the position of the nuclei in the GI tract and the nuclei radius. The particle growth can then be calculated using the Noyes–Whitney equation with a negative concentration gradient. These mechanisms automatically give the particle size distribution of the precipitant. This particle size distribution data can then be used to calculate the redissolution of the precipitant in the GI tract.

Therefore, to represent the process of salt dissolution and free-form precipitation, we need two Noyes–Whitney equations, one for the dissolution of a salt API and the other for the particle growth and redissolution of the free base precipitant. For the dissolution of a salt, $S_{surface}$ and $S_{dissolv}$ can be set to the solubility of the salt [$= K_{sp}^{0.5}$ (common ionic effect should be considered for Cl^- and Na^+ salt cases)]. For the particle growth and redissolution of a free base precipitant, $S_{surface}$ and $S_{dissolv}$ can be set to those of the free base.

REFERENCES

1. Dokoumetzidis, A., Macheras, P. (2006). A century of dissolution research: From Noyes and Whitney to the biopharmaceutics classification system. *Int. J. Pharm*., 321, 1–11.
2. Avdeef, A. (2010). Leakiness and size exclusion of paracellular channels in cultured epithelial cell monolayers-interlaboratory comparison. *Pharm. Res*., 27, 480–489.
3. Sugano, K. (2009). Introduction to computational oral absorption simulation. *Expert Opin. Drug Metabol. Toxicol*., 5, 259–293.
4. Sugano, K., Okazaki, A., Sugimoto, S., Tavornvipas, S., Omura, A., Mano, T. (2007). Solubility and dissolution profile assessment in drug discovery. *Drug Metabol. Pharmacokinet*., 22, 225–254.
5. Galia, E., Nicolaides, E., Horter, D., Lobenberg, R., Reppas, C., Dressman, J.B. (1998). Evaluation of various dissolution media for predicting in vivo performance of class I and II drugs. *Pharm. Res*., 15, 698–705.
6. Nawroth, T., Buch, P., Buch, K., Langguth, P., Schweins, R. (2011). Liposome Formation from bile salt-lipid micelles in the digestion and drug delivery model FaSSIF(mod) estimated by combined time-resolved neutron and dynamic light scattering. *Mol. Pharm*., 8, 2162–2172.

7. Okazaki, A., Mano, T., Sugano, K. (2007). Theoretical dissolution model of poly disperse drug particles in biorelevant media. *J. Pharmaceut. Sci. Tech*., Japan (meeting abstract and poster), 67.
8. Li, C.-Y., Zimmerman, C.L., Wiedmann, T.S. (1996). Diffusivity of bile salt/phospholipid aggregates in mucin. *Pharmceut. Res*., 13, 535–541.
9. Naylor, L.J., Bakatselou, V., Dressman, J.B. (1993). Comparison of the mechanism of dissolution of hydrocortisone in simple and mixed micelle systems. *Pharmaceut. Res*., 10, 865–870.
10. Balakrishnan, A., Rege, B.D., Amidon, G.L., Polli, J.E. (2004). Surfactant-mediated dissolution: contributions of solubility enhancement and relatively low micelle diffusivity. *J. Pharmaceut. Sci*., 93, 2064–2075.
11. Rao, V.M., Lin, M., Larive, C.K., Southard, M.Z. (1997). A mechanistic study of griseofulvin dissolution into surfactant solutions under laminar flow conditions. *J. Pharmaceut. Sci*., 86, 1132–1137.
12. Granero, G.E., Ramachandran, C., Amidon, G.L. (2005). Dissolution and solubility behavior of fenofibrate in sodium lauryl sulfate solutions. *Drug Dev. Ind. Pharmaceut*., 31, 917–922.
13. Sun, W., Larive, C.K., Southard, M.Z. (2003). A mechanistic study of danazol dissolution in ionic surfactant solutions. *J. Pharmaceut. Sci*., 92, 424–435.
14. Okazaki, A., Mano, T., Sugano, K. (2008). Theoretical dissolution model of polydisperse drug particles in biorelevant media. *J. Pharmaceut. Sci*., 97, 1843–1852.
15. Sugano, K. (2010). Aqueous boundary layers related to oral absorption of a drug: from dissolution of a drug to carrier mediated transport and intestinal wall metabolism. *Mol. Pharmaceut*., 7, 1362–1373.
16. Avdeef, A., Tsinman, O. (2008). Miniaturized rotating disk intrinsic dissolution rate measurement: effects of buffer capacity in comparisons to traditional Wood's apparatus. *Pharmaceut. Res*., 25, 2613–2627.
17. Kou, J.H., Fleisher, D., Amidon, G.L. (1991). Calculation of the aqueous diffusion layer resistance for absorption in a tube: application to intestinal membrane permeability determination. *Pharmaceut. Res*., 8, 298–305.
18. Camenen, B. (2007). Simple and general formula for the settling velocity of particles. *J. Hydraul. Eng*., 133, 229–233.
19. Sugano, K. (2008). Theoretical comparison of hydrodynamic diffusion layer models used for dissolution simulation in drug discovery and development. *Int. J. Pharmaceut*., 363, 73–77.
20. Armenante, P.M., Kirwan, D.J. (1989). Mass transfer to microparticles in agitated systems. *Chem. Eng. Sci*., 44, 2781–2796.
21. Crail, D.J., Tunis, A., Dansereau, R. (2004). Is the use of a 200ml vessel suitable for dissolution of low dose drug products? *Int. J. Pharmaceut*., 269, 203–209.
22. Harriott, P. (1962). Mass transfer to particles: Part 1. Suspended inagitated tanks. *AICHE Journal*, 8, 93–102.
23. Galli, C. (2006). Experimental determination of the diffusion boundary layer width of micron and submicron particles. *Int. J. Pharmaceut*., 313, 114–122.
24. Shirhatti, V., Wang, M., Williams, R., Ortega, J.R. (2007). Determination of minimum agitation speed for complete solid suspension using four electrode conductivity method. *AIP Conf. Proc*., 914, 389–396.

25. Sugano, K. (2011). Fraction of a dose absorbed estimation for structurally diverse low solubility compounds. *Int. J. Pharmaceut*., 405, 79–89.
26. Ostergaard, J., Ye, F., Rantanen, J., Yaghmur, A., Larsen, S.W., Larsen, C., Jensen, H. (2011). Monitoring lidocaine single-crystal dissolution by ultraviolet imaging. *J. Pharmaceut. Sci*., 100, 3405–3410.
27. Hintz, R.J., Johnson, K.C. (1989). The effect of particle size distribution on dissolution rate and oral absorption. *Int. J. Pharmaceut*., 51, 9–17.
28. Wang, J., Flanagan, D.R. (2002). General solution for diffusion-controlled dissolution of spherical particles. 2. Evaluation of experimental data. *J. Pharmaceut. Sci*., 91, 534–542.
29. Wang, J., Flanagan, D.R. (1999). General solution for diffusion-controlled dissolution of spherical particles. 1. Theory. *J. Pharmaceut. Sci*., 88, 731–738.
30. Sugano, K. (2010). Computational oral absorption simulation of free base drugs. *Int. J. Pharmaceut*., in press.
31. Mooney, K.G., Mintun, M.A., Himmelstein, K.J., Stella, V.J. (1981). Dissolution kinetics of carboxylic acids. I: Effect of pH under unbuffered conditions. *J. Pharmaceut. Sci*., 70, 13–22.
32. Mooney, K.G., Mintun, M.A., Himmelstein, K.J., Stella, V.J. (1981). Dissolution kinetics of carboxylic acids. II: Effects of buffers. *J. Pharmaceut. Sci*., 70, 22–32.
33. Serajuddin, A.T.M., Jarowski, C.I. (1985). Effect of diffusion layer pH and solubility on the dissolution rate of pharmaceutical bases and their hydrochloride salts. I: Phenazopyridine. *J. Pharmaceut. Sci*., 74, 142–147.
34. Serajuddin, A.T.M., Jarowski, C.I. (1985). Effect of diffusion layer pH and solubility on the dissolution rate of pharmaceutical acids and their sodium salts. II: Salicylic acid, theophylline, and benzoic acid. *J. Pharmaceut. Sci*., 74, 148–154.
35. Sheng, J.J., McNamara, D.P., Amidon, G.L. (2009). Toward an in vivo dissolution methodology: a comparison of phosphate and bicarbonate buffers. *Mol. Pharmaceut*., 6, 29–39.
36. Sugano, K. (2009). A simulation of oral absorption using classical nucleation theory. *Int. J. Pharmaceut*., 378, 142–145.
37. Liu, X.Y. (1999). A new kinetic model for three-dimensional heterogeneous nucleation. *J. Chem. Phys*., 111, 1628–1635.
38. Lindfors, L., Forssen, S., Westergren, J., Olsson, U. (2008). Nucleation and crystal growth in supersaturated solutions of a model drug. *J. Colloid Interface Sci*., 325, 404–413.

CHAPTER 4

THEORETICAL FRAMEWORK III: BIOLOGICAL MEMBRANE PERMEATION

"Observations always involve theory."

—Edwin Hubble

A simple empirical linear correlation between the human intestinal membrane permeability and Caco-2 permeability of drugs (Fig. 7.27) has been used in biopharmaceutical modeling. However, there are many *in vivo* observations that cannot be simulated as far as this simple method is concerned. In the GUT framework, we dismiss this simple empirical correlation approach and introduce a mechanistic theoretical framework.

4.1 OVERALL SCHEME

The overall scheme of the intestinal membrane permeation of a drug is shown in Figure 4.1. After administering a drug, the drug molecules are dissolved in the bulk fluid of the gastrointestinal (GI) tract. The drug molecules exist in the fluid in the unbound or bile-micelle-bound state. The bulk fluid is efficiently mixed in the GI tract, and the dissolved drug molecules are conveyed close to the intestinal membrane surface by the turbulent flow or chaotic mixing. However, the unstirred water layer (UWL) exists adjacent to the intestinal

Biopharmaceutics Modeling and Simulations: Theory, Practice, Methods, and Applications, First Edition. Kiyohiko Sugano.

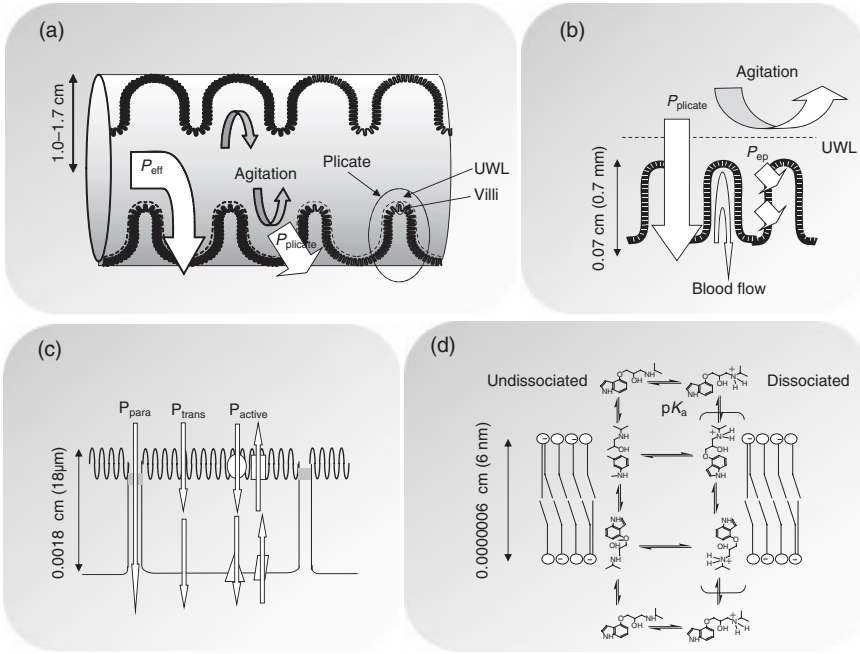

Figure 4.1 Overall scheme of intestinal membrane permeation. (a) Intestinal tube, (b) villi, (c) epithelial cell, and (d) lipid bilayer.

epithelial wall,[1] being a barrier for the transfer of drug molecules from the bulk fluid to the membrane surface. This barrier is relatively thin (ca. 300 μm) but still determines the ceiling of the effective permeability (P_{eff}) of a drug (ca. $2–8 \times 10^{-4}$ cm/s in humans). Both unbound and bile-micelle-bound drug molecules can diffuse through the UWL [1]. The unbound drug molecules then permeate the apical membrane of the epithelial cells mainly by passive diffusion, as well as by carrier-mediated transport in case of some drugs. Efflux transport from the cytosol to the apical side can occur if the drug is a substrate for an efflux transporter. Some drugs pass through the intercellular junction (the paracellular route). In the epithelial cell, a drug metabolism can occur mainly by CYP3A4 and UGTs (intestinal first-pass metabolism). After permeating the basolateral membrane, the drug molecules diffuse through the subepithelial space and then reach the villi blood flow. The villi blood flow then carries the drug molecules to the liver where the drug can be metabolized (liver first-pass metabolism).

[1]The *in vivo* existence of the UWL in the intestine is often argued. However, from the fluid dynamic theory, the existence of UWL is 100% sure. The question is how much diffusion resistance is maintained by the UWL. The current best guess value is 300 μm.

4.2 GENERAL PERMEATION EQUATION

The overall equation to calculate the permeation rate (dX_{perm}/dt), the permeation rate coefficient (k_{perm}), and the effective intestinal membrane permeability (P_{eff}) is expressed as[2] [2]

$$\frac{dX_{perm}}{dt} = k_{perm}X_{dissolv} = \frac{2DF}{R_{GI}}P_{eff}X_{dissolv} \tag{4.1}$$

$$P_{eff} = \frac{PE}{\frac{1}{P'_{ep}} + \frac{1}{P_{UWL}}} = \frac{PE}{\frac{1}{f_u(f_0 \cdot P_{trans,0} + P_{para}) \cdot Acc \cdot VE} + \frac{1}{\frac{D_{eff}}{h_{UWL}} + P_{WC}}} \tag{4.2}$$

where DF is the degree of flatness of the intestinal tube, R_{GI} is the radius of the small intestine, PE and VE are the respective surface area expansion coefficients of the plicate (fold) and villi structures, P_{ep} is the epithelial membrane permeability ($P'_{ep} = f_u \times P_{ep} \times$ Acc $\times$ VE), Acc is the accessibility to the epithelial membrane surface [3], P_{UWL} is the UWL permeability, f_u is the free monomer fraction, f_0 is the fraction of undissociated species, $P_{trans,0}$ is the intrinsic passive transcellular permeability of undissociated species, P_{para} is the paracellular permeability (of unbound species), D_{eff} is the effective diffusion coefficient in the UWL, h_{UWL} is the effective thickness of the UWL, and P_{WC} is the permeability of the UWL by water convection. In the following sections, each component of this equation is discussed.

4.3 PERMEATION RATE CONSTANT, PERMEATION CLEARANCE, AND PERMEABILITY

The relationship between the permeation rate, the permeation rate coefficient, permeation clearance, and permeability is first discussed. Figure 4.2 shows the schematic explanation of the relationship between these parameters.

Passive membrane permeation is a mass transfer process driven by a concentration gradient across a membrane. The permeation rate is the amount of drug permeating the membrane per time (dX_{perm}/dt, dimension: amount/time). Usually, this process follows the first-order kinetics.[3]

$$\frac{dX_{perm}}{dt} = k_{perm} \cdot X_{dissolv} \tag{4.3}$$

[2]Equations to calculate the carrier-mediated transport are discussed later.

[3]Usually, the concentration in the GI tract is much larger than the plasma concentration. Therefore, back flux from the plasma to the GI tract is neglected in this section, unless otherwise noted.

$$\frac{dX}{dt} = k \cdot X \left(= \frac{CL \cdot X}{V} \right) = CL \cdot C = SA \cdot P \cdot C$$

$$= \frac{SA \cdot P \cdot X}{V} = \frac{2}{R} \cdot DF \cdot P \cdot X$$

Figure 4.2 The mathematical conversions between k_{perm}, CL_{perm}, and P_{eff}.

where k_{perm} is the permeation rate coefficient (dimension: time^{-1}).[4] The permeation clearance (CL_{perm}, dimension: volume/time = length^3/time) is defined as

$$k_{perm} = \frac{CL_{perm}}{V_{GI}} \tag{4.4}$$

where V_{GI} is the fluid volume in the GI tract. By inserting Equations 4.3 and 4.4 (cf. $C_{dissolv} = X_{dissolv}/V_{GI}$), the permeation rate is expressed as

$$\frac{dX_{perm}}{dt} = \frac{CL_{perm}}{V_{GI}} \cdot X_{dissolv} = CL_{perm} \cdot C_{dissolv} \tag{4.5}$$

The effective permeability (P_{eff}, dimension: length/time) is defined as the clearance per surface area (based on smooth intestinal surface) (SA_{GI}, dimension: length^2).

$$CL_{perm} = SA_{GI} \cdot P_{eff} \tag{4.6}$$

where SA_{GI} is the intestinal smooth surface area (fold and villi structure is *not* taken into account). By inserting Equations 4.5 and 4.6, the permeation rate is expressed as

$$\frac{dX_{perm}}{dt} = k_{perm} \cdot X_{dissolv} = SA_{GI} \cdot P_{eff} \cdot C_{dissolv}, \qquad k_{perm} = \frac{SA_{GI}}{V_{GI}} P_{eff} \tag{4.7}$$

The permeation flux (J_{perm}) is the amount of drug permeating the membrane per area per time (flux, dimension: amount/length^2/time; cf. concentration = amount/length^3).

$$J_{perm} = P_{eff} C_{dissolv} \tag{4.8}$$

[4]In the case of passive diffusion, the permeation rate coefficient and permeabilities become constant. However, when a carrier-mediated transport is involved, these coefficients become concentration dependent.

These are the general expressions for membrane permeation and can be applied for any other permeation processes.

Example In an *in vitro* permeation assay, 0.1 mg dose of a drug was dissolved in the donor chamber with a volume of 1 ml. After 120 min, 0.001 mg (1%) of the dose was found in the acceptor chamber. The membrane surface area is 0.5 cm^2. In this case, k_{perm}, CL_{perm}, and P_{app} can be calculated as follows.

As only 1% of the drug permeated after 120 min, $X_{dissolv}$ in the donor chamber can be approximated to be constant. By integrating Equation 4.7,

$$X_{perm} = k_{perm} \cdot X_{dissolv} \cdot t$$

Therefore,

$$k_{perm} = \frac{X_{perm}}{X_{dissolv} \cdot t} = \frac{0.001}{0.1 \times 120} = 0.000083 \text{ min}^{-1}$$

$$CL_{perm} = k_{perm} \cdot V = 0.000083 \times 1 = 0.000083 \text{ ml/min}$$

$$P_{app} = \frac{CL_{perm}}{SA} = \frac{0.000083}{0.5} = 0.00017 \text{ cm/min} = 2.7 \times 10^{-6} \text{ cm/s}$$

When the donor volume was changed from 1 to 0.1 ml. The permeated percentage after 120 min can be calculated as follows:

$$k_{perm} = \frac{CL_{perm}}{V_{GI}} = 0.00083 \text{ min}^{-1}$$

$$\frac{X_{perm}}{X_{dissolv}} = k_{perm} \cdot t = 0.00083 \times 120 = 0.1 = 10\%$$

When the fluid volume is smaller, the permeation rate and permeated fraction become larger, whereas the permeability and permeation clearance remain the same. This is the same situation with the relationship between k_{el}, CL, and Vd (k_{el} = CL/Vd) in pharmacokinetics.

4.4 INTESTINAL TUBE FLATNESS AND PERMEATION PARAMETERS

In Equation 4.7, P_{eff} is related to k_{perm} by the surface area/volume ratio (SA_{GI}/V_{GI}). Theoretically, SA_{GI} is a function of V_{GI} and the degree of flatness (DF).

$$SA_{GI} = f(V_{GI}, DF) \tag{4.9}$$

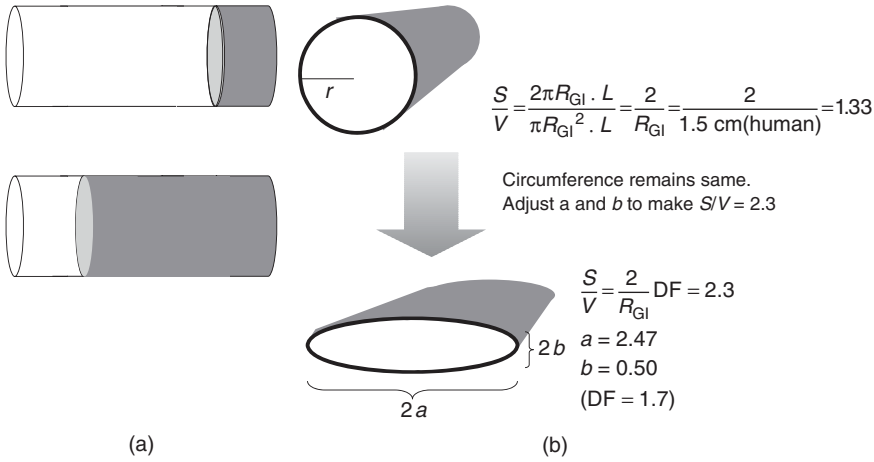

Figure 4.3 Relationship between the fluid volume and available surface area for a tube shape. (a) Fluid volume and surface area and (b) Tube shape and surface area/volume ratio.

DF can be also a function of V_{GI}.[5]

$$\mathrm{DF} = f(V_{\mathrm{GI}}) \tag{4.10}$$

In the case of a tube shape,[6] this ratio can be represented by the radius and degree of flatness of the tube.

$$\frac{\mathrm{SA}_{\mathrm{GI}}}{V_{\mathrm{GI}}} = \frac{2\pi R_{\mathrm{GI}} \cdot L_{\mathrm{GI}}}{\pi R_{\mathrm{GI}}^2 \cdot L_{\mathrm{GI}}}\mathrm{DF} = \frac{2}{R_{\mathrm{GI}}}\mathrm{DF} \tag{4.11}$$

where L_{GI} is the length of the GI tract. Because the small intestine is a tube, the surface area and fluid volume become proportional (Fig. 4.3a). For cylindrical shape, DF = 1. However, the shape of the intestine would be like a deflated fire hose and DF should be larger than 1. As discussed later, DF was estimated to be 1.7 (Fig. 4.3b; Section 8.4.1).

[5]As the membrane shape can be deformed by the fluid volume.

[6]In general, when the two objects are similar in shape, the surface area/volume ratio decreases as the volume increases,

$$\frac{\mathrm{SA}}{V} \propto \frac{L^2}{L^3} = \frac{1}{L}$$

Therefore, the mass (and heat) transfer via the surface becomes inefficient as the volume increases. To compensate this, the surface of the object can be expanded by making folds, protuberances (villi), etc. (Section 6.1).

By summarizing Equations 4.3–4.11, the relationship between P_{eff}, the permeation rate coefficient (k_{perm}), and the absorption rate ($\mathrm{d}X_{\mathrm{perm}}/\mathrm{d}t$) can be expressed as

$$\begin{aligned}\frac{\mathrm{d}X_{\mathrm{perm}}}{\mathrm{d}t} &= k_{\mathrm{perm}} \cdot X_{\mathrm{perm}} = \frac{\mathrm{SA}_{\mathrm{GI}}}{V_{\mathrm{GI}}} \cdot P_{\mathrm{eff}} \cdot X_{\mathrm{perm}} = \mathrm{DF} \cdot \frac{2}{R_{\mathrm{GI}}} \cdot P_{\mathrm{eff}} \cdot X_{\mathrm{perm}} \\ &= k_{\mathrm{perm}} \cdot V_{\mathrm{GI}} \cdot C_{\mathrm{perm}} = \mathrm{SA}_{\mathrm{GI}} \cdot P_{\mathrm{eff}} \cdot C_{\mathrm{perm}} = \mathrm{DF} \cdot \frac{2}{R_{\mathrm{GI}}} \cdot P_{\mathrm{eff}} \cdot V_{\mathrm{GI}} \cdot C_{\mathrm{perm}}\end{aligned} \tag{4.12}$$

The upper and lower parts of Equation 4.12 correspond to the expressions based on the amount and concentration of a drug, respectively.

Example The k_{perm} and Fa of atenolol in humans can be calculated from the human P_{eff} as follows ($P_{\mathrm{eff}} = 0.2 \times 10^{-4}$ cm/s) [4] (cf. $R_{\mathrm{GI}} = 1.5$ cm, $T_{\mathrm{si}} = 210$ min, $\mathrm{Fa} = 1 - \exp(-k_{\mathrm{perm}} T_{\mathrm{si}})$):

$$k_{\mathrm{perm}} = \mathrm{DF}\frac{2}{R_{\mathrm{GI}}}P_{\mathrm{eff}} = 1.7 \times \frac{2}{1.5} \times 0.00002 = 0.000045\ \mathrm{s}^{-1} = 0.0027\mathrm{min}^{-1}$$

$$\mathrm{Fa} = 1 - \exp\left(-k_{\mathrm{perm}} T_{\mathrm{si}}\right) = 1 - \exp\left(-0.0027 \times 210\right) = 0.43$$

4.5 EFFECTIVE CONCENTRATION FOR INTESTINAL MEMBRANE PERMEABILITY

4.5.1 Effective Concentration for Unstirred Water Layer Permeation

In the GUT framework, the effective intestinal membrane permeability (P_{eff}) is defined based on the sum of the concentrations of molecular states being able to permeate the first permeation barrier, the UWL. Free monomers and bile-micelle-bound molecules are considered to diffuse through the UWL [1]. Therefore, P_{eff} is defined based on C_{dissolv}. This is the unified definition of effective concentration for both permeation and dissolution.

$$X_{\mathrm{dissolv}} = X_{\mathrm{mono}} + X_{\mathrm{bm}} = f_{\mathrm{mono}} X_{\mathrm{dissolv}} + (1 - f_{\mathrm{mono}}) X_{\mathrm{dissolv}} \tag{4.13}$$

$$C_{\mathrm{dissolv}} = \frac{X_{\mathrm{dissolv}}}{V_{\mathrm{GI}}} \tag{4.14}$$

4.5.2 Effective Concentration for Epithelial Membrane Permeation: the Free Fraction Theory

In most cases, it would be appropriate to assume that only free monomers can permeate the epithetical membrane. There are many experimental data showing that bile-micelle binding reduces apparent permeability (P_{app}) *in vitro*, *in situ*,

and *in vivo* (P_{app} is usually calculated based on $C_{dissolv}$) [5–11].[7] Bile-micelle binding is thought to be one of the main reasons for the negative food effect (Section 12).

The effective epithelial membrane permeability (P'_{ep}), which is defined based on the total dissolved drug concentration, is expressed as

$$P'_{ep} = f_u \cdot P_{ep} \tag{4.15}$$

If the UWL permeability is negligible, P_{eff} is expressed as

$$P_{eff} = f_u \cdot P_{ep} \cdot PE \cdot VE \tag{4.16}$$

This is similar to the hepatic clearance calculation, in which the intrinsic hepatic clearance ($CL_{h,int}$) and unbound fraction in the plasma (f_{up}) are related to the hepatic clearance (CL_h) as $CL_h = f_{up}CL_{h,int}$ (when $Q_h > f_{up}CL_{h,int}$; Section 4.11).

4.6 SURFACE AREA EXPANSION BY PLICATE AND VILLI

P_{eff} value is usually calculated assuming that the small intestine is a smooth tube. However, the small intestinal has a plicate and villi structure. The UWL is adjacent to the top of the villi. Therefore, P_{eff} can be expressed as

$$P_{eff} = P_{plicate} \cdot PE \tag{4.17}$$

where $P_{plicate}$ is the plicate surface permeability and PE represents the surface area expansion by the plicate structure. The plicate surface permeation is a sequence of UWL and epithelial membrane permeations.

$$P_{plicate} = \frac{1}{\dfrac{1}{P_{UWL}} + \dfrac{1}{f_u \cdot P_{ep} \cdot Acc \cdot VE}} \tag{4.18}$$

where P_{UWL} is the UWL permeability, Acc is the accessibility to the villi surface, and VE is the villi expansion. Acc depends on the diffusion coefficient and the epithelial membrane permeability of a drug. In the case of a drug with high permeability, drug molecules are absorbed from the top of the villi before they diffuse to the crypt of the villi (Fig. 4.4), whereas in the case of a drug with low

[7]Usually an *in vitro* permeability assay (e.g., Caco-2) is performed without adding bile micelles to the donor chamber. Therefore, before using an *in vitro* data for biopharmaceutical modeling, the permeability should be corrected for bile micelle binding by multiplying with f_u.

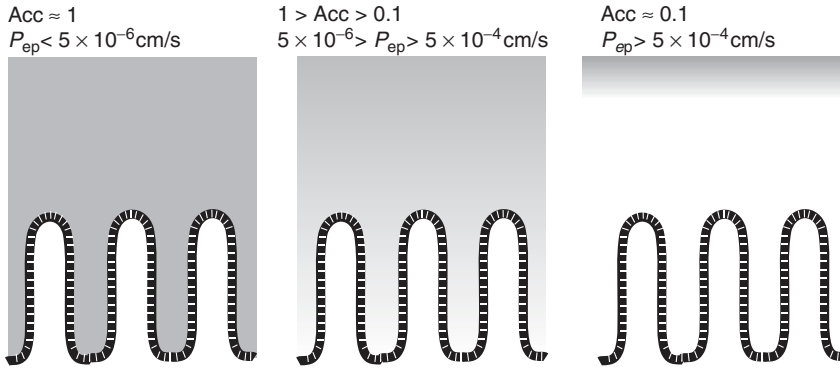

Figure 4.4 Villi available surface area for different P_{ep} drugs.

permeability, the entire surface is utilized for membrane permeation. Acc can be calculated as follows [3]:

$$q = \frac{1}{2}\left[(\beta^2+4)^2+\beta\right], \quad r = \frac{1}{2}\left[(\beta^2+4)^2-\beta\right] \tag{4.19}$$

$$\gamma = \left(\frac{f_u P_{ep} H_{villi}^2}{D_{eff} W_{channel}}\right)^{1/2}, \quad \beta = \left(\frac{P_{WC}^2 W_{channel}}{f_u P_{ep} D_{eff}}\right)^{1/2} \tag{4.20}$$

$$AA = \frac{\frac{1}{\gamma}\left\{\left(\frac{r}{q}\right)\exp(-r\gamma)[1-\exp(-q\gamma)] - \left(\frac{q}{r}\right)\left[\exp(-r\gamma)-1\right]\right\}}{q + r\exp\left[-\gamma(r+q)\right]} \tag{4.21}$$

$$BB = \frac{\left[\frac{W_{channel}}{H_{villi}}(r+q)\exp(-r\gamma)\right]}{q + r\exp[-\gamma(r+q)]} \tag{4.22}$$

$$Acc = \frac{\left(AA + BB + \frac{W_{villi}}{H_{villi}}\right)}{\left(1 + \frac{W_{channel}}{H_{villi}} + \frac{W_{villi}}{H_{villi}}\right)} \tag{4.23}$$

where P_{WC} is permeation by water conveyance, W_{villi} is the width of villi, $W_{channel}$ is the width of the channel between villi, and H_{viili} is the height of villi. Figure 4.5 shows the effect of Acc on P_{eff} calculation. In the case of low P_{ep} drugs (ca. $P_{ep} < 5 \times 10^{-6}$ cm/s at pH 6.5), P_{eff} is predominantly determined by epithelial membrane permeation and Acc has little effect. For high P_{ep} drugs (ca. $P_{ep} > 500 \times 10^{-6}$ cm/s at pH 6.5), P_{eff} is predominantly determined by the UWL and Acc has little effect. Acc has the largest effect (1.7-fold) when the UWL permeability and epithelial membrane permeability are in the same order of magnitude (ca. $P_{ep} = 5 - 500 \times 10^{-5}$ cm/s at pH 6.5, $0 < \log D_{oct} < 2$ at

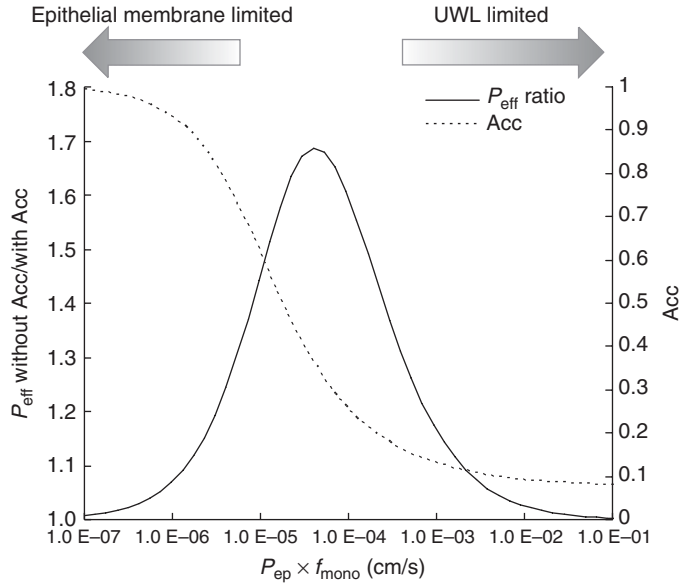

Figure 4.5 Effect of Acc on P_{eff} estimation.

pH 6.5). The maximum error by ignoring the Acc (i.e., assuming Acc = 1) is ca. 1.7-fold in P_{eff} prediction (Fig. 4.5). However, in this range, the oral absorption of a drug usually becomes rapid and complete (unless otherwise Do >1[8]). Therefore, in cases where Fa% <90%, the Acc has little effect on Fa% prediction accuracy (hence, Acc = 1 assumption is appropriate for Fa% prediction).

4.7 UNSTIRRED WATER LAYER PERMEABILITY

4.7.1 Basic Case

Both free monomers and bile-micelle-bound molecules can pass through the UWL, which partly superimposes to the mucous layer. In addition to diffusion, water conveyance would also affect UWL permeation [12, 12]. P_{UWL} can be expressed as

$$P_{UWL} = \frac{D_{eff}}{h_{UWL}} + P_{WC} = \frac{f_{mono}D_{mono} + (1 - f_{mono})D'_{bm}}{h_{UWL}} + P_{WC} \qquad (4.24)$$

D'_{bm} is the diffusion coefficient of bile-micelle-bound drug in the UWL. When the bile acid concentration is <3 mM, the effective diffusion coefficient in the mucous layer was reported to be three times higher compared to that in water [14].

[8]However, this case is rare (only for a compound with very high melting point (Section 2.3.7)).

Even though both unbound and bile-micelle-bound drugs can permeate the UWL, the unbound monomer fraction (f_u) affects P_{UWL}, as D_{bm} is 8–80 times smaller than D_{mono}. P_{UWL} becomes smaller when the unbound fraction is smaller. This should not be confused with the effect of f_u on the effective epithelial membrane permeability (P'_{ep}). Bile-micelle binding reduces both P_{UWL} and P'_{ep}. In the case of the UWL permeability, P_{UWL} does not become zero even when f_u is zero, whereas in the case of the epithelial membrane permeation, P'_{ep} becomes zero when f_u is zero. However, even for very highly lipophilic drugs, P'_{ep} does not become zero because the slope of log P_{oct}–K_{bm} relationship (0.74) is smaller than that of log P_{oct}–$P_{trans,0}$ relationship (ca. 1).

4.7.2 Particles in the UWL (Particle Drifting Effect)

There had been a large discrepancy between the theoretical Fa% prediction and experimental observations for solubility-unstirred water permeability limited cases (SL-U) (Chapter 10). As discussed in Chapter 1, the theory suggested that the absorbed amount of a drug would not be increased when the dose was increased or particle size was reduced for the SL cases. These theoretical suggestions are in good agreement with experimental observations for solubility-epithelial membrane permeability limited cases (SL-E) and SL-U cases with moderate particle size and dose (>5 μm and <5 mg/kg), but not for the SL-U cases with small particle size and/or large dose (<5 μm and/or >5 mg/kg) (Chapters 8 and 10; Fig. 10.2).

The particle drifting effect (PDE) was recently proposed [15] as a possible explanation for this discrepancy. The absorbed amount of a drug in solubility-permeability limited cases is determined by the solubility and permeability of the drug (but not the dissolution rate). However, the solubility of a drug is independent of the dose and particle size.[9] Therefore, even though it might be counter-intuitive, the permeability of a drug should have changed depending on the dose and particle size.

Many reports showed that a significant portion of microscale particles can drift into the UWL [16–20]. The structure of the mucous layer (i.e., micrometer-scale mesh size; Chapter 6; Fig. 6.7) also supports this experimental observation.

When the drug particles exist within the UWL, the distance from the particle to the epithelial cell surface becomes shorter. This reduction in diffusion length should be taken into account in biopharmaceutical modeling. This effect would be proportional to the drug particle surface area (i.e., dose and the inverse of particle size) in the UWL and would be significant when the surface area of the drug particles is in the same order of magnitude as the intestinal membrane surface (Section 3.2.3). These drug particles in the UWL could be the reservoir of a drug in the UWL.

In conscious humans, the total thickness of the UWL (h_{totUWL}) is reported to be ca. 0.03 cm (a plicate-surface-based value; it is 0.01 cm when based

[9]Unless otherwise the particle size is $\ll$100 nm (Sections 2.3.9 and 7.6.3.4).

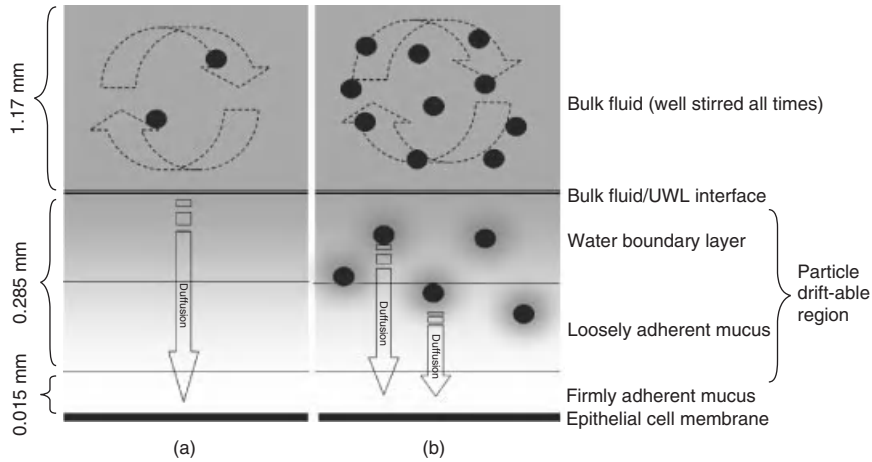

Figure 4.6 Particle drifting effect. (a) Low dose: drug molecules are supplied only from the bulk fluid/UWL interface. (b) High dose: drug molecules are supplied from both the particle surface in the UWL and the bulk fluid/UWL interface. *Source:* Adapted from Reference 15 with permission.

on a smooth surface) (Section 6.2.3.3). The UWL consists of the mucous and aqueous boundary layers (the latter is called the *Prandtl's boundary layer*, which is maintained solely by the viscosity of water; Fig. 4.6). The mucous layer is divided into two regions: the firmly adhered and loosely bound regions [21, 22]. The loosely bound mucous region can be renewed by a fluid flow.

Since the self-diffusion of micrometer-scale particles is negligibly small, the drug particles may be drifted into the UWL by the fluctuating fluid flow and/or the sedimentation by gravity (nanoscale particles may self-diffuse by Brownian motion). Fluctuation of intestinal fluid flow by the peristaltic moves of the intestinal wall is a well-known phenomenon. The loosely adhered mucus is easily removed by a flow [21, 22]. Therefore, the UWL would not be a completely static water layer. The fluid in the UWL can be renewed by an occasional strong flow and drug particles can be carried into the UWL (such as snow drifting on the hedge or sand drifting on the seacoast). However, the average flow in the UWL is weak, and the UWL becomes a barrier against self-diffusion majority of the time.

As the drug particles drift into the UWL, the effective thickness of the UWL looks reduced (Fig. 4.6). Considering the PDE, h_{UWL} is calculated as

$$h_{\mathrm{UWL}} = h_{\mathrm{fam}}\left[1 - \mathrm{RK}\left(\frac{r_{\mathrm{p,mean}}}{R_{\mathrm{mucous}}}\right)\right] + h_{\mathrm{pd}} - \frac{1}{2}h_{\mathrm{pd}} \cdot R_{\mathrm{SA}} \quad R_{\mathrm{SA}} \leq 1 \tag{4.25}$$

$$h_{\mathrm{UWL}} = h_{\mathrm{fam}}\left[1 - \mathrm{RK}\left(\frac{r_{\mathrm{p,mean}}}{R_{\mathrm{mucous}}}\right)\right] + \frac{1}{2} \cdot \frac{h_{\mathrm{pd}}}{R_{\mathrm{SA}}} \qquad R_{\mathrm{SA}} > 1 \tag{4.26}$$

$$R_{SA} = \frac{3 \cdot C_{pd} \cdot h_{pd} \cdot \text{Dose}}{V_{GI} \cdot \rho} \sum_i \frac{f_i}{r_{p,i}} \tag{4.27}$$

where h_{fam} is the thickness of the firmly adhered mucous layer, R_{mucous} is the nominal radius of the pore size of the mucous layer, R_{SA} is the ratio of the drug particle surface area in the UWL and the villi surface area, C_{pd} is the particle drifting coefficient, and h_{pd} is the thickness of the particle driftable region defined as $h_{pd} = h_{tot,UWL} - h_{fam}$. RK is a size sieving function (the Renkin function, Eq. 4.37). The $1 - \text{RK}$ term was introduced to represent the particles penetrating into the firmly adhered mucous layer. R_{mucous} and C_{pd} were reported to be 2.9 μm and 2.2, respectively [23].

The concept of PDE is recently introduced and requires further validation (for validation of PDE, see Chapters 8 and 10). The PDE should be also considered for nasal and pulmonary absorptions, as the fluid on the membrane is very thin and is not stirred, and drug particles are directly delivered into this thin UWL in these administration sites.

4.8 EPITHELIAL MEMBRANE PERMEABILITY (PASSIVE PROCESSES)

The epithelial membrane permeability (P_{ep}) can be further deduced to passive transcellular (P_{trans}) and paracellular (P_{para}) permeabilities (carrier-mediated transport is discussed later).

$$P_{ep} = P_{trans} + P_{para} \tag{4.28}$$

4.8.1 Passive Transcellular Membrane Permeability: pH Partition Theory

The cellular membrane is a lipid bilayer mainly consisting of phospholipids and cholesterol (Fig. 6.4). The lipophilic core of a lipid bilayer becomes the permeation barrier for hydrophilic molecules. In the case of dissociable drugs, P_{trans} can be represented as the weighted sum of the permeability of each species.

$$P_{trans} = f_0 \cdot P_{trans,0} + f_+ \cdot P_{trans,+} + f_- \cdot P_{trans,-} + f_{++} \cdot P_{trans,++} + \cdots \tag{4.29}$$

$$f_0 + f_+ + f_- + f_{++} + \cdots = 1 \tag{4.30}$$

where $P_{trans,0}$ is the intrinsic permeability of the undissociated species, $P_{trans,+}$ is that of $+1$ charged species, etc. The fraction of each species (f) depends on the pH near the epithelial membrane surface (microclimate pH, 5.5–6.5) and the pK_a(s) of a drug (Section 6.1). Usually, the uncharged species is much more permeable

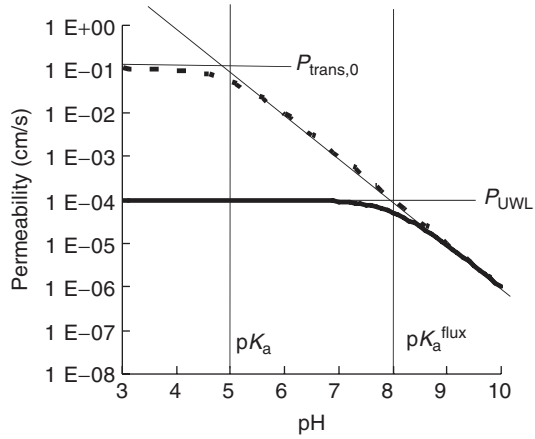

Figure 4.7 pH–permeability curve for an acidic drug.

than the charged species. Therefore, according to the pH partition theory,[10,11]

$$P_{trans} \approx f_0 \cdot P_{trans,0} \tag{4.31}$$

A typical pH–permeability curve is shown in Figure 4.7. The slope of the logarithmic plot is 1. In this slope region, one unit difference of pH or pK_a (a logarithmic scale) corresponds to a 10-fold change in permeability on a normal scale. Therefore, when a nonphysiological pH is used in an *in vitro* membrane assay for a dissociable drug, the effect of pH should be corrected before using the permeability value for biopharmaceutical modeling.[12] When the effect of the UWL is negligible, the horizontal line corresponds to $P_{trans,0}$. The crossover point of the slope line and the horizontal line is the pK_a the drug. However, when the UWL limits the permeability, the horizontal line becomes lower than $P_{trans,0}$, and the crossover point (pK_a flux) is not the same as the pK_a of the drug [26].

4.8.2 Intrinsic Passive Transcellular Permeability

4.8.2.1 Solubility–Diffusion Model. $P_{trans,0}$ can be further deduced from the interactions between a drug and the lipid bilayer. The simplest way to calculate the membrane permeability from the molecular properties of a drug and the membrane constituents is to treat the lipid bilayer as a homogeneous organic solvent membrane and apply Fick's law (Fig. 4.8) [27]. The passive permeation

[10]This relationship is similar to that of octanol–water partition coefficient (P_{oct}) and octanol–water distribution coefficient (D_{oct}), as $D_{oct} = f_0 P_{oct}$ (Section 7.2).

[11]Recently, it was suggested that ionized molecular species can also passively permeate the lipid bilayer (however, much slower than the neutral species) [24, 24].

[12]A pH of 7.4 is often used in an *in vitro* assay, although it is ca. 1 pH unit higher than the microclimate pH.

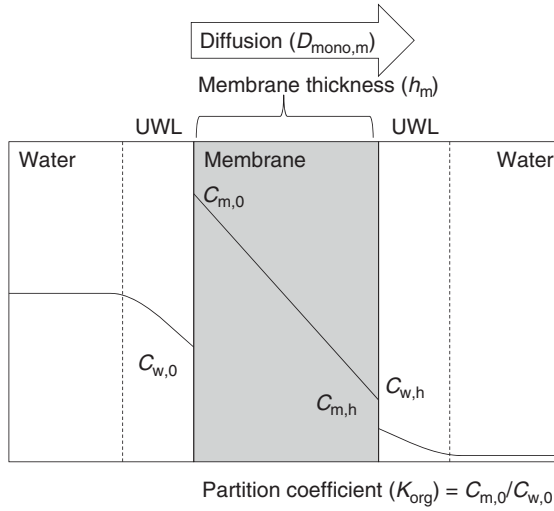

Figure 4.8 Homogeneous membrane model.

across a membrane is a diffusion process, the driving force of which is the concentration gradient across the membrane (i.e., Fick's law). If the interfacial resistance at the lipid–water interface is assumed negligible, flux (J) can be expressed as

$$J = \frac{D_m(C_{m,0} - C_{m,h})}{h_m} = \frac{D_m K_{org}(C_{W,0} - C_{W,h})}{h_m} = P_0(C_{W,0} - C_{W,h}) \quad (4.32)$$

where $D_{mono,m}$ is the diffusion coefficient of a drug in the membrane, h_m is the thickness of the membrane, and $C_{m,0}$ and $C_{m,h}$ are the concentrations of a drug at positions 0 and h in the membrane, respectively. $C_{m,0}$ and $C_{m,h}$ can be expressed by the partition coefficient between the water and the organic solvent (K_{org}) and the concentration in the water phases of the donor and acceptor sides ($C_{W,0}$ and $C_{W,h}$, respectively). Considering the sink condition, $C_{W,h}$ is approximated to be zero. Equation 4.32 indicates that the permeability is determined by the partition (a static parameter) and diffusion coefficients (a kinetic parameter) and the thickness of the membrane.[13]

The solubility–diffusion model can be extrapolated to the inhomogeneous membrane model [28]. The permeability coefficient is the reciprocal of the permeation resistance, and the total permeation resistance connected in series is the sum of each resistance (same as Ohm's law).

$$\frac{1}{P_{trans,0}} = \int_0^h \frac{1}{D_m(x)K_{org}(x)}dx \quad (4.33)$$

[13]This is similar to the Nernst–Brunner equation, in which the intrinsic dissolution rate is defined by the diffusion coefficient, thickness of the UWL on the particle, and solubility at the solid surface.

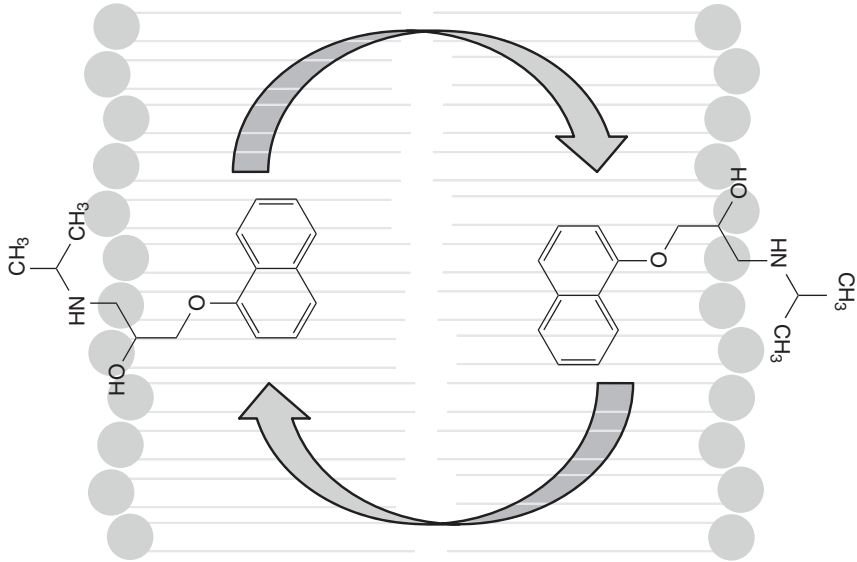

Figure 4.9 Flip-flop membrane permeation.

where $D_m(x)$ is the local diffusion coefficient at position x and $K_{org}(x)$ is the local partition coefficient between water and position x. According to Equation 4.33, the lowest permeability region (barrier domain) limits the total permeability. Therefore, Equation 4.33 can be simplified to Equation 4.32. K_{org} is the partition coefficient of a solute from water (not from the polar head group interface) to the barrier domain. The diffusion coefficient in the membrane is suggested to be lower than that in a nonpolar solvent such as hexadecane. The ordered region of the hydrophobic core (high density tail region in Figure 6.4) is suggested to behave like a soft polymer, leading to a reduction in the diffusion coefficient of this region.

According to the solubility–diffusion model, the membrane permeability coefficient can be related to the partition coefficient between water and the barrier region. If a suitable organic solvent that resembles the rate-limiting barrier is chosen, the membrane permeability coefficient can be calculated from the partition coefficient between water and the organic solvent, the diffusion coefficient, and the thickness of the barrier. In the case of a lipid bilayer mainly composed of phospholipids, simple alkanes or alkenes were suggested to reflect the rate-limiting permeation barrier for hydrophilic molecules [28–31]. Octanol was suggested to be less suitable, although it is the most often used organic solvent for QSAR (quantitative structure–activity relationship). However, the solubility diffusion theory has been investigated mainly for small molecules (MW$<$100), and its applicability to druglike molecules is not known.

4.8.2.2 Flip-Flop Model. The flip-flop mechanism has also been investigated as the membrane permeation mechanism [32–34]. Figure 4.9 shows the concept

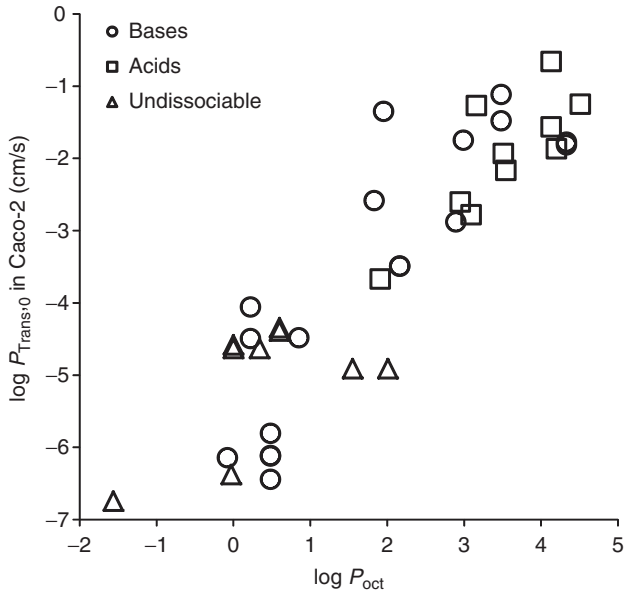

Figure 4.10 Relationship between log P_{oct} and log $P_{trans,0}$ in Caco-2 for nontransporter substrates.

of the flip-flop mechanism. The flip-flop model has been proposed to describe the transmembrane movement of large amphiphilic molecules or peptide mimetic molecules (e.g., doxorubicin). The transmembrane movement can be described as (i) incorporation of a compound into one membrane leaflet and (ii) transfer (flip-flop) across the lipid core. In the case of fatty acids, it was found that the first step was much faster than the second flip-flop step, and the flip-flop rate decreased as the chain length increased [35, 36].

4.8.2.3 Relationship between $P_{trans,0}$ and log P_{oct}. The octanol–water partition coefficient is most often used as the surrogate of K_{org}. $P_{trans,0}$ and P_{oct} show broad but linear relationship over the range of $-2 < \log P_{oct} < 4$ and $0.0000001 < P_{trans,0} < 0.1$ cm/s.[14][15] Previously, the following equation was proposed to roughly estimate $P_{trans,0}$ in the Caco-2 assay [2, 2].

$$\log P_{trans,0}(\text{cm/s}) = 1.1 \log P_{oct} - 5.6 \tag{4.34}$$

This equation is derived using experimental P_{oct} values. $P_{trans,0}$ is calculated from Caco-2 apparent permeability data (cf. Section 7.9.5) [37–39]. Figures 4.10

[14]Note that the order is not 10^{-6}. The high end value of 0.1 cm/s ($100{,}000 \times 10^{-6}$ cm/s) might look odd, as the highest apparent permeability (P_{app}) experimentally observed is usually 50×10^{-6} cm/s. However, this upper limit in P_{app} is due to the thick UWL in a standard *in vitro* setting. Once the UWL effect is corrected, $P_{trans,0}$ can reach up to 0.1 cm/s.

[15]This does not mean that octanol and lipid bilayer have exactly the same selectivity for drug permeation. The standard deviation of this relationship is ca. 1 log unit.

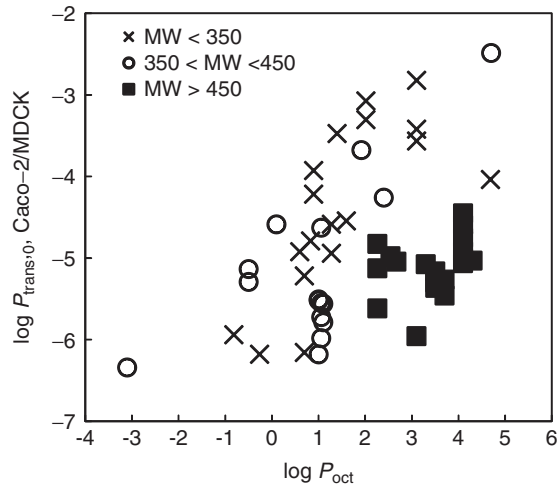

Figure 4.11 Relationship between log P_{oct} and log $P_{trans,0}$ for P-gp substrates in Caco-2 and MDCK cells under P-gp inhibition.

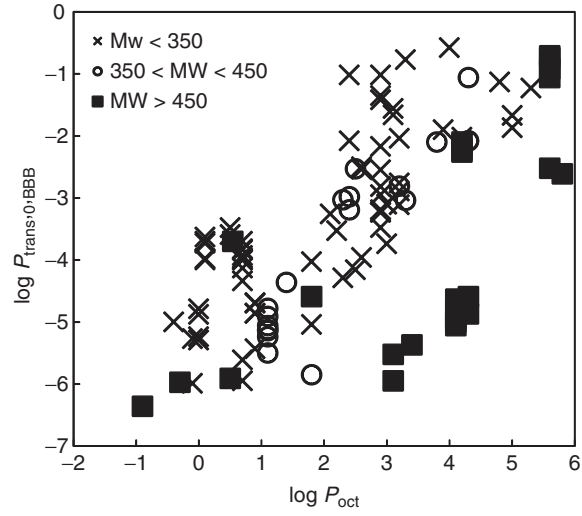

Figure 4.12 Relationship between log P_{oct} and the intrinsic blood–brain barrier permeability ($P_{trans,0,BBB}$) measured by brain perfusion experiments in P-gp knockout mice (or non-P-gp substrates). *Source:* Plotted based on References 40 and 41.

and 4.11 show the relationship between log P_{oct} and log $P_{trans,0}$. Figure 4.11 was based on the analysis of passive permeability for the P-gp substrates, which tended to have higher MW (Section 4.9.5). Figure 4.12 shows the similar relationship between passive blood–brain barrier (BBB) permeability and log P_{oct} [40, 41]. It is interesting that regardless of the cell types (i.e., Caco-2, MDCK, and mice BBB), the relationships between log P_{oct} and log $P_{trans,0}$ were similar. A large molecule (MW > 500) with medium to high lipophilicity (log $D_{oct,\ pH6.5} > 1.5$) tended to deviate downward from the central correlation line. Previously, similar deviation was observed in the Caco-2 study [42], but the P-gp effect was not excluded. However, even after removing the P-gp effect, this deviation was observed. This finding suggested that the passive permeation mechanism could be different for small and large molecules. For small molecules, the transmembrane permeation may be simply described by the partition-diffusion mechanism, whereas the flip-flop mechanism would be more suitable for large molecules. Equation 4.34 can be used for the drugs with MW<500 and log $D_{oct,\ pH6.5} = 2–5$, but not for drugs with MW > 500 and log $D_{oct,pH\ 6.5} > 5$. When the MW effect was taken into account, the following empirical equation was obtained (Fig. 4.13).

$$\log P_{trans,0}(\text{cm/s}) = 0.89 \log P_{oct} - \frac{MW^{0.6}}{8.2} - 1.2 \tag{4.35}$$

Even though Equations 4.34 and 4.35 only provide a rough estimation of $P_{trans,0}$, these equations are practically useful in drug discovery and development,

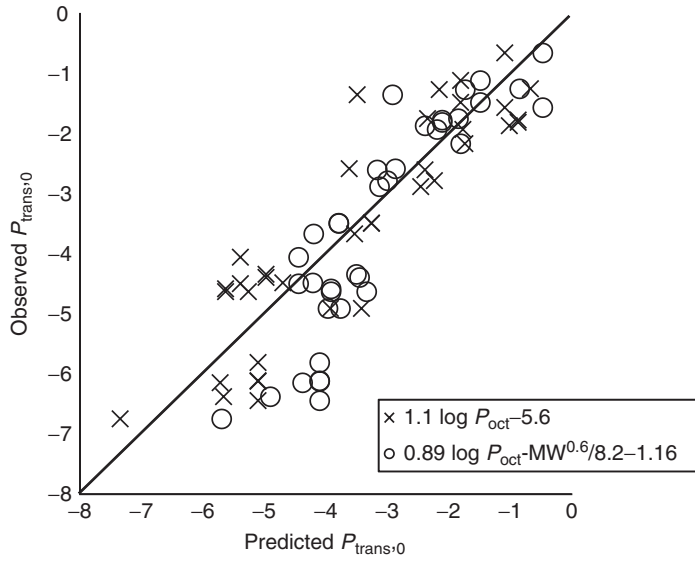

Figure 4.13 Estimated and observed $P_{trans,0}$ for nontransporter substrates.

especially for lipophilic drugs (log $D_{\text{oct,pH 6.5}} > 2$). Owing to the artifacts in an *in vitro* assay (Section 7.9.8), there is an inherent risk of underestimation of P_{app} for drugs with high lipophilicity (log $D_{\text{oct,pH6.5}} > 1.5$). On the other hand, experimental log $D_{\text{oct,pH 6.5}}$ is relatively reliable up to 4. In addition, at log $D_{\text{oct,pH 6.5}} > 2$, P_{eff} is governed by the UWL in most cases (except where MW > 500), and therefore, accurate estimation of P_{ep} is not required. Equations 4.34 and 4.35 should not be used if $P_{\text{trans,0}} > 0.1$ cm/s, as these equations were not validated in this range. There should be a theoretical upper limit for $P_{\text{trans,0}}$ controlled by diffusion process in the cytosol.

Example The P_{trans} of ketoprofen at pH 6.5 can be estimated from its log P_{oct} (3.2) and pK_a (4.0) as follows.[16]

$$\log P_{\text{trans,0}}(\text{cm/s}) = 1.1 \times 3.2 - 5.6 = -2.1$$

$$f_0 = \frac{1}{1 + \dfrac{10^{-4.0}}{10^{-6.5}}} = 0.0030$$

$$P_{\text{trans}} = 0.0030 \times 10^{-2.1} = 24 \times 10^{-6}\text{cm/s}$$

4.8.3 Paracellular Pathway

Small molecules can permeate the tight junction between the epithelial cells. The tight junction is maintained by the cell adhesion molecules and is negatively charged. Cationic small molecules (MW < 200 –400 for humans) tend to be able to permeate the paracellular pathway, whereas large and/or negatively charged molecules cannot. Drug permeation through the paracellular pathway has been successfully modeled using a negative-charge tube model [43–50].

$$\begin{aligned} P_{\text{para}} &= f_0 \cdot P_{\text{para,0}} + f_+ \cdot P_{\text{para,+}} + f_- \cdot P_{\text{para,-}} + f_{++} \cdot P_{\text{para,++}} + \cdots \\ &= A'' \cdot \frac{1}{\text{MW}^{1/3}} \cdot \text{RK}\left(\frac{\text{MW}^{1/3}}{R_{\text{MW}}}\right)\left(f_0 + \sum^{z(z\neq 0)} f_z \cdot E(z)\right) \end{aligned} \tag{4.36}$$

$$\text{RK}(R_{\text{ratio}}) = (1 - R_{\text{ratio}})^2[1 - 2.104 \cdot R_{\text{ratio}} + 2.09(R_{\text{ratio}})^3 - 0.95(R_{\text{ratio}})^5] \tag{4.37}$$

$$E(z) = \frac{Z_{\text{para}} \cdot z}{1 - \exp(-Z_{\text{para}} \cdot z)} \tag{4.38}$$

[16]The following misunderstanding is frequently cited in the literature of transporters: "A dissociable drug with a pK_a of 8.5 (base) or pK_a 4.5 (acid) is 99% ionized at a neutral pH and cannot permeate the lipid bilayer membrane by passive diffusion." (often followed by "Therefore, the majority of the ionizable drugs are absorbed via a transporter."). This misunderstanding might come from overlooking the point that $P_{\text{trans,0}}$ can be at least as high as $100{,}000 \times 10^{-6}$ cm/s.

where f_z is the fraction of each charged species (z, charge number) calculated from pK_a(s) of a drug, R_{ratio} is the ratio of the apparent pore radius of the paracellular pathway based on MW selectivity (R_{MW} (8.46 for humans)) and the molecular radius of a permeant (r_{mono}) ($R_{ratio} = MW^{1/3}/R_{MW}$), and A'' is a lump constant of the paracellular pathway population, etc. ($A'' = 3.9 \times 10^{-4}, P_{para}$ in cm/s). Z_{para} corresponds to the apparent electric potential of the paracellular pathway (for the intestine, -18 to -80 mV). Owing to this negative charge, the paracellular pathway is cation selective [44, 51]. RK is a molecular sieving function (Renkin function) [52]. RK decreases as the molecular radius of a permeant increases. Even though the paracellular pathway model equation was a first approximation, it appropriately modeled the contribution of the paracellular pathway (Section 8.4.4). In addition to MW and z, the substrate's lipophilicity was also suggested to affect the paracellular pathway permeability [53, 54]. The molecular shape of a drug was suggested to affect P_{app} for specific cases such as PEGs [55].

The effective width of the paracellular pathway is different between animals and humans. The paracellular pathway is significantly leakier in dogs than in rats and humans [56] (Section 13.5.1). Caco-2 cells tend to have tighter tight junctions than the human small intestine [57]. Therefore, the paracellular pathway should be taken into account when we investigate species differences and *in vitro–in vivo* correlation.

Figure 4.14 shows the prediction of Fa% via P_{para} calculated using Equations 4.36–4.39. The paracellular pathway is often mentioned as a minor pathway when compared to passive transcellular permeation. However, many hydrophilic basic drugs (p$K_a >$ ca. 6.5) are suggested to permeate the paracellular pathway; for example, atenolol (MW = 266), metformin (MW = 129), and ranitidine (MW = 314). As P_{para} can be estimated from MW and pK_a with reasonable accuracy, the benefit/cost ratio of P_{para} calculation is appropriate.

4.8.4 Relationship between log D_{oct}, MW, and Fa%

Figure 4.15 shows the relationship between log D_{oct} (pH 6.5), MW, and Fa% calculated using Equations 4.35–4.38. The theoretical calculation is in good agreement with the experimental observation shown in Figure 8.8.

4.9 ENTERIC CELL MODEL

Figure 4.16 is the schematic presentation of an epithelial cell. To appropriately simulate the biological processes in the cytosol, the effective concentration of a drug in the cytosol should be defined as the unbound drug concentration ($f_{u1}C_1$).[17] $f_{u1}C_1$ could be significantly different from the drug concentration in the apical side. Full numerical integration of the processes in Figure 4.16 has been extensively used to investigate the pharmacokinetics in the enteric cells [58–65].

[17]The definitions of parameters shown in Figure 4.16 are used in this section.

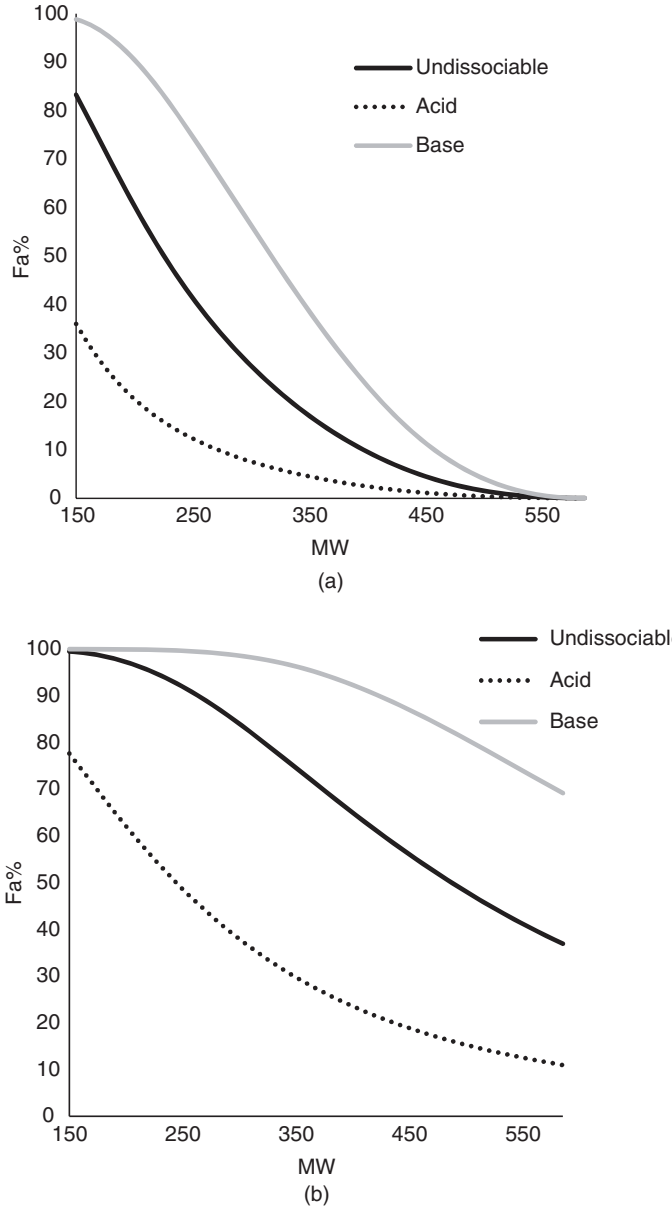

Figure 4.14 Fa% via paracellular pathway estimated based on the GUT framework. (a) Humans and (b) dogs.

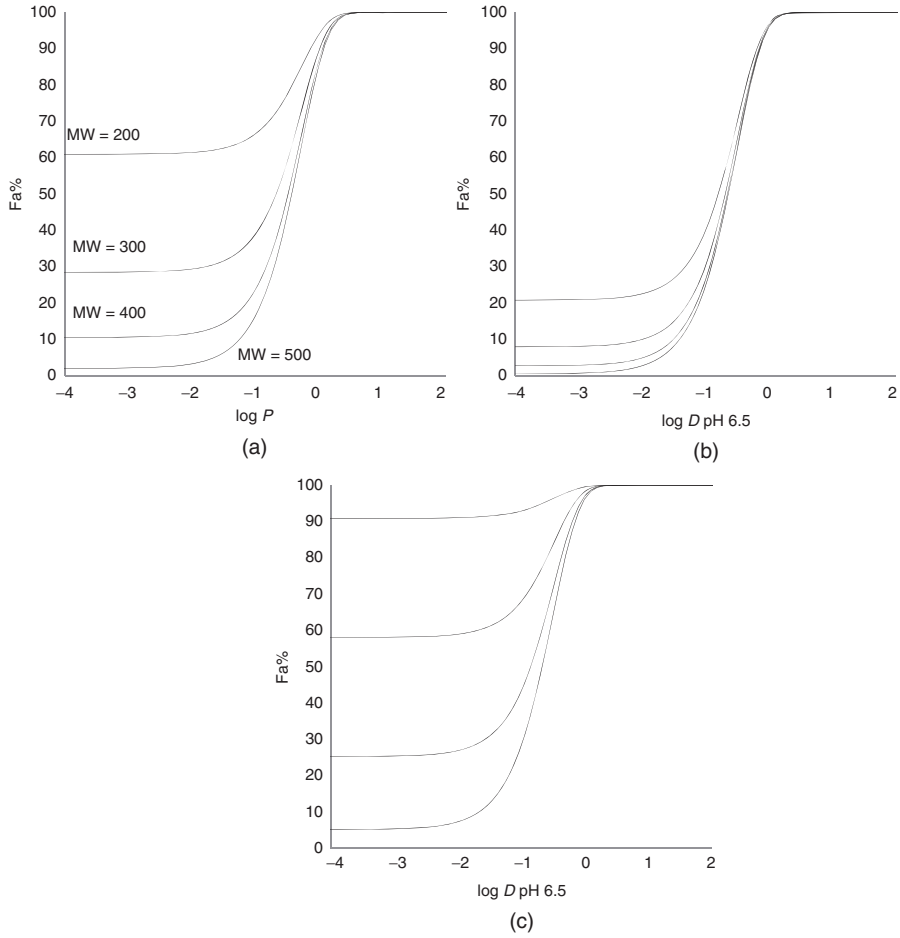

Figure 4.15 Relationship between log D_{oct}, MW, and Fa% theoretically calculated using Equations 4.35–4.39: (a) undissociable drugs, (b) acids, and (c) bases.

However, by applying the steady-state approximation, the net permeability and $f_{u1}C_1$ can be simply calculated without requiring numerical integration [66].

4.9.1 Definition of P_{app}

In an *in vitro* cellular membrane permeation assay, after a short induction time, the concentration in the acceptor chamber increases linearly with time. This means that the concentration in the cytosol achieved a steady state after the induction time. The apparent permeability (P_{app}) is calculated from this linear region as

$$P_{app} = \frac{1}{A_{well} \cdot C_{donor}} \frac{dX_{acceptor}}{dt} \tag{4.39}$$

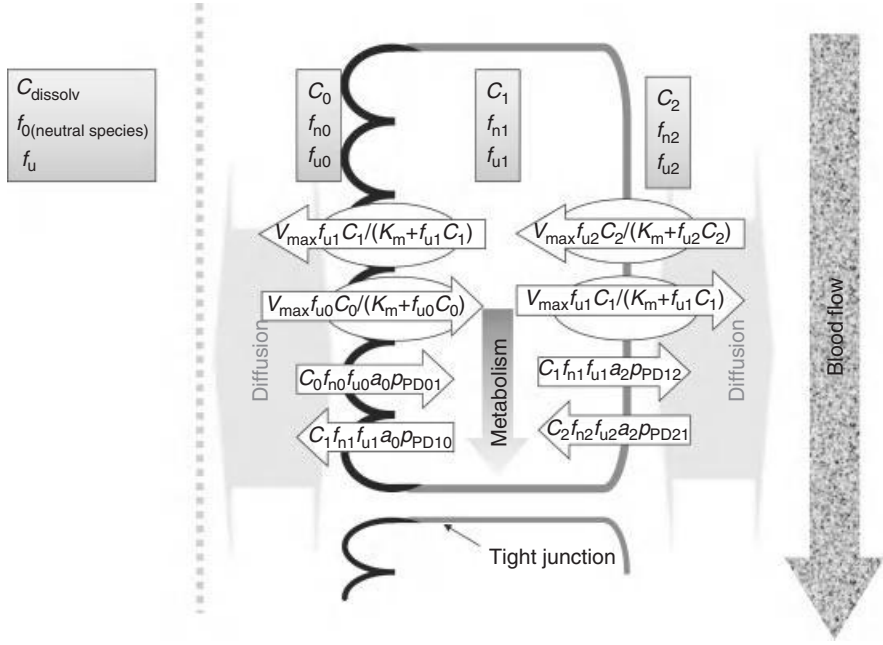

Figure 4.16 Epithelial cells' configuration.

where C_{donor} is the dissolved drug concentration in the donor well, A_{well} is the surface area of the well, and $X_{acceptor}$ is the drug amount in the acceptor well.

In most cases, the steady-state approximation is appropriate mainly because the fluid volume in the cytosol is much smaller than the intestinal fluid.[18] In the following section, the theoretical details of the explicit cell model are discussed based on the steady-state approximation.

4.9.2 Enzymatic Reaction: Michaelis–Menten Equation

Usually, drug permeation by carrier-mediated transport is saturable, is substrate specific, and can be inhibited [67]. Intrinsic carrier-mediated permeability can be expressed as

$$p_{CM} = \frac{J_{max}}{K_m + C_{CM}} \tag{4.40}$$

where J_{max} is the maximum flux, K_m is the Michaelis–Menten constant, and C_{CM} is the effective concentration at the site of a transporter. K_m should be aligned

[18]The steady-state approximation is valid when a steady state is rapidly established in the cytosol compared to the timescale of concentration change in the donor side. Even when the $C_{dissolv}$ changes over time, the steady-state approximation is applicable for each time point. At steady state, the ratio of the concentrations in the donor and cytosol compartments can be approximated to be constant.

with the definition of C_{CM}. When $C_{CM} \ll K_m$,

$$p_{CM} = \frac{J_{max}}{K_m} \tag{4.41}$$

J_{max} is in proportion to the expression level of each enzyme. To correct the difference in the *in vitro* and *in vivo* expression levels,

$$p_{CM,in\ vivo} = \frac{in\ vivo \text{ expression level}}{in\ vitro \text{ expression level}} \times p_{CM,in\ vitro} \tag{4.42}$$

4.9.3 First-Order Case 1: No Transporter and Metabolic Enzymes

In this simplest case, the mass balance equation at the steady state for the cytosol compartment is

$$\begin{aligned}\frac{dX_1}{dt} &= C_0 f_{u0} f_{n0} p_{PD01} a_0 - C_1 f_{u1} f_{n1} p_{PD10} a_0 \\ &\quad - C_1 f_{u1} f_{n1} p_{PD12} a_2 + C_2 f_{u2} f_{n2} p_{PD21} a_2 = 0\end{aligned} \tag{4.43}$$

where

f_n = the fraction of undissociated (uncharged) species;
f_u = the fraction of unbound species;
p = ideal permeability;
C = total dissolved drug concentration in each compartment;
a = absolute surface area;
X = compound amount in each compartment;
PD = passive diffusion;
0, 1, and 2 = compartments in Figure 4.16.

This equation is based on two assumptions:

1. Only the unbound fraction can permeate the membrane (free fraction theory).
2. Only the undissociated molecule can passively permeate the membrane (pH partition theory).

At steady state, the net mass balance in the cytosol can be approximated to be zero at each time point. The drug concentration in the basal side (C_2) is much smaller than that in the apical side and is considered to be negligible ($C_2 = 0$). By rearranging Equation 4.43 for $C_1 f_{u1}$, we obtain,

$$C_1 f_{u1} = C_0 f_{u0} \frac{f_{n0}}{f_{n1}} \frac{p_{PD01} a_0}{p_{10PD} a_0 + p_{12PD} a_2} \tag{4.44}$$

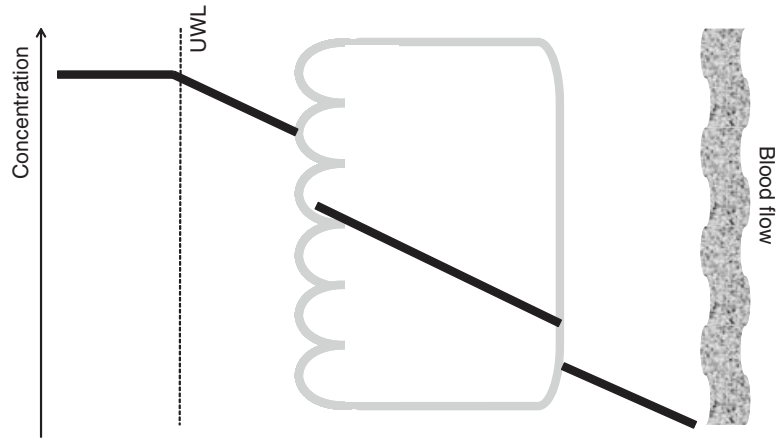

Figure 4.17 Schematic presentation of concentration gradient across the epithelial membrane. The bold line indicates the concentration gradient across the intestinal wall.

This equation can be interpreted as the unbound drug concentration in the cytosol ($C_1 f_{u1}$) is determined by the ratio of undissociated fraction in the apical and cytosol compartments (f_{n0}/f_{n1}), intrinsic passive permeability, unbound fraction in the apical site (f_{u0}), and surface area ($p_{PD01}a_0/(p_{PD10}a_0 + p_{PD12}a_2)$). f_{n0}/f_{n1} can be calculated from the pK_a of a drug and the pH of the apical and the cytosol compartments. Therefore, the information about the bound fraction of a drug in the cytosol (f_{u1}) is not required for calculation of the unbound drug concentration in the cytosol at the steady state.[19] In other words, the concentration gradient of the unbound undissociated species solely determines the passive permeation process. Figure 4.17 shows a schematic presentation of a concentration gradient across the intestinal wall. Figure 4.18 shows the concentration profile of undissociated and dissociated species.

When the passive permeability is symmetric in the influx and efflux directions and is equal in the apical and basal sides (i.e., $p_{PD01} = p_{PD10} = p_{PD12} = p_{PD21} = p_{PD}$),[20] and as the surface area ratio is 1:3 in the epithelial cells [68], Equation 4.44 becomes

$$C_1 f_{u1} = C_0 f_{u0} \frac{f_{n0}}{f_{n1}} \frac{a_0}{a_0 + a_2} = C_0 f_{u0} \frac{1}{4} \frac{f_{n0}}{f_{n1}} \tag{4.45}$$

Therefore, when the pH of the apical and cytosol compartments are equal (e.g., pH 7.4) or a drug is not dissociable, the unbound drug concentration in the cytosol

[19]This situation is the similar in the PK–PD theory, so the cytosol concentration in a target organ can be calculated from the plasma concentration and plasma unbound fraction (when no carrier-mediated transport is involved).

[20]This assumption is supported by the fact that passive *A* to *B* and *B* to *A* permeability values become the same at iso-pH.

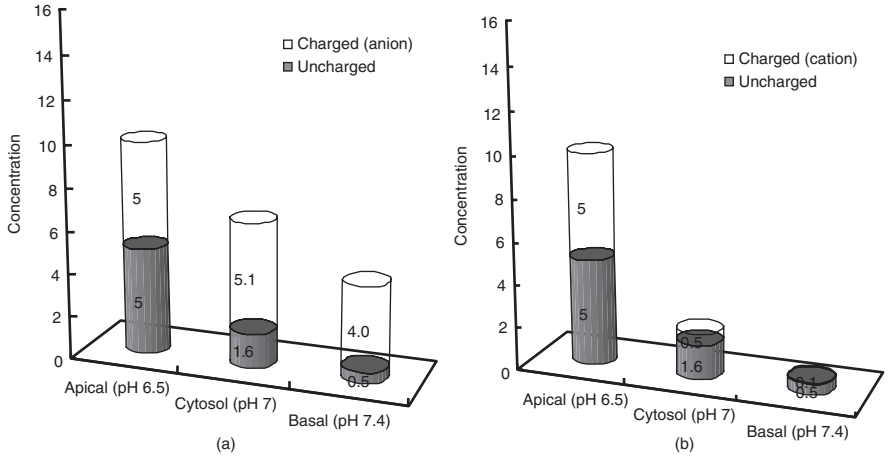

Figure 4.18 The concentration of undissociated and charged species in the epithelial cells. The concentration gradient of unbound undissociated species (gray bar) solely determines the passive permeation processes. (a) Acid and (b) base. (Both have pK_a of 6.5). Concentration gradient of unbound unionized drug molecules determines the passive permeability.

($C_1 f_{u1}$) is one-fourth of that in the apical side ($C_0 f_{u0}$). When the pH is different (e.g., pH 6.0–6.5 in the apical side (acid microclimate pH) and 7.0–7.4 in the cytosol) and a drug is dissociable, the difference in the undissociated fraction should be taken into account. This point is especially important for prediction of drug–drug interaction in the enterocytes (Section 14.2).

Example The unbound drug concentration ratio of cimetidine (cytosol/apical) can be calculated as follows (p$K_a = 6.9$; pH of the apical and cytosol sites = 6.5 and 7.0, respectively; and no bile-micelle binding in the apical side):

$$f_{n0} = \frac{1}{1 + \dfrac{10^{-6.5}}{10^{-6.9}}} = 0.28, \quad f_{n1} = \frac{1}{1 + \dfrac{10^{-7.0}}{10^{-6.9}}} = 0.56$$

$$\frac{C_1 f_{u1}}{C_0 f_{u0}} = \frac{1}{4} \times \frac{0.28}{0.56} = 0.13$$

Using this cytosol concentration, the net permeability can be calculated as follows. At steady state, the flux across the apical membrane becomes equal to the net flux from the apical to basal side.

$$C_0 P_{app} A_{well} = C_0 f_{u0} f_{n0} p_{PD} a_0 - C_1 f_{u1} f_{n1} p_{PD} a_0 \tag{4.46}$$

The LHS of the equation is the macroscopic net flux from the apical side to the basal side (cf. the apparent permeability (P_{app}) is defined based on the flat

surface area of a cell culture well (A_{well}) and the dissolved drug concentration at the apical membrane surface (C_0)). The RHS is the microscopic net flux at the apical membrane. By substituting Equation 4.44 in Equation 4.46, we obtain

$$P_{app} = f_{n0} f_{u0} p_{PD} \frac{1}{A_{well}} \left(\frac{a_0 a_2}{a_0 + a_2} \right) \tag{4.47}$$

This equation can be interpreted as P_{app} is affected by the uncharged and unbound fractions in the apical side (f_{n0} and f_{u0}, respectively), but not by those in the cytosol (f_{n1} and f_{u1} do not appear in this equation).[21] As shown in Figure 4.18, the passive flux is determined only by the concentration gradient of unbound undissociated species [38, 69].[22,23]

4.9.4 First-Order Case 2: Efflux Transporter in Apical Membrane

When $C_1 f_{u1} \ll K_m$, the efflux transport can be treated as the first-order kinetics. For A to B direction, the mass balance in the cytosol at steady state is

$$C_0 f_{u0} f_{n0} p_{PD01} a_0 - C_1 f_{u1} f_{n1} p_{PD10} a_0 - C_1 f_{u1} f_{n1} p_{PD12} a_2 - C_1 f_{u1} p_{efflux} a_0 = 0 \tag{4.48}$$

By rearranging this equation, we obtain

$$C_1 f_{u1} = C_0 f_{u0} \frac{f_{n0}}{f_{n1}} \frac{p_{PD01} a_0}{p_{PD10} a_0 + p_{PD12} a_2 + \dfrac{p_{efflux} a_0}{f_{n1}}} \tag{4.49}$$

On the other hand, from the definition of apparent permeability and flux across the basolateral membrane at steady state, we obtain

$$C_0 P_{app,A-B} A_{well} = C_1 f_{u1} f_{n1} p_{PD12} a_2 - C_2 f_{u2} f_{n2} p_{PD21} a_2 \tag{4.50}$$

In this equation, the flux across the basolateral membrane at steady state (RHS) is equal to the total flux defined as the donor concentration and apparent permeability (LHS). Usually, P_{app} is calculated at the time point where $C_2 \approx 0$

[21] It is often argued that the pH partition theory should be incorrect because the pH in the cytosol is maintained constant (at pH 7.4) regardless of the apical pH and the basolateral permeation of a drug will be the rate-limiting step (main permeation barrier) for an acid (unless otherwise the apical intrinsic passive clearance ($a_0 p_{01}$) is significantly smaller than the basal one ($a_1 p_{12}$)). According to Equation 4.47, pH and unbound fraction in the cytosol does not affect P_{app}, and therefore, regardless of $a_0 p_{01}$ and $a_1 p_{12}$ values, the pH-partition theory is valid. It has been widely experimentally confirmed in the literature that dissociable compounds follow the pH partition theory [38, 39].

[22] Concentration and fraction should not be confused.

[23] In an *in situ* assay and *ex vivo* assay, the pH-dependent permeability of a drug is often not well observed because of the existence of microclimate pH, which is well maintained and little affected by the bulk fluid pH.

and the second term is negligible. By substituting Equation 4.49 in Equation 4.50, we obtain

$$P_{\mathrm{app},A-B} = \frac{C_1 f_{\mathrm{u}1} f_{\mathrm{n}1} p_{\mathrm{PD}12} a_2}{C_0 A_{\mathrm{well}}} = \frac{f_{\mathrm{n}1} p_{\mathrm{PD}12} a_2}{C_0 A_{\mathrm{well}}} C_0 f_{\mathrm{u}0} \frac{f_{\mathrm{n}0}}{f_{\mathrm{n}1}} \frac{p_{\mathrm{PD}01} a_0}{p_{\mathrm{PD}10} a_0 + p_{\mathrm{PD}12} a_2 + \dfrac{p_{\mathrm{efflux}} a_0}{f_{\mathrm{n}1}}}$$

$$= f_{\mathrm{u}0} f_{\mathrm{n}0} \frac{1}{A_{\mathrm{well}}} \frac{p_{\mathrm{PD}01} a_0 p_{\mathrm{PD}12} a_2}{p_{\mathrm{PD}10} a_0 + p_{\mathrm{PD}12} a_2 + \dfrac{p_{\mathrm{efflux}} a_0}{f_{\mathrm{n}1}}} \tag{4.51}$$

In a similar way, for B to A direction,

$$C_2 f_{\mathrm{u}2} f_{\mathrm{n}2} p_{\mathrm{PD}21} a_2 - C_1 f_{\mathrm{u}1} f_{\mathrm{n}1} p_{\mathrm{PD}12} a_2 - C_1 f_{\mathrm{u}1} f_{\mathrm{n}1} p_{\mathrm{PD}10} a_0 - C_1 f_{\mathrm{u}1} p_{\mathrm{efflux}} a_0 = 0 \tag{4.52}$$

$$C_1 f_{\mathrm{u}1} = C_2 f_{\mathrm{u}2} \frac{f_{\mathrm{n}2}}{f_{\mathrm{n}1}} \frac{p_{\mathrm{PD}21} a_2}{p_{\mathrm{PD}12} a_2 + p_{\mathrm{PD}10} a_0 + \dfrac{p_{\mathrm{efflux}} a_0}{f_{\mathrm{n}1}}} \tag{4.53}$$

$$C_2 P_{\mathrm{app},B-A} A = C_2 f_{\mathrm{u}2} f_{\mathrm{n}2} p_{\mathrm{PD}21} a_2 - C_1 f_{\mathrm{u}1} f_{\mathrm{n}1} p_{\mathrm{PD}12} a_2 \tag{4.54}$$

Therefore,

$$P_{\mathrm{app},B-A} = \frac{C_2 f_{\mathrm{u}2} f_{\mathrm{n}2} p_{\mathrm{PD}21} a_2 - C_1 f_{\mathrm{u}1} f_{\mathrm{n}1} p_{\mathrm{PD}12} a_2}{C_2 f_{\mathrm{u}2} A_{\mathrm{well}}}$$

$$= f_{\mathrm{n}2} f_{\mathrm{u}2} \frac{1}{A_{\mathrm{well}}} \left(p_{\mathrm{PD}21} a_2 - \frac{p_{\mathrm{PD}12} a_2 p_{\mathrm{PD}21} a_2}{p_{\mathrm{PD}12} a_2 + p_{\mathrm{PD}10} a_0 + p_{\mathrm{effulx}} a_0 / f_{\mathrm{n}1}} \right) \tag{4.55}$$

When $f_{\mathrm{n}0} = f_{\mathrm{n}2}$ (the iso-pH condition), $f_{\mathrm{u}0} = f_{\mathrm{u}2}$, and $p_{\mathrm{PD}01} = p_{\mathrm{PD}10} = p_{\mathrm{PD}12} = p_{\mathrm{PD}21} = p_{\mathrm{PD}}$, the efflux ratio (ER) becomes

$$\mathrm{ER} = \frac{P_{\mathrm{app},BA}}{P_{\mathrm{app},AB}} = 1 + \frac{p_{\mathrm{efflux}}}{f_{\mathrm{n}1} p_{\mathrm{PD}}} \tag{4.56}$$

This equation is particularly important, as it clearly shows the relationship between ER, passive diffusion, and active efflux transport. By substituting this equation in Equation 4.49, we obtain

$$C_1 f_{\mathrm{u}1} = C_0 f_{\mathrm{u}0} \frac{f_{\mathrm{n}0}}{f_{\mathrm{n}1}} \frac{p_{01} a_0}{p_{10} a_0 + p_{12} a_2 + a_0 p_{01} (\mathrm{ER} - 1)}$$

$$= C_0 f_{\mathrm{u}0} \frac{f_{\mathrm{n}0}}{f_{\mathrm{n}1}} \frac{1}{1 + a_2/a_0 + (\mathrm{ER} - 1)} \tag{4.57}$$

This equation collapses to Equation 4.44 when ER = 1. As the surface area ratio is 1:3 in the epithelial cells [68],

$$C_1 f_{u1} = C_0 f_{u0} \frac{f_{n0}}{f_{n1}} \frac{1}{4 + (\mathrm{ER} - 1)} \tag{4.58}$$

Therefore, the unbound drug concentration in the cytosol under the effect of efflux transporter can be estimated once we have ER data.

An inhibition study is often performed to estimate the effect of an efflux transporter on oral absorption of its substrate. In this case,

$$\frac{P_{app,PD}}{P_{app,A-B}} = 1 + \frac{1}{4}(\mathrm{ER} - 1) \tag{4.59}$$

This equation suggests that an AUC change by inhibiting an apical efflux transporter is much smaller than ER. For example, when ER = 2, the AUC increase by inhibiting the apical efflux transporter will be 1.25.[24] Another merit of this equation is that ER can be estimated from $P_{app,PD}/P_{app,A-B}$ ratio. In many cases of lipophilic P-gp substrates, the $P_{app,B-A}$ exceeds the *in vitro* UWL limitation (Section 7.9.8), while $P_{app,A-B}$ and $P_{app,PD}$ remain within it. In this case, Equation 4.59 can be used to calculate ER unaffected by the UWL. In addition, if $P_{app,PD}$ is not available, it can be estimated from $P_{app,A-B}$ and ER (when $P_{app,B-A} \ll in\ vitro P_{UWL}$).

From Equation 4.59,

$$p_{efflux} = f_{n1} p_{PD}\ (\mathrm{ER} - 1) \tag{4.60}$$

$$A_{well} \cdot p_{efflux} \equiv P_{effux} = \frac{J_{max}}{K_m} = A f_{n1} p_{PD} (\mathrm{ER} - 1)$$

$$\equiv P_{app,PD} \left(\frac{a_0 a_2}{a_0 + a_2} \right) (\mathrm{ER} - 1) \tag{4.61}$$

Using Equations 4.59 and 4.61, we can estimate K_m/J_{max} both *in vitro* and *in vivo*. It would be appropriate to assume that K_m is similar *in vivo* and *in vitro*. Therefore, the difference in the expression levels can be estimated by comparing *in vitro* and *in vivo* J_{max} values. This enables mechanistic *in vitro–in vivo* extrapolation.

In Figure 4.19, *in vitro* p_{efflux} was plotted against $f_{n1} \times p_{PD}$ for structurally diverse drugs. P_{app} data were collected from the literature [70–73]. The following methods were used to estimate p_{efflux}: (i) when $P_{app,PD}$, $P_{app,A-B}$, and $P_{app,B-A}$ are all available and below the UWL limitation, they are used to calculate $f_{n1} \times p_{PD}$ and p_{efflux}; (ii) when $P_{app,B-A}$ exceeded the UWL limitation, while $P_{app,PD}$ and $P_{app,A-B}$ did not, Equation 4.59 was used to calculate ER; and (iii) when $P_{app,PD}$

[24]Therefore, when considering the bioequivalence (0.8–1.25 AUC and C_{max}) of oral absorption with and without inhibition, ER = 2 would be a good criteria.

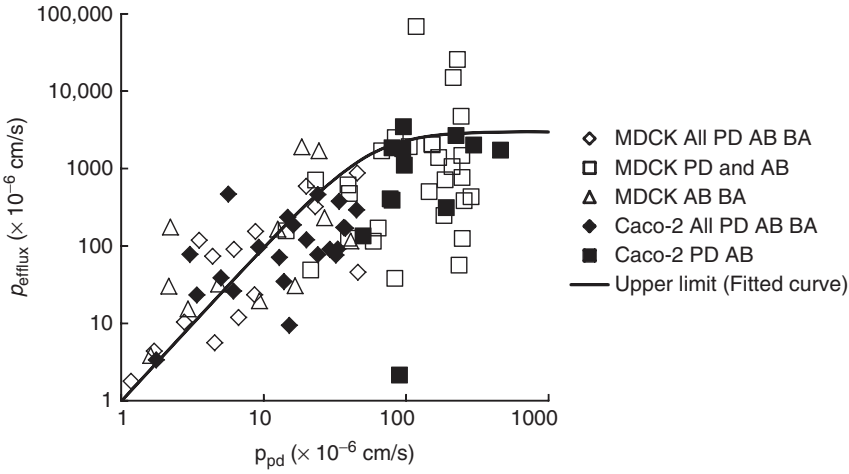

Figure 4.19 $p_{efflux}-p_{PD}$ relationship.

is not available but $P_{app,A-B}$ and $P_{app,B-A}$ are both below the UWL limitation, $P_{app,PD}$ is calculated from $P_{app,A-B}$ and ER using Equation 4.59. The half of the highest permeability observed in the system was used as the UWL limiting criteria. All experiments were performed at pH 7.4 in both apical and basal sides (hence, $f_{n0} = f_{n1} = f_{n2}$) without any solubilizers ($f_{u0} = f_{u2} = 1$).

As shown in Figure 4.19, a correlation was observed between p_{efflux} and $f_{n1} \times p_{PD}$. This is in good agreement with the suggested mechanism of P-gp that the efflux transport is the sequence of the passive membrane partitioning step and active transmembrane transport step (Fig. 4.20) [74]. The trend line in Figure 4.19 is

$$p_{efflux} \leq \left[\frac{0.2}{(f_{n1} \times p_{PD})^2} + \frac{1}{500} \right]^{-1} \tag{4.62}$$

where the unit of both p_{efflux} and $f_{n1} \times p_{PD}$ is 10^{-6} cm/s. Using this trend line, the maximum effect of P-gp on P_{ep}, P_{eff}, and Fa% can be calculated. Figure 4.21b shows the maximum increase of P_{ep}, P_{eff}, and Fa% by P-gp inhibition for undissociable drugs. Equations 4.35 and 4.62 were used to calculate $P_{trans,0}$ and maximum p_{efflux}, respectively. It was suggested that maximum ratio of P_{ep} would be ca. 7 (inhibition/no inhibition) for moderately lipophilic indissociable drugs, whereas when passive P_{ep} is higher than 3×10^{-3} cm/s (log D_{oct} of ca. 2.5), the P-gp effect on net P_{ep} should be minimum. Furthermore, at passive $P_{ep} > 2 \times 10^{-4}$ cm/s (log D_{oct} of ca. 1.25), the minimum value of net P_{ep} becomes ca. 50×10^{-6} cm/s and the UWL would become the limiting step, hence P-gp inhibition would have little effect on total P_{eff} and complete oral absorption is anticipated even when the drug is a P-gp substrate. These theoretical suggestions are in good agreement with the

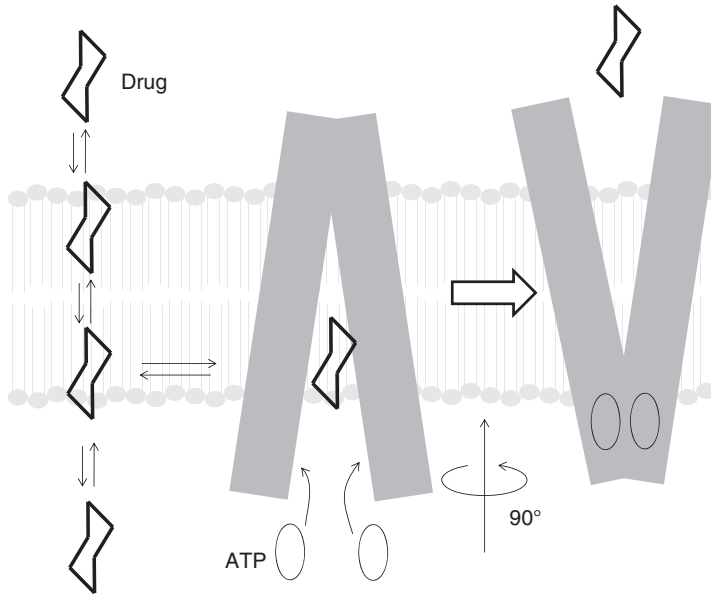

Figure 4.20 Model of substrate transport by P-gp [74]. A substrate drug partitions into the bilayer and enters the internal drug-binding pocket through an open portal. ATP binding induces a large conformational change, opening the drug-binding site to the extracellular space.

experimental observations that when the passive P_{ep} is high, P-gp has little or no effect on the *in vitro* ER [75] and *in vivo* total absorption (Section 14.4.2).

In addition, the P-gp effect would be larger for basic drugs compared to indissociable and acid drugs in *in vivo* situation (Fig. 4.22). This is due to the difference in the apical and cytosol pH. When the apical pH is changed from 7.4 to 6.5, the passive influx of a basic drug becomes ca. 10-fold smaller while P-gp efflux remains the same (as the cytosol pH remains the same). Maximum P-gp inhibition effect on Fa% (ca. sevenfold) would be observed for a basic drug with moderate permeability.

4.9.5 Apical Efflux Transporter with K_m and V_{max}

To calculate the nonlinear effect of efflux transporter, the Michaelis–Menten equation can be incorporated into the explicit cell model. In this case, the mass balance in the cell compartment can be written as

$$\frac{dM_1}{dt} = C_0 f_{n0} f_{u0} a_0 p_{PD01} - C_1 f_{n1} f_{u1} a_0 p_{PD10} - C_1 f_{n1} f_{u1} a_2 p_{PD12}$$

$$+ C_2 f_{n2} f_{u2} a_2 p_{PD21} - \frac{V_{max\,10} C_1 f_{u1}}{K_{m10} + C_1 f_{u1}} = 0 \tag{4.63}$$

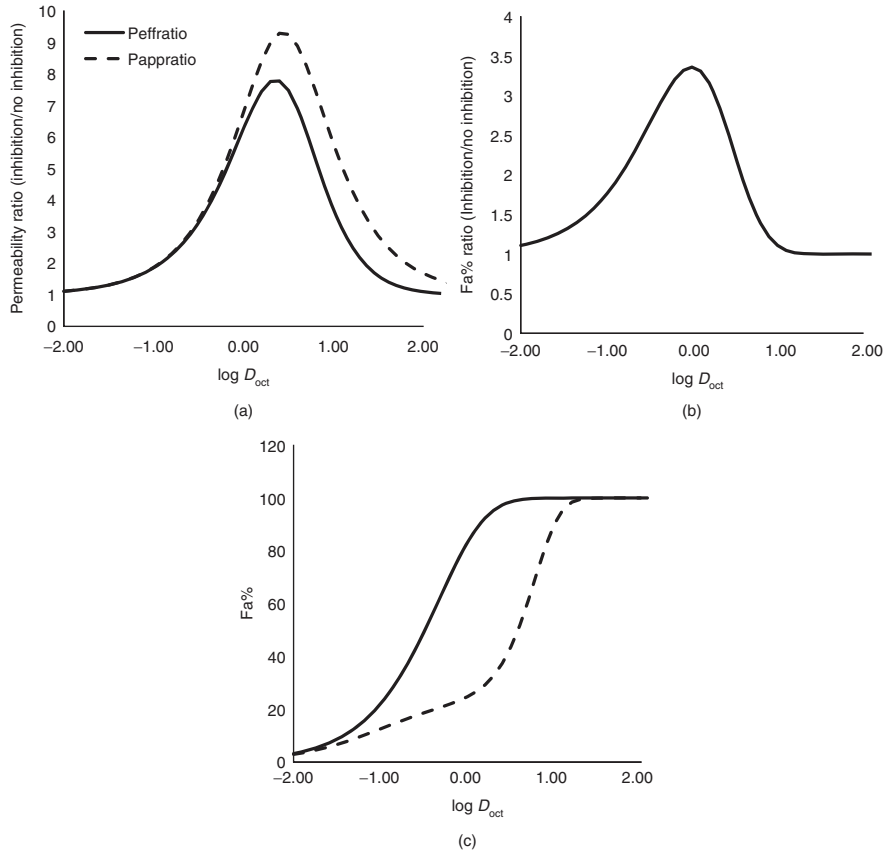

Figure 4.21 Maximum effect of P-gp inhibition on P_{eff} and Fa% (without low solubility and dissolution rate limitation, paracellular permeation, and bile-micelle binding ($f_u = 1$)). (a) P_{eff} ratio, (b) Fa% ratio, and (c) Fa%. PE = 3, VE = 10, $h_{UWL} = 0.03$ cm, $D_{mono} = 7 \times 10^{-6}$ cm/s, $H_{villi} = 0.06$ cm, $W_{channel} = 0.02$ cm, $W_{villli} = 0.05$ cm, and $P_{WC} = 0.23 \times 10^{-5}$ cm/s.

where K_{m10} is the intrinsic Michaelis constant of an efflux transporter in the apical membrane. By rearranging Equation 4.63,

$$\begin{aligned}
&(C_1 f_{u1})^2 (f_{n1} a_0 p_{10} + f_{n1} a_2 p_{12}) \\
&\quad + (C_1 f_{u1}) \left[K_{m10} (f_{n1} a_0 p_{10} + f_{n1} a_2 p_{12}) \right. \\
&\quad \left. + V_{max\,10} - (C_0 f_{n0} f_{u0} a_0 p_{01} + C_2 f_{n2} f_{u2} a_2 p_{21}) \right] \\
&\quad - K_{m10} (C_0 f_{n0} f_{u0} a_0 p_{01} + C_2 f_{n2} f_{u2} a_2 p_{21}) = 0
\end{aligned} \tag{4.64}$$

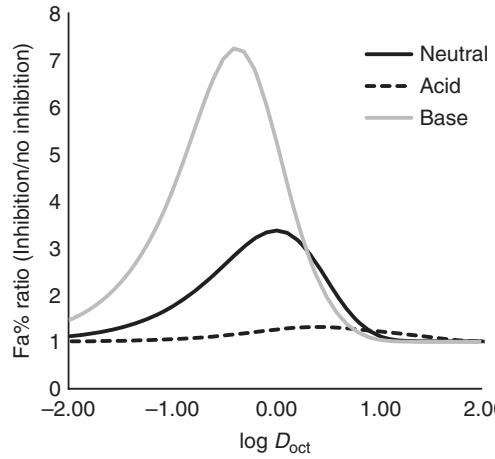

Figure 4.22 Maximum effect of P-gp inhibition on Fa% for undissociable, acid and base drugs. pK_a was set to 4 and 9 for acids and bases, respectively. Other conditions are the same with Figure 4.21.

This is a quadratic equation for $C_1 f_{u1}$. By solving Equation 4.64, $C_1 f_{u1}$ can be obtained as

$$C_1 f_{u1} = \frac{-b' + \sqrt{b^{2\prime} - 4a'c'}}{2a'} \tag{4.65}$$

$$a' = f_{n1} a_0 p_{10} + f_{n1} a_2 p_{12} \tag{4.66}$$

$$b' = K_{m10} a' + V_{max\,10} + \frac{c'}{K_{m10}} \tag{4.67}$$

$$c' = -K_{m10}(C_0 f_{n0} f_{u0} a_0 p_{01} + C_2 f_{n2} f_{u2} a_2 p_{21}) \tag{4.68}$$

On the other hand, from the definition of $P_{app,A-B}$ (LHS of Eq. 4.69) and the mass transfer into the basal compartment (RHS of Eq. 4.69), we obtain

$$C_0 P_{app,A-B} A_{well} = C_1 f_{n1} f_{u1} a_2 p_{12} - C_2 f_{n2} f_{u2} a_2 p_{21} \tag{4.69}$$

Similarly,

$$C_2 P_{app,B-A} A_{well} = C_2 f_{n2} f_{u2} a_2 p_{21} - C_1 f_{n1} f_{u1} a_2 p_{12} \tag{4.70}$$

For apical to basal permeation, assuming a sink condition in the basal side ($C_2 = 0$), we obtain

$$P_{\mathrm{app,ep},A-B} = \frac{1}{C_0 A_{\mathrm{well}}} f_{\mathrm{n1}} a_2 p_{12} (C_{\mathrm{l}} f_{\mathrm{u1}}) \tag{4.71}$$

Similarly, for $P_{\mathrm{app},B-A}$,

$$P_{\mathrm{app,ep},B-A} = \frac{1}{C_2 A_{\mathrm{well}}} [C_2 f_{\mathrm{n2}} f_{\mathrm{u2}} a_2 p_{21} - (C_{\mathrm{l}} f_{\mathrm{u1}}) f_{\mathrm{n1}} a_2 p_{12}] \tag{4.72}$$

In these equations, C_0 and C_2 are the donor concentrations for $P_{\mathrm{app},A-B}$ and $P_{\mathrm{app},B-A}$, respectively. By substituting Equation 4.65 ($C_{\mathrm{l}} f_{\mathrm{u1}}$) in Equations 4.71 and 4.72, $P_{\mathrm{app},A-B}$ and $P_{\mathrm{app},A-B}$ can be calculated.

Figure 4.23 is the schematic explanation of the concentration–P_{app} curve calculated using Equations 4.62–4.72. In many cases of efflux transporter substrates, an asymmetric concentration–P_{app} curve is observed between the A to B and B to A permeations. This asymmetry is caused by the differences in the passive clearance of the apical and basolateral membranes. Figure 4.24 shows the fitted curve for rhodamin123 and fexofenadine. In addition, the difference in expression level can change the apparent K_{m} value as the cytosol concentration changes depending on the P-gp expression level [64, 76, 77]. Figure 4.25 shows the fitted curve for vinblastine with a single intrinsic K_{m} value.

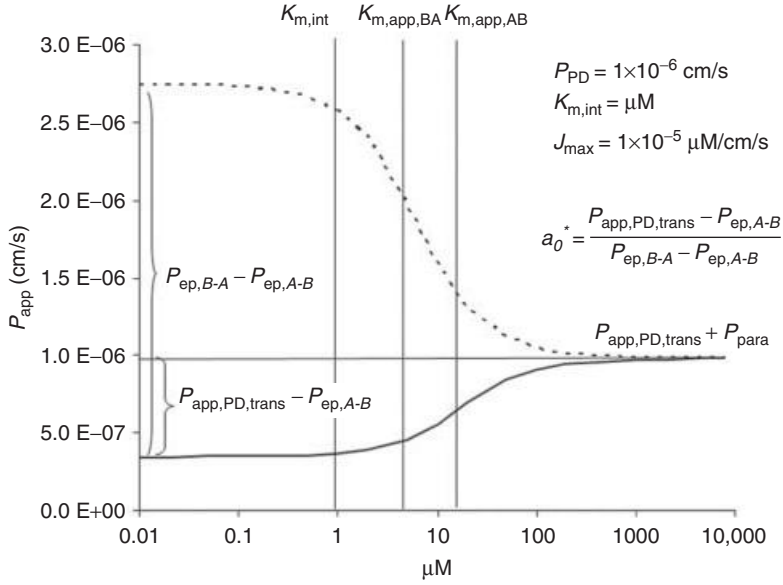

Figure 4.23 Schematic explanation of the concentration–P_{app} curve with an efflux transporter in the apical membrane. *Source:* Adapted from Reference 66 with permission.

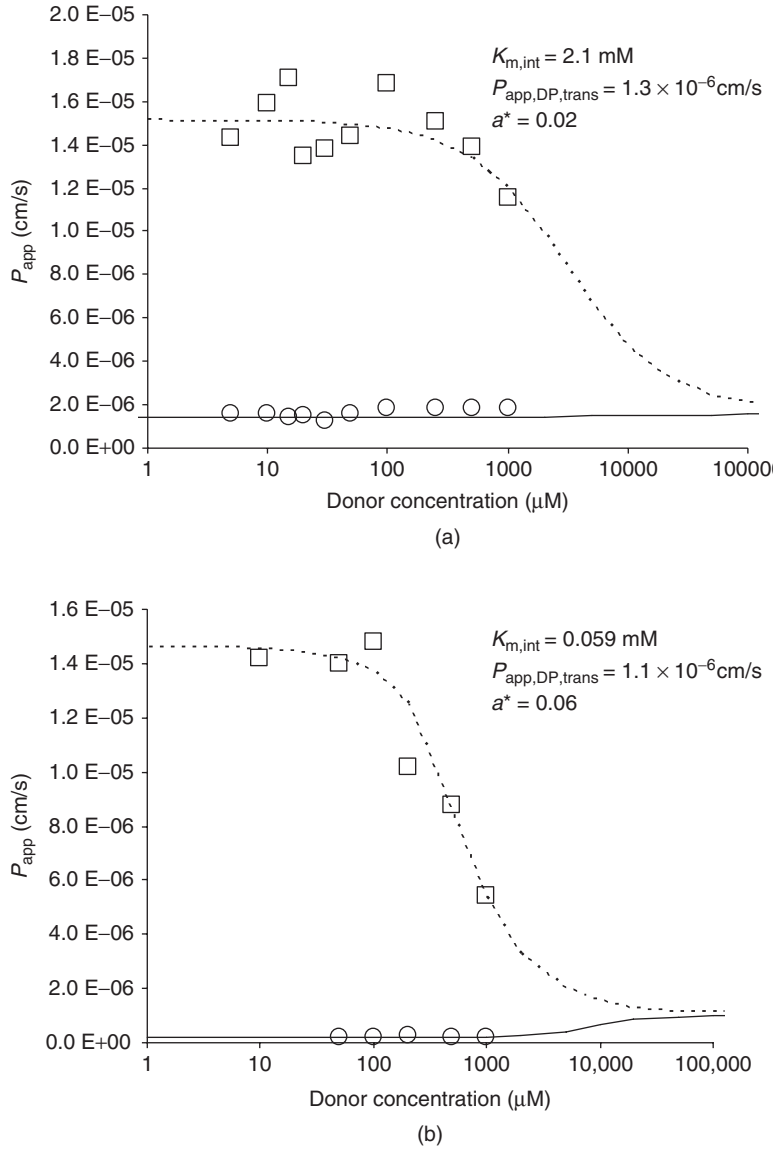

Figure 4.24 Experimental and simulated concentration–P_{app} curves of rhodamin123 and fexofenadine [66, 78, 79]. (a) Rhodamine 123 and (b) Fexofenadine. *Source:* Adapted from Reference 66 with permission.

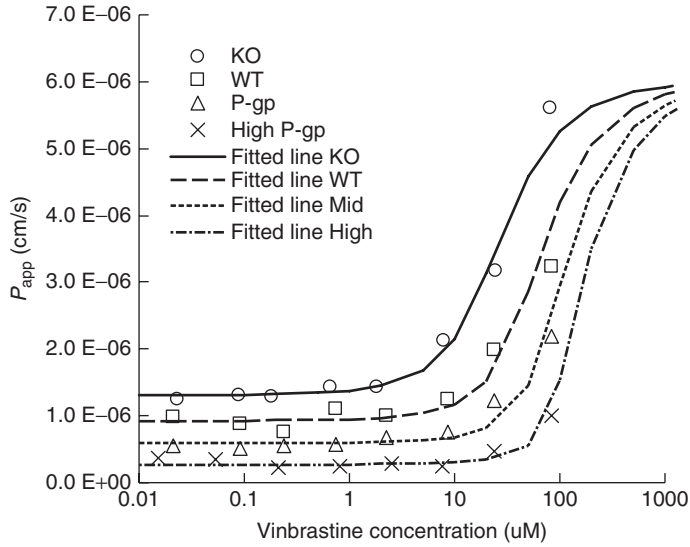

Figure 4.25 Expression-level dependency of vinblastine permeability [66, 77]. *Source:* Adapted from Reference 66 with permission.

4.9.6 Apical Influx Transporter with K_m and V_{max}

When an apical influx transporter is involved in the membrane permeation, $P_{app,A-B}$ can be expressed as

$$P_{app,A-B} = \frac{J_{max}}{K_{m01} + C_0 f_{u0}} + P_{trans,PD} \tag{4.73}$$

When an apical influx transporter is coparticipating in the drug transport with an apical efflux transport, the effect of the apical influx transporter can be taken into account by replacing Equation 4.68 with

$$c' = -K_m \left(C_0 f_{n0} f_{u0} a_0 p_{01} + \frac{V_{max\,01} C_0 f_{u0}}{K_{m01} + C_0 f_{u0}} + C_2 f_{n2} f_{u2} a_2 p_{21} \right) \tag{4.74}$$

4.9.7 UWL and Transporter

In the above discussions of explicit cell models, the UWL is neglected. To consider the UWL effect, the following condition can be additionally introduced:

$$(C_{dissolv} - C_0) P_{UWL} - C_0 P_{ep} = 0 \tag{4.75}$$

where C_0 is the concentration adjacent to the apical membrane in the apical chamber. This equation means that at steady state, the flux across the UWL (first term) is equal to the flux across the epithelial membrane.

4.9.7.1 No Transporter. With no transporter, by rearranging Equation 4.75, C_0/C_{dissolv} can be calculated as

$$\frac{C_0}{C_{\text{dissolv}}} = \frac{P_{\text{UWL}}}{P_{\text{UWL}} + P_{\text{ep}}} \tag{4.76}$$

When $P_{\text{UWL}} < P_{\text{ep}}$, the drug concentration at the epithelial membrane surface (C_0) is significantly smaller than C_{dissolv} because of the concentration gradient across the UWL. Furthermore, the $f_{\text{u1}}C_1$ can be 3- to 10-fold lower than $f_{\text{u0}}C_0$ for neutral and base cases (for acids, $f_{\text{u0}}C_0/f_{\text{u1}}C_1 = 2$). Therefore, to saturate or inhibit a metabolic enzyme in the cytosol, the concentration in the donor side should be significantly higher than the intrinsic K_{m} and K_{i} values. When predicting the drug–drug interaction, these concentration gradients across the UWL and the epithelial membrane should be taken into account (Section 14.2.2).

4.9.7.2 Influx Transporter and UWL. With an apical influx transporter, Equations 4.73 and 4.75 can be solved as a quaternary equation (cf. P_{ep} is a function of C_0 for nonlinear cases) [80, 81].

$$C_0 f_{\text{u0}} = \sqrt{\frac{q^2 r^2}{4} + qK_{\text{m01}}C_{\text{dissolv}}f_{\text{u0}}} - \frac{q \cdot r}{2} \tag{4.77}$$

$$P_{\text{app},A-B} = P_{\text{UWL}}\left(1 - \frac{C_0 f_{\text{u0}}}{C_{\text{dissolv}}}\right) \tag{4.78}$$

$$q = \frac{P_{\text{UWL}}}{P_{\text{UWL}} + P_{\text{trans,PD}}},\ r = \frac{K_{\text{m01}}}{q} + \frac{J_{\max}}{P_{\text{UWL}}} - C_{\text{dissolv}}f_{\text{u0}} \tag{4.79}$$

Figure 4.26 shows the concentration–$P_{\text{app},A-B}$ relationship with an apical influx transporter. If the UWL effect is neglected in the intrinsic K_{m} calculation, the intrinsic K_{m} value is overestimated (apparent K_{m} > intrinsic K_{m}).

4.9.7.3 Efflux Transporter. In this case, the theoretical treatment to handle the UWL effect together with a saturable efflux transport is complicated and a simple open solution cannot be obtained. However, the following process can be used to calculate P_{app}. At steady state,

$$(C_{\text{dissolv}} - C_0)P_{\text{UWL}} - C_0 P_{\text{ep}} = 0 \tag{4.80}$$

$$P_{\text{ep}} = f(C_0) \tag{4.81}$$

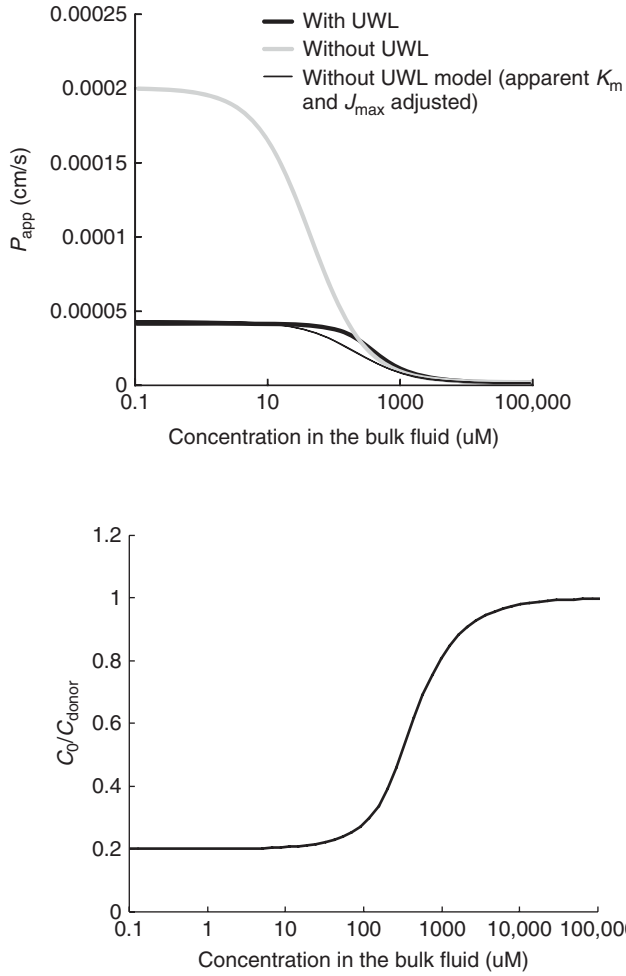

Figure 4.26 The effect of UWL on total permeability of apical influx transporter substrate. $P_{active} = 200 \times 10^{-6}$ cm/s, $K_m = 50$ μm, and $P_{UWL} = 50 \times 10^{-6}$ cm/s. No passive diffusion.

From this condition, the C_0 value satisfying Equation 4.80 can be seeked, for example, using the Newton method or the simplex method.[25] Once C_0 is obtained, P_{app} can be calculated as

$$P_{app} = \frac{C_0}{C_{dissolv}} P_{ep} \tag{4.82}$$

[25] *In Vivo* P_{eff} can be obtained in the same way, but surface area (fold and villi) and bile-micelle-unbound fraction should be taken into account.

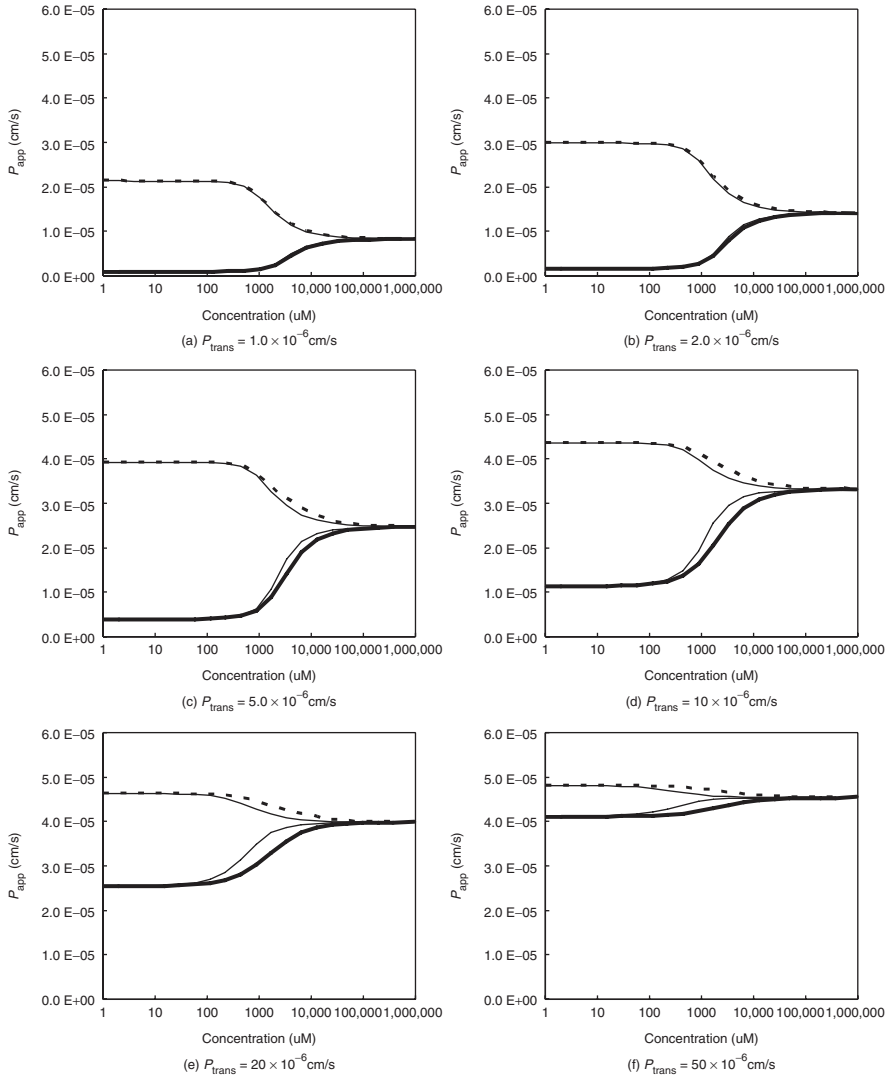

Figure 4.27 The effect of the UWL on the total permeability of an efflux transport substrate. Keys are shown in (a). $K_m = 50$ μM and $P_{UWL} = 50 \times 10^{-6}$ cm/s. Passive permeation (P_{trans}) was changed from 1 to 50×10^{-6} cm/s. p_{efflux} was calculated using Equation 4.62.

Figure 4.27 shows the effect of P_{UWL} on P_{app}.

4.10 GUT WALL METABOLISM

The gut wall metabolism could be significant especially for CYP3A4 and UGT substrates. Various methods to predict Fg (fraction not metabolized in the gut

wall) for CYP3A4 substrates have been reported in the literature [82–85]. In this section, two models that have been reported in the literature are first discussed and then the anatomical Fg model is introduced. These models can be used when the unbound drug concentration in the cytosol is lower than the K_m of CYP3A4. For more advanced simulation, differential equations for an explicit epithelial cell model can be numerically solved [65].

4.10.1 The Q_{gut} Model

Yang et al. introduced the "Q_{gut} model" based on an analogy to the well-stirred model [83, 83].

$$Fg = \frac{Q_{gut}}{Q_{gut} + f_{u1}CL_{met,int}} \tag{4.83}$$

$$Q_{gut} = \left(\frac{1}{PS_{perm}} + \frac{1}{Q_{villi}}\right)^{-1} \tag{4.84}$$

where Q_{villi} is the villi blood flow (18 l/h for humans). In the Q_{gut} model, PS_{perm} was defined based on the effective intestinal membrane permeability and calculated as, PS_{perm} = intestinal smooth surface area (0.66 m^2) × P_{eff}. P_{eff} is estimated from the *in vitro* P_{app} (MDCK and Caco-2) by simple linear regression. It was reported that $f_{u1} = 1$ gave the best prediction results, rather than using the plasma unbound fraction (f_{up}) as the surrogate for f_{u1} (i.e., assuming $f_{u1} = f_{up}$). However, the reason was not identified in the report [83]. A possible reason for this discrepancy is discussed later. Figure 4.29 shows the reported Fg predictability by the Q_{gut} model assuming $f_{u1} = 1$ [83].

4.10.2 Simple Fg Models

Kato [82] proposed a simple equation to estimate Fg from the intrinsic hepatic clearance.

$$Fg = \frac{402}{402 + CL_{h,int}} \tag{4.85}$$

This equation would be valid for CYP3A substrates with high membrane permeability.

4.10.3 Theoretical Consideration on Fg

In this section, to understand the background of the Q_{gut} model and other models, a theoretical equation is derived from the anatomy of the epithelial cells and intestinal villi. As the derivation of the Q_{gut} model from the anatomical perspective was not disclosed in the original paper, we attempt to reproduce a derivation process possibly studied by the original investigator.

4.10.3.1 Derivation of the Fg Models. As shown in Figure 4.28, Fg is basically determined as the ratio of the metabolism rate ($k_{met} \times C_1 \times V_1$; V_1, fluid volume in the cell) and the escaping rate via the basolateral membrane ($k_{esc} \times C_1 \times V_1$). As the escaping rate becomes faster, the Fg becomes larger and approaches 1. This is the main concept applied in all the Fg models. Fg is interpreted as the ratio of the escaping rate in the total rate.

$$\mathrm{Fg} = \frac{k_{esc} C_1 V_1}{k_{met} C_1 V_1 + k_{esc} C_1 V_1} = \frac{C_1 f_{u1} \mathrm{CL}_{esc,int}}{C_1 f_{u1} \mathrm{CL}_{met,int} + C_1 f_{u1} \mathrm{CL}_{esc,int}}$$

$$= \frac{\mathrm{CL}_{esc,int}}{\mathrm{CL}_{met,int} + \mathrm{CL}_{esc,int}} \tag{4.86}$$

Both metabolism and basolateral membrane permeation are driven by the unbound drug concentration. Therefore, in this equation, f_{u1} is canceled out in the numerator and dominator. The escaping process from the cytosol is the sequential process of the basolateral membrane permeation, diffusion from the basolateral membrane to the capillary vessels, and conveyance by the blood flow. One of these three steps can be the rate-limiting step.

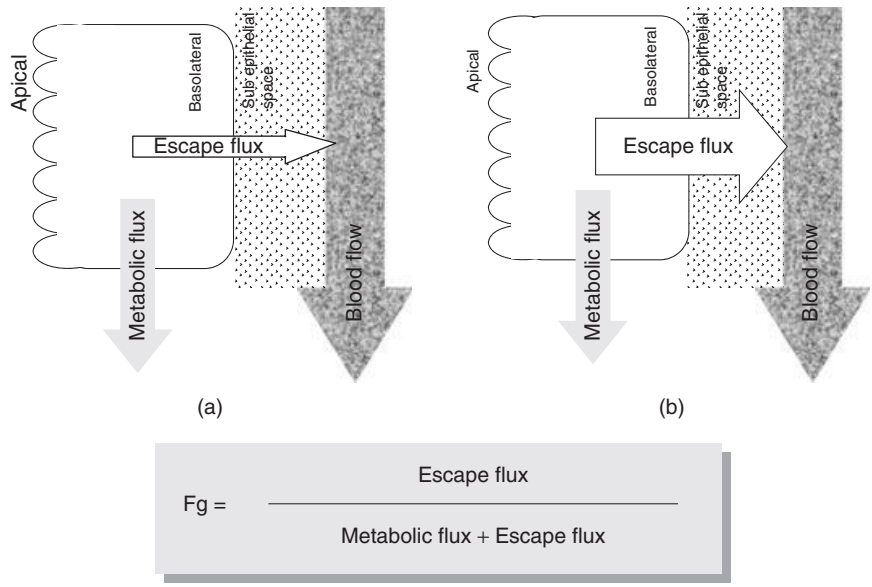

Figure 4.28 Schematic presentation of the relationship between Fg, metabolic flux, and escape flux of a drug. (a) Low Fg and (b) high Fg.

Basolateral Membrane Permeation Limited. When the permeation clearance of the basolateral membrane is much slower than the following processes,

$$\mathrm{Fg} = \frac{\mathrm{PS}_{\mathrm{baso,int}}}{\mathrm{CL}_{\mathrm{met,int}} + \mathrm{PS}_{\mathrm{baso,int}}} \tag{4.87}$$

where $\mathrm{PS}_{\mathrm{baso,int}}$ is the basolateral permeation clearance of unbound drug molecules. For passive diffusion, $\mathrm{PS}_{\mathrm{baso,int}}$ can be calculated as $\mathrm{PS}_{\mathrm{baso,int}} = a_2 p_{\mathrm{PD12}}$. In this case, correction for f_{u1} is not required (i.e., $f_{\mathrm{u1}} = 1$), which in good agreement with the findings by Yang et al. [83].

Blood Flow Limited. When the basolateral membrane permeation and subepithelial diffusion are infinitely fast, the escaping rate is limited by the blood flow. The escaping rate becomes equal to the blood flow elimination rate of a drug. Therefore,

$$C_1 f_{\mathrm{u1}} \mathrm{CL}_{\mathrm{esc,int}} = Q_{\mathrm{villi}} C_{\mathrm{p}} \tag{4.88}$$

The LHS of the equation is the escaping rate, and the RHS is the blood flow elimination rate. At this limiting condition, the unbound concentration in the cytosol and plasma becomes the same because equilibrium is rapidly established between the cytosol and plasma.

$$f_{\mathrm{u1}} C_1 = f_{\mathrm{up}} C_{\mathrm{p}} \tag{4.89}$$

where f_{up} is the unbound fraction in the plasma. Therefore, by substituting Equation 4.89 in Equation 4.88, $\mathrm{CL}_{\mathrm{esc,int}}$ becomes

$$\mathrm{CL}_{\mathrm{esc,int}} = \frac{Q_{\mathrm{villi}} C_{\mathrm{p}}}{C_1 f_{\mathrm{u1}}} = \frac{Q_{\mathrm{villi}} C_{\mathrm{p}}}{f_{\mathrm{up}} C_{\mathrm{p}}} = \frac{Q_{\mathrm{villi}}}{f_{\mathrm{up}}} \tag{4.90}$$

Intermediate Cases between Basolateral Permeability and Blood Flow Limited. By comparing these two cases, a general equation to cover both cases should be

$$\mathrm{CL}_{\mathrm{esc,int}} = \left(\frac{1}{\mathrm{PS}_{\mathrm{baso,int}}} + \frac{1}{Q_{\mathrm{villi}}/f_{\mathrm{up}}} \right)^{-1} \tag{4.91}$$

When $a_2 p_{12} \gg Q_{\mathrm{villi}}/f_{\mathrm{up}}, \mathrm{CL}_{\mathrm{esc,int}} = Q_{\mathrm{villi}}/f_{\mathrm{up}}$, whereas $\mathrm{CL}_{\mathrm{esc,int}} = \mathrm{PS}_{\mathrm{baso,int}}$ when $\mathrm{PS}_{\mathrm{baso,int}} \ll Q_{\mathrm{villi}}/f_{\mathrm{up}}$. To derive the Q_{gut} model, the apparent permeation clearance from the basolateral membrane ($\mathrm{PS}_{\mathrm{perm}}$) can be defined based on C_1.

$$\mathrm{CL}_{\mathrm{esc,int}} = \left(\frac{1}{\mathrm{PS}_{\mathrm{perm}}/f_{\mathrm{u1}}} + \frac{1}{Q_{\mathrm{villi}}/f_{\mathrm{up}}} \right)^{-1} \tag{4.92}$$

If we assume, $f_{u1} = f_{up}$ and rearrange Equation 4.92 and substitute it in Equation 4.86, we can obtain an equation identical to the Q_{gut} model.

$$f_{u1}CL_{esc,int} = \left(\frac{1}{PS_{perm}} + \frac{1}{Q_{villi}}\right)^{-1} \equiv Q_{gut} \tag{4.93}$$

$$Fg = \frac{CL_{esc,int}}{CL_{met,int} + CL_{esc,int}} = \frac{Q_{gut/f_{u1}}}{CL_{met,int} + Q_{gut}/f_{u1}} = \frac{Q_{gut}}{f_{u1}CL_{met,int} + Q_{gut}} \tag{4.94}$$

However, the definition of PS_{perm} is ambiguous in the Q_{gut} model. Yang et al. [83] reported that $f_{u1} = 1$ gave the best prediction, whereas the assumption $f_{u1} = f_{up}$ gave poor prediction. This is in good agreement with the basolateral permeation limited cases but disagrees with the blood flow limited cases.

4.10.3.2 Derivation of the Anatomical Fg Model. In the Q_{gut} model, the diffusion in the subepithelial space is neglected. If the subepithelial space diffusion is the rate-limiting step, based on the similar discussion with the blood flow limited case,

$$C_1 f_{u1} CL_{esc,int} = CL_{subepithelial} C_{subepithelial} \tag{4.95}$$

$$f_{u1} C_1 = f_{subepithelial} C_{subepithelial} \tag{4.96}$$

$$CL_{esc,int} = \frac{CL_{subepithelial} C_{subepithelial}}{C_1 f_{u1}} = \frac{CL_{subepithelial}}{f_{up}} \tag{4.97}$$

where $CL_{subepithelial}$ is the permeation clearance of the subepithelial space and $C_{subepithelial}$ is the concentration and unbound fraction of a drug in the subepithelial space. In this case, the fluid in the subepithelial space was assumed to be the same as the plasma ($f_{subepithelial} = f_{up}$). The diffusion clearance in the subepithelial space is

$$CL_{subepithelial} = A_{blood\ vessel} \frac{D_{mono} f_{up} + D_{albumin}(1 - f_{up})}{h_{subepithelial}} \tag{4.98}$$

where $h_{subepithelial}$ is the thickness of the subepithelial space. This clearance is based on the total concentration in the subepithelial space and the surface area of the blood vessel in the villi ($A_{blood\ vessel}$). $CL_{subepithelial}$ becomes relatively constant when $f_{up} < 0.05$ and is mainly determined by the diffusion coefficient of albumin-bound drug molecules ($D_{albumin} = 6.6 \times 10^{-7}$ cm^2/s).

When we combine the three limited cases into one general equation, it becomes

$$CL_{esc,int} = \left(\frac{1}{PS_{baso,int}} + \frac{1}{CL_{subepithelial}/f_{up}} + \frac{1}{Q_{villi}/f_{up}}\right)^{-1} \tag{4.99}$$

This is called the *anatomical Fg model* in this book. The next step is to assess which process tends to become the rate-limiting step, the subepithelial diffusion or the blood flow. Considering the villi structure (Fig. 6.2), the $h_{\text{subepithelial}}$ would be approximately 50 μm and $A_{\text{blood vessel}}$ is approximately 100 cm^2 in humans. In this case, $\text{CL}_{\text{subepithelial}}$ is likely to be smaller than Q_{villi}. $\text{CL}_{\text{subepithelial}}$ value becomes relatively constant, ca. 2–4 ml/min/kg at $f_{\text{u1}} < 0.05$ ($h_{\text{subepithelial}} = 50$ μm and $A_{\text{blood vessel}} = 88.4$ cm^2 (12.6 cm^2/ kg)). This $\text{CL}_{\text{subepithelial}}$ value becomes coincidentally close to Q_{villi}, but it is significantly smaller than $Q_{\text{villi}}/f_{\text{u1}}$. This could be a possible reason why $f_{\text{u1}} = 1$ operationally resulted in a better prediction in the Q_{gut} model (as PS_{baso} limited drugs are minor in the validation data set).

Another discrepancy in the Q_{gut} model is that it suggests the existence of positive food effects via Fg increase. The Q_{gut} model suggests that the Fg would be affected by the change of Q_{villi}. Food intake increases the enteric blood flow by 100% (Fig. 6.23). Therefore, if the Q_{gut} model is correct, a positive food effect is anticipated for lipophilic drugs with high Fg. However, this contradicts the experimental observations (Section 12.2.2.2). These two contradictions in the Q_{gut} model can be solved by the anatomical Fg model. As $\text{CL}_{\text{subepithelial}}$ is close to Q_{villi} for $f_{\text{up}} \ll 0.05$, the Q_{gut} model (with $f_{\text{u1}} = 1$) and the anatomical model give similar Fg value. In addition, because CYP3A4 substrate tends to have low f_{up} and high permeability, the anatomical Fg model can be simplified to the Kato Fg model, which uses a constant $\text{CL}_{\text{esc,int}}$ value (5.7 ml/min/kg for humans).

The key difference between the Q_{gut} model and the anatomical Fg model is the method to calculate $\text{CL}_{\text{esc,int}}$. To directly compare the Q_{gut} and anatomical models with the experimental $\text{CL}_{\text{esc,int}}$, the Fg was converted to $\text{CL}_{\text{esc,int}}$ as

$$\text{CL}_{\text{esc,int}} = \frac{\text{Fg} \cdot \text{CL}_{\text{met,int}}}{1 - \text{Fg}} \tag{4.100}$$

$\text{CL}_{\text{met,int}}$ was obtained from the *in vitro* human intestinal microsome assay. Because this data is collected from various literature, it was normalized to that of midazolam (6.2 ml/min/kg) (Table 4.1). Figure 4.29 shows the comparison between the Q_{gut} and anatomical models for $\text{CL}_{\text{esc,int}}$ prediction. Even though $f_{\text{up}} = f_{\text{u1}}$ was suggested to be theoretically more appropriate, if $f_{\text{up}} = f_{\text{u1}}$ is used, the Q_{gut} model largely overestimated $\text{CL}_{\text{esc,int}}$, whereas the operational assumption $f_{\text{u1}} = 1$ gave better prediction. This is in good agreement with the previous findings by Yang et al. By the Q_{gut} ($f_{\text{u1}} = 1$) model, $\text{CL}_{\text{esc,int}}$ of many lipophilic drugs becomes a constant value ($= Q_{\text{villi}}$) value so that it becomes close to Kato's simple model. The anatomical Fg model can capture the f_{up} dependency of $\text{CL}_{\text{esc,int}}$ (Fig. 4.29c).

4.10.4 Interplay between CYP3A4 and P-gp

Recently, an interplay between CYP3A4 and P-gp has been proposed [87, 88]. This point is interesting because these enzymes have overlapping

TABLE 4.1 Clinical Fg, $CL_{int,met}$, and Predicted $CL_{esc,int}$

									Predicted (ml/min/kg)		$CL_{esc,int}$	Predicted Fg			References	
Drug	MW	$\log P_{oct}$	pK_a	Acid/ Base	f_{up}	$CL_{int,met}$ (*In Vitro*)	Fg (obs.)	$CL_{esc,int}$ (obs.)	Q_{gut} (f_{u1} = f_{up})	Q_{gut} (f_{u1} = f_{up})	Anatomical Model	Q_{gut} (f_{u1} = f_{up})	Q_{gut} (f_{u1} = f_{up})	Anatomical Model	Fg	$CL_{int,met}$
Alfentanil	417	2.4	6.3	B	0.093	0.87	0.61	1.33	2.7	29	1.7	0.76	0.97	0.66	97	86
Alprazolam	308	4.9	2.6	B	0.300	0.00	0.92	—	4.2	14	1.4	1.00	1.00	1.00	97	85
Amlodipine	408	3.7	8.9	B	0.005	0.50	0.88	3.71	2.3	452	4.0	0.82	1.00	0.89	85	85
Atorvastatin	558	4.4	4.2	A	0.005	0.25	0.40	0.17	0.0	8	0.0	0.14	0.97	0.14	97	86
Buspirone	386	2.5	7.6	B	0.050	2.96 (1.98–3.95)	0.16	0.56	2.5	50	2.1	0.46	0.94	0.42	97	86, 98
Carbamazepine	236	0.8	—	—	0.250	<0.55	1.00	—	3.8	15	1.6	0.88	0.97	0.75	98	98
Cisapride	465	3.3	7.8	B	0.020	2.59 (2.50–2.67)	0.55	3.16	2.6	130	3.3	0.50	0.98	0.56	97	86, 98
Clonazepam	315	2.5	—	—	0.150	0.00	0.93	—	3.9	26	1.8	1.00	1.00	1.00	85	85
Cyclosporine	1203	3.5	—	—	0.068	1.14 (0.36–1.91)	0.55	1.36	0.0	0	0.0	0.01	0.24	0.01	97	86, 98
Diazepam	285	2.9	3.4	B	0.023	<0.55	1.00	—	4.1	179	5.8	0.88	1.00	0.91	98	98
Diltiazem	415	3.2	8.0	B	0.180	0.73	0.91	7.38	2.8	15	1.3	0.79	0.95	0.64	98	98
Felodipine	383	4.5	—	—	0.004	23.90 (21.34–26.47)	0.49	22.97	4.2	1162	30.6	0.15	0.98	0.56	97	86, 98
Lovastatin	404	4.5	—	—	0.050	54.81 (44.49–65.13)	0.07	4.13	4.2	84	3.2	0.07	0.60	0.05	97	86, 98
Methadone	309	4.2	9.0	B	0.210	0.07	0.82	0.29	3.8	18	1.6	0.98	1.00	0.96	97	86
Midazolam	325	3.2	5.9	B	0.035	6.20	0.54	7.13	4.1	117	4.2	0.40	0.95	0.40	97	85, 86, 98
Nicardipine	479	4.3	7.1	B	0.005	53.31 (44.76–61.85)	0.64	94.77	4.1	810	19.1	0.07	0.94	0.26	98	85
Nifedipine	346	4.5	—	—	0.050	2.44 (1.73–3.60)	0.70	5.70	4.2	84	3.3	0.63	0.97	0.57	97	85, 86, 98
Nimodipine	418	2.7	—	—	0.016	15.77	0.64	28.04	3.3	204	5.1	0.17	0.93	0.24	98	98

(*Continued*)

TABLE 4.1 (*Continued*)

Drug	MW	log P_{oct}	pK_a	Acid/ Base	f_{up}	$CL_{int,met}$ (*In Vitro*)	Fg (obs.)	$CL_{esc,int}$ (obs.)	Predicted (ml/min/kg) $CL_{esc,int}$ Q_{gut} (f_{u1} = f_{up})	Q_{gut} (f_{u1} = f_{up})	Anatomical Model	Predicted Fg Q_{gut} (f_{u1} = f_{up})	Q_{gut} (f_{u1} = f_{up})	Anatomical Model	References Fg	References $CL_{int,met}$
Nisoldipine	388	3.1	—	—	0.003	69.93	0.28	26.53	3.9	1296	21.9	0.05	0.95	0.24	97	86
Nitrendipine	360	4.5	—	—	0.020	6.72	0.44	5.28	4.2	209	6.5	0.38	0.97	0.49	98	98
Quinidine	324	2.9	8.6	B	0.260	<0.27 (0.00–0.55)	0.91	—	2.5	10	1.2	0.90	0.97	0.81	97	85, 98
Repaglinide	452	5.9	3.9	A	0.015	0.43	0.89	3.48	1.3	89	1.6	0.76	1.00	0.79	97	86
Rifabutin	846	3.2	6.5	B	0.070	0.47	0.21	0.13	0.1	2	0.1	0.23	0.81	0.22	97	86
Sildenafil	474	4.5	9.2	B	0.040	1.02	0.68	2.17	2.1	52	1.9	0.67	0.98	0.65	97	86
Simvastatin	418	4.7	—	—	0.020	59.98 (56.50–63.46)	0.14	9.76	4.2	209	6.4	0.07	0.78	0.10	97	85, 86, 98
Tacrolimus	803	3.3	—	—	0.010	15.60 (12.04–19.16)	0.14	2.54	0.3	21	0.3	0.02	0.58	0.02	97	85, 86
Terfenadine	472	5.6	9.9	B	0.003	30.09	0.40	20.06	2.8	945	7.1	0.09	0.97	0.19	97	86
Trazodone	372	3.5	7.5	B	0.070	0.22	0.83	1.05	4.0	57	2.5	0.95	1.00	0.92	97	86
Triazolam	342	5.5	—	—	0.150	<0.55	0.70	—	4.2	28	1.8	0.88	0.98	0.77	97	98
Verapamil	455	4.2	9.1	B	0.093	4.01 (2.15–6.23)	0.65	7.45	2.0	22	1.4	0.33	0.84	0.25	97	85, 86, 98
Zolpidem	307	2.5	6.4	B	0.050	0.02	0.79	0.08	3.9	78	3.1	0.99	1.00	0.99	97	86

Indinavir and saquinavir were excluded from the analysis, as they have low K_m for CP3A4 (<1 μM) and saturation of CYP3A4 was suggested [65].

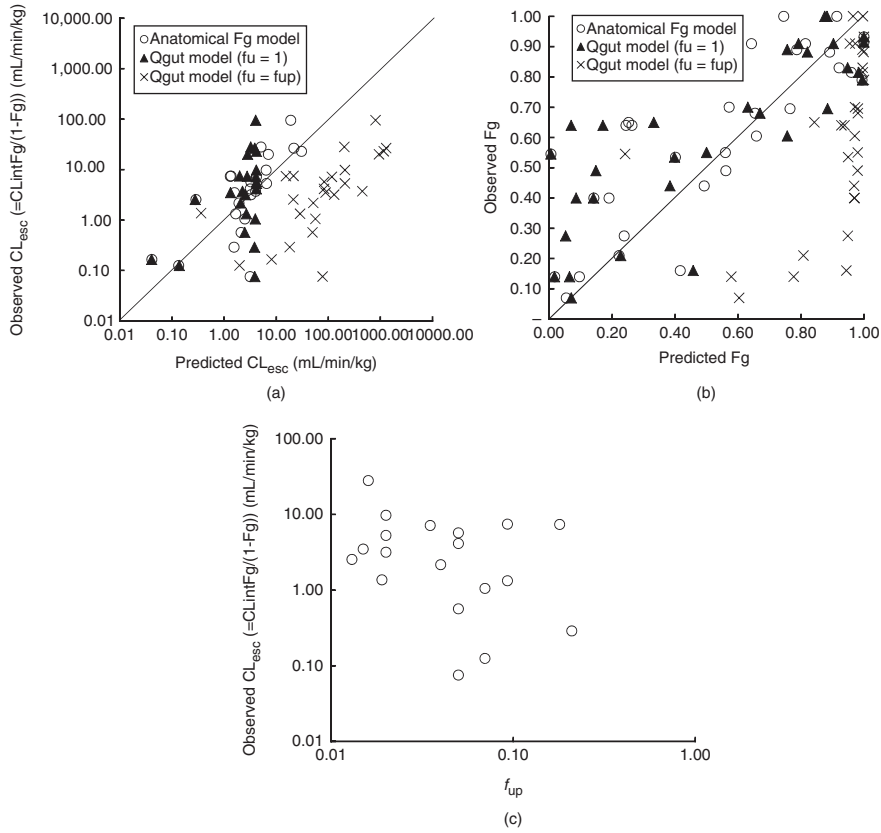

Figure 4.29 Comparison of (a) $CL_{esc,int}$ and (b) Fg predictability of the Q_{gut} and anatomical models. The relationship between $CL_{esc,int}$ and f_{up} is shown in (c). $Q_{villi} = 4.2$ ml/min/kg, $h_{subepithelial} = 0.0005$ cm, $A_{villi} = 126$ cm^2/ kg, $A_{vein} = 1.43$ cm^2/ kg, $D_{albumin} = 0.66 \times 10^{-6}$ cm^2/s, and $PS_{baso,int} = f_{n1} \times P_{trans,0} \times (a_0 a_2/(a_0 + a_2))/A_{well} \times a_2 \times A_{villi}$. $P_{trans,0}$ was calculated from experimental log P_{oct} and MW using Equation 4.35.

substrates. However, the definition of "interplay" has not been explicitly defined and there are controversies in the interpretation of experimental data. Recently, Fan and coworkers [89] performed a fully numerical simulation using a three-compartment model to solve the controversy. Here, we discuss this point using the steady-state solutions. The results from the full numerical simulation and the steady-state analytical solution are essentially the same, but the latter would be easier for interpretation and suitable for a book like this.

As discussed above, Fg is determined as the ratio of metabolic clearance and escaping clearance (Fig. 4.28). Therefore, if both processes are concentration-linear, P-gp in the apical membrane does not affect Fg and there is no interplay between P-gp and CYP3A4 on Fg. However, it is not the case when the metabolic clearance is saturable.

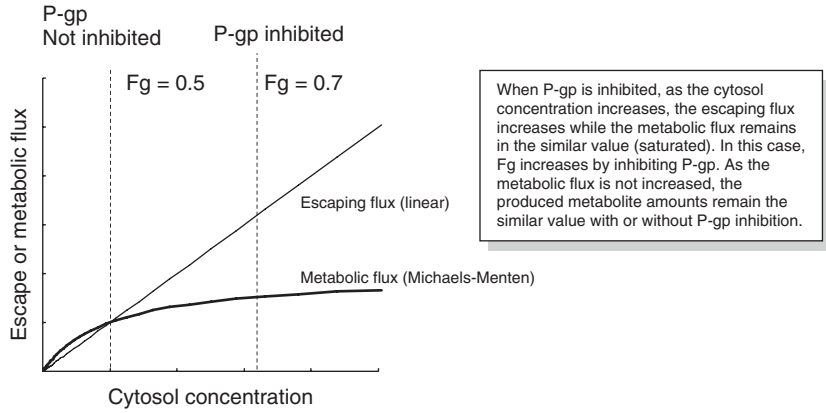

Figure 4.30 Relationship between escape flux, metabolic flux, and cytosol concentration.

We start with the similar equation for an efflux transporter. The mass balance in the cytosol at steady state can be described as:

$$\frac{dM_1}{dt} = C_0 f_{n0} f_{u0} a_0 p_{01} - C_1 f_{n1} f_{u1} a_0 p_{10} - C_1 f_{u1} a_0 p_{efflux} - C_1 f_{n1} f_{u1} a_2 p_{12} + C_2 f_{n2} f_{u2} a_2 p_{21} - \frac{V_{max,met} C_1 f_{u1}}{K_{m,met} + C_1 f_{u1}} \quad (4.101)$$

An apical membrane efflux (first order) was added and the saturable process was amended to metabolic clearance ($CL_{met,int} = V_{max,met}/(C_1 f_{u1} + K_{m,met})$). This equation can be solved for $C_1 f_{n1}$ as a quadratic equation and substituted in Equation 4.69.

$$P_{app,ep,A-B} = \frac{1}{C_0 A_{well}} [a_0 p_{01} f_{n0} C_0 - (C_1 f_{u1})(a_0 p_{10} f_{n1} - a_0 p_{efflux} f_{n1})] \quad (4.102)$$

Figure 4.30 shows the cytosol concentration dependency of escape and metabolic flux. When an apical efflux transporter is inhibited, the cytosol concentration increases and the escape flux[26] increases proportionally (as it follows the first-order kinetics). When $f_{u1} C_0 \ll K_{m,met}$, the metabolic flux also increases proportionally (hence, Fg remains constant). However, for a nonlinear case ($f_{u1} C_0 \approx K_{m,met}$ or above), metabolic flux increases subproportionally. Therefore, Fg is increased.

The effect of an efflux transporter on Fg might be observed even when a reduction of Fa by the efflux transporter was not significant. In Figure 4.31, $P_{ep} > 10 \times 10^{-6}$ cm/s and Fa% is > 99% across the concentration range.

[26]Should not be confused with clearance.

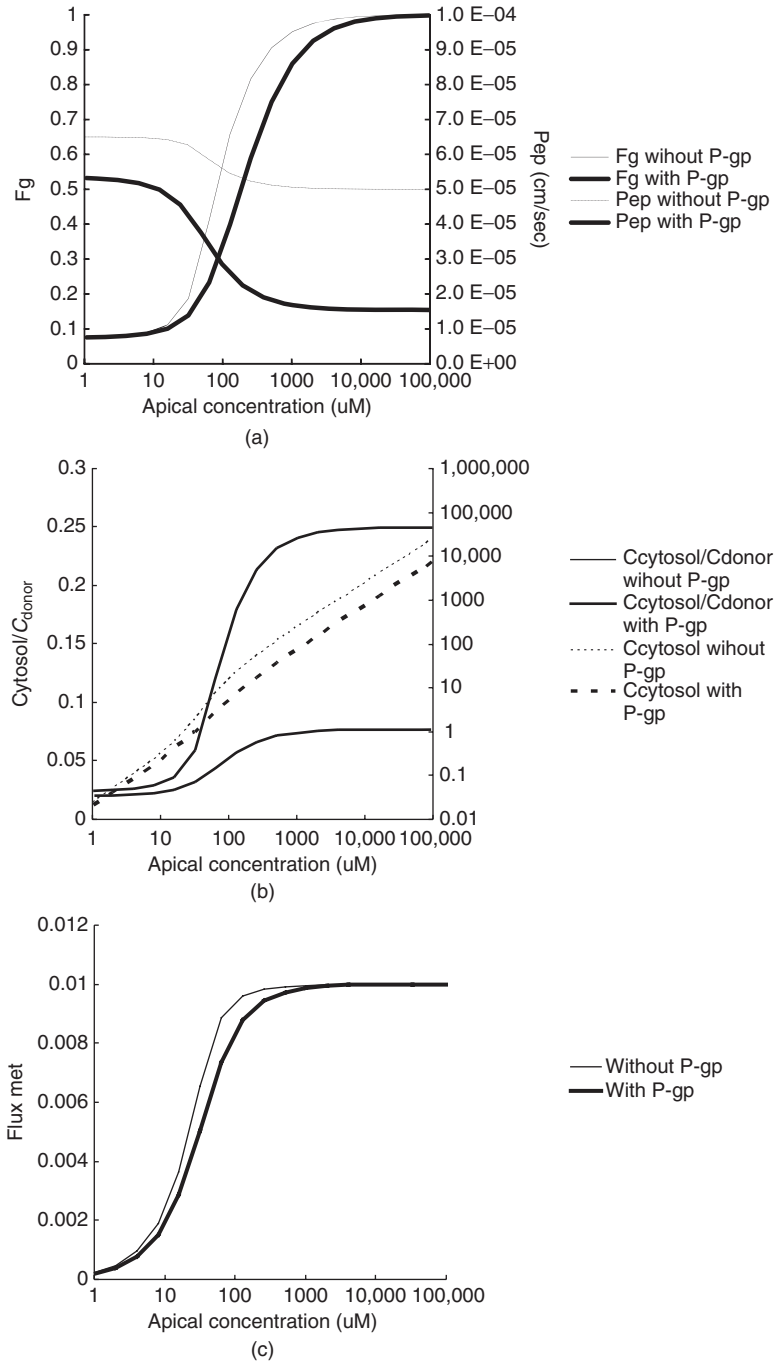

Figure 4.31 Concentration dependency of (a) Fg, P_{ep}; (b) cytosol concentration; and (c) metabolic flux. $P_{trans} = 5 \times 10^{-5}$ cm/s, $p_{efflux} = p_{PD} \times 10$, and $K_{m,met} = 1$ μM.

The effect of P-gp on the metabolic rate has been mainly investigated using CYP3A4-expressing Caco-2 cells [90–92]. When P-gp was inhibited, Fg was found to be increased. At the same time, the generated metabolite amount was slightly increased (due to a slight increase in metabolic flux by the increase in the cytosol concentration). This is in good agreement with the theoretical results.

Interestingly, it was theoretically suggested that P_{ep} would also show concentration dependency, even though the P-gp efflux was assumed linear. This occurs due to the change in the unbound drug concentration in the cytosol by metabolism. As the metabolic clearance is saturated, the unbound drug concentration in the cytosol increases, and therefore, the concentration gradient across the apical membrane is reduced, resulting in lower P_{ep} (cf. P_{ep} is the macroscopic permeability corresponding to the concentration reduction rate in the apical side[27] but not to the intrinsic permeability of each membrane (p_{01} and p_{10} are constant)).

4.11 HEPATIC METABOLISM AND EXCRETION

Hepatic first-pass metabolism often has significant impact on BA%. The following equation is often used to calculate the fraction of a drug that passes through the liver.

$$\mathrm{Fh} = 1 - \frac{\mathrm{CL_h}}{Q_h} \tag{4.103}$$

$\mathrm{CL_h}$ can be obtained from i.v. data. Figure 4.32 shows the relationship between $\mathrm{CL_h}$ and BA% in humans for marketed drugs [93]. When $\mathrm{Fa} = \mathrm{Fg} = 1, \mathrm{BA\%} = \mathrm{Fh} = 1 - \mathrm{CL_h}/Q_h$.

Hepatic metabolic clearance can be predicted from the *in vitro* assays such as S9, microsome, and hepatocyte assays. These assays can be performed with or without coexistence of plasma protein. In many cases, the intrinsic clearance (clearance of unbound drug) is used for *in vivo* CL prediction. The well-stirred model is most often used for CL prediction from *in vitro* data.

$$\mathrm{CL_h} = \frac{Q_h \cdot f_{up} \cdot \mathrm{CL_{int}}}{Q_h + f_{up} \cdot \mathrm{CL_{int}}} \tag{4.104}$$

Recently, there have been extensive investigations for more mechanistic approaches to predict $\mathrm{CL_h}$, explicitly incorporating the canalicular and sinusoidal transporters [94–96].

[27]In *in vitro* assays, P_{app} is usually calculated from the appearance rate in the acceptor chamber assuming that appearance rate equals the concentration reduction rate in the apical side. But this is not valid when the metabolic degradation occurs in the cytosol. If extensive metabolism occurs in the cytosol, the appearance rate could be small even when the disappearance rate in the apical side is fast. Fa corresponds to the appearance rate in the cytosol (before metabolism) and is equal to the disappearance rate.

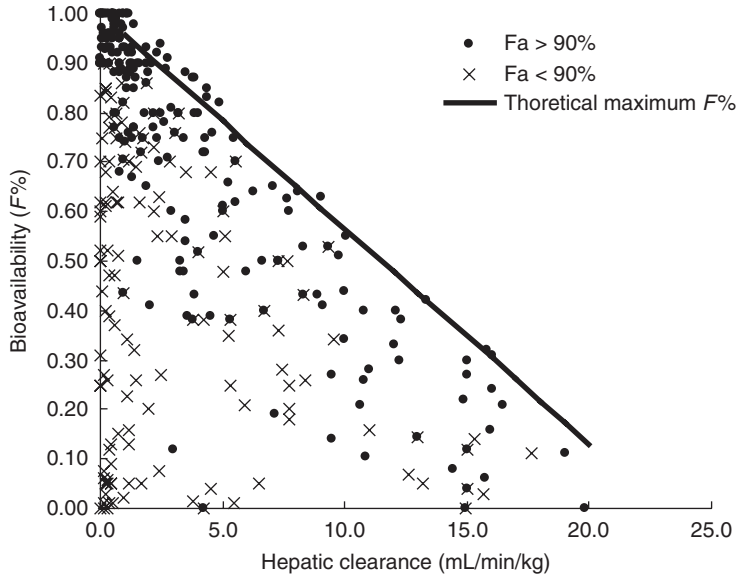

Figure 4.32 Bioavailability and CL_h in humans. *Source:* Replotted from Reference 93.

REFERENCES

1. Amidon, G.E., Higuchi, W.I., Ho, N.F.H. (1982). Theoretical and experimental studies of transport of micelle-solubilized solutes. *J. Pharmaceut. Sci*., 71, 77–84.
2. Sugano, K. (2009). Estimation of effective intestinal membrane permeability considering bile-micelle solubilisation. *Int. J. Pharm*., 368, 116–122.
3. Oliver, R.E., Jones, A.F., Rowland, M. (1998). What surface of the intestinal epithelium is effectively available to permeating drugs? *J. Pharmaceut. Sci*., 87, 634–639.
4. Lennernaes, H. (2007). Intestinal permeability and its relevance for absorption and elimination. *Xenobiotica*, 37, 1015–1051.
5. Yamaguchi, T., Ikeda, C., Sekine, Y. (1986). Intestinal absorption of a b-adrenergic blocking agent nadolol. I. Comparison of absorption behavior of nadolol with those of other b-blocking agents in rats. *Chem. Pharmaceut. Bull*., 34, 3362–3369.
6. Yamaguchi, T., Ikeda, C., Sekine, Y. (1986). Intestinal absorption of a b-adrenergic blocking agent nadolol. II. Mechanism of the inhibitory effect on the intestinal absorption of nadolol by sodium cholate in rats. *Chem. Pharmaceut. Bull*., 34, 3836–3843.
7. Yamaguchi, T., Oida, T., Ikeda, C., Sekine, Y. (1986). Intestinal absorption of a b-adrenergic blocking agent nadolol. III. Nuclear magnetic resonance spectroscopic study on nadolol-sodium cholate micellar complex and intestinal absorption of nadolol derivatives in rats. *Chem. Pharmaceut. Bull*., 34, 4259–4264.
8. Poelma, F.G.J., Breaes, R., Tukker, J.J. (1990). Intestinal absorption of drugs. III. The influence of taurocholate on the disappearance kinetics of hydrophilic and lipophilic drugs from the small intestine of the rat. *Pharmaceut. Res*., 7, 392–397.

9. Poelma, F.G.J., Breas, R., Tukker, J.J., Crommelin, D.J.A. (1991). Intestinal absorption of drugs. The influence of mixed micelles on the disappearance kinetics of drugs from the small intestine of the rat. *J. Pharm. Pharmacol*., 43, 317–324.
10. Lennernaes, H., Regaardh, C.G. (1993). Evidence for an interaction between the b-blocker pafenolol and bile salts in the intestinal lumen of the rat leading to dose-dependent oral absorption and double peaks in the plasma concentration-time profile. *Pharmaceut. Res*., 10, 879–883.
11. Ingels, F., Beck, B., Oth, M., Augustijns, P. (2004). Effect of simulated intestinal fluid on drug permeability estimation across Caco{-}2 monolayers. *Int. J. Pharm*., 274, 221–232.
12. Nilsson, D., Fagerholm, U., Lennernas, H. (1994). The influence of net water absorption on the permeability of antipyrine and levodopa in the human jejunum. *Pharmaceut. Res*., 11, 1540–1544.
13. Pappenheimer, J.R. (2001). Role of pre-epithelial "unstirred" layers in absorption of nutrients from the human jejunum. *J. Membr. Biol*., 179, 185–204.
14. Li, C.-Y., Zimmerman, C.L., Wiedmann, T.S. (1996). Diffusivity of bile salt/phospholipid aggregates in mucin. *Pharmaceut. Res*., 13, 535–541.
15. Sugano, K. (2010). Possible reduction of effective thickness of intestinal unstirred water layer by particle drifting effect. *Int. J. Pharm*., 387, 103–109.
16. Doyle-McCullough, M., Smyth, S.H., Moyes, S.M., Carr, K.E. (2007). Factors influencing intestinal microparticle uptake *in vivo*. *Int. J. Pharm*., 335, 79–89.
17. Hodges, G.M., Carr, E.A., Hazzard, R.A., Carr, K.E. (1995). Uptake and translocation of microparticles in small intestine. Morphology and quantification of particle distribution. *Dig. Dis. Sci*., 40, 967–975.
18. Limpanussorn, J., Simon, L., Dayan, A.D. (1998). Transepithelial transport of large particles in rat: a new model for the quantitative study of particle uptake. *J. Pharm. Pharmacol*., 50, 753–760.
19. Norris, D.A., Puri, N., Sinko, P.J. (1998). The effect of physical barriers and properties on the oral absorption of particulates. *Adv. Drug Delivery Rev*., 34, 135–154.
20. Smyth, S.H., Feldhaus, S., Schumacher, U., Carr, K.E. (2008). Uptake of inert microparticles in normal and immune deficient mice. *Int. J. Pharm*., 346, 109–118.
21. Allen, A., Flemstroem, G. (2005). Gastroduodenal mucus bicarbonate barrier: Protection against acid and pepsin. *Am. J. Physiol*., 288, C1–C19.
22. Atuma, C., Strugala, V., Allen, A., Holm, L. (2001). The adherent gastrointestinal mucus gel layer: thickness and physical state *in vivo*. *Am. J. Physiol*., 280, G922–G929.
23. Sugano, K. (2011). Fraction of a dose absorbed estimation for structurally diverse low solubility compounds. *Int. J. Pharm*., 405, 79–89.
24. Sugano, K., Nabuchi, Y., Machida, M., Asoh, Y. (2004). Permeation characteristics of a hydrophilic basic compound across a bio-mimetic artificial membrane. *Int. J. Pharm*., 275, 271–278.
25. Fischer, H., Kansy, M., Avdeef, A., Senner, F. (2007). Permeation of permanently positive charged molecules through artificial membranes influence of physico-chemical properties. *Eur. J. Pharmaceut. Sci*., 31, 32–42.
26. Walter, A., Gutknecht, J. (1984). Monocarboxylic acid permeation through lipid bilayer membranes. *J. Membr. Biol*., 77, 255–264.

27. Diamond, J.M., Katz, Y. (1974). Interpretation of nonelectrolyte partition coefficients between dimyristoyl lecithin and water. *J. Membr. Biol*., 17, 121–154.

28. Xiang, T., Xu, Y., Anderson, B.D. (1998). The barrier domain for solute permeation varies with lipid bilayer phase structure. *J. Membr. Biol*., 165, 77–90.

29. Mayer, P.T., Xiang, T.X., Anderson, B.D. (2000). Independence of substituent contributions to the transport of small molecule permeants in lipid bilayers. *AAPS PharmSci [Electronic Resource]*, 2, E14.

30. Mayer, P.T., Anderson, B.D. (2002). Transport across 1,9-decadiene precisely mimics the chemical selectivity of the barrier domain in egg lecithin bilayers. *J. Pharmaceut. Sci*., 91, 640.

31. Walter, A., Gutknecht, J. (1986). Permeability of small nonelectrolytes through lipid bilayer membranes. *J. Membr. Biol*., 90, 207–217.

32. Burton, P. S., Conradi, R.A., Hilgers, A.R. (1991). Mechanisms of peptide and protein absorption. (2). Transcellular mechanism of peptide and protein absorption: passive aspects. *Adv. Drug Deliv. Rev*., 7, 365–386.

33. Eytan, G.D., Kuchel, P.W. (1999). Mechanism of action of P-glycoprotein in relation to passive membrane permeation. *Int. Rev. Cytol*., 190, 175–250.

34. Regev, R., Eytan, G.D. (1997). Flip-flop of doxorubicin across erythrocyte and lipid membranes. *Biochem. Pharmacol*., 54, 1151–1158.

35. Kamp, F., Zakim, D., Zhang, F., Noy, N., Hamilton, J.A. (1995). Fatty acid flip-flop in phospholipid bilayers is extremely fast. *Biochemistry*, 34, 11928–11937.

36. Kleinfeld, A.M., Chu, P., Storch, J. (1997). Flip-flop is slow and rate limiting for the movement of long chain anthroyloxy fatty acids across lipid vesicles. *Biochemistry*, 36, 5702–5711.

37. Avdeef, A., Artursson, P., Neuhoff, S., Lazorova, L., Grasjo, J., Tavelin, S. (2005). Caco{-}2 permeability of weakly basic drugs predicted with the double-sink PAMPA pKa(flux) method. *Eur. J. Pharmaceut. Sci*., 24, 333–349.

38. Yamashita, S., Furubayashi, T., Kataoka, M., Sakane, T., Sezaki, H., Tokuda, H. (2000). Optimized conditions for prediction of intestinal drug permeability using Caco{-}2 cells. *Eur. J. Pharmaceut. Sci*., 10, 195–204.

39. Lee, K.J., Johnson, N., Castelo, J., Sinko, P.J., Grass, G., Holme, K., Lee, Y.H. (2005). Effect of experimental pH on the *in vitro* permeability in intact rabbit intestines and Caco{-}2 monolayer. *Eur. J. Pharmaceut. Sci*., 25, 193–200.

40. Avdeef, A. (2011). How well can *in vitro* brain microcapillary endothelial cell models predict rodent *in vivo* blood-brain barrier permeability? *Eur. J. Pharmaceut. Sci*., 43, 109–124.

41. Dagenais, C., Avdeef, A., Tsinman, O., Dudley, A., Beliveau, R. (2009). P-glycoprotein deficient mouse *in situ* blood-brain barrier permeability and its prediction using an in combo PAMPA model. *Eur. J. Pharmaceut. Sci*., 38, 121–137.

42. Camenisch, G., Alsenz, J., van de Waterbeemd, H., Folkers, G. (1998). Estimation of permeability by passive diffusion through Caco{-}2 cell monolayers using the drugs' lipophilicity and molecular weight. *Eur. J. Pharmaceut. Sci*., 6, 313–319.

43. Adson, A., Burton, P.S., Ruab, T.J., Barsuhn, C.L., Audus, L., Ho, N.F.H. (1995). Passive diffusion of weak organic electrolytes across Caco{-}2 cell monolayers: Uncoupling the contributions of hydrodynamic, transcellular and paracellular barriers. *Pharmaceut. Res*., 84, 1197–1203.

44. Adson, A., Ruab, T.J., Burton, P.S., Barsuhn, C.L., Hilgers, A.R., Audus, K.L., Ho, N.F.H. (1994). Quantitative approaches to delineate paracellular diffusion in cultured epithelial cell monolayers. *J. Pharmaceut. Sci*., 83, 1529–1530.

45. Sugano, K., Nabuchi, Y., Machida, M., Aso, Y. (2003). Prediction of human intestinal permeability using artificial membrane permeability. *Int. J. Pharm*., 257, 245–251.

46. Sugano, K., Takata, N., Machida, M., Saitoh, K., Terada, K. (2002). Prediction of passive intestinal absorption using bio-mimetic artificial membrane permeation assay and the paracellular pathway model. *Int. J. Pharm*., 241, 241–251.

47. Sugano, K., Obata, K., Saitoh, R., Higashida, A., Hamada, H., Processing of Biopharmaceutical Profiling Data in Drug Discovery, in: B. Testa, S. Krämer, H. Wunderli-Allenspach, G. Folkers (Eds.) Pharmacokinetic Profiling in Drug Research, Wiley-VCH, Zurich, 2006, pp. 441–458.

48. Obata, K., Sugano, K., Saitoh, R., Higashida, A., Nabuchi, Y., Machida, M., Aso, Y. (2005). Prediction of oral drug absorption in humans by theoretical passive absorption model. *Int. J. Pharm*., 293, 183–192.

49. Avdeef, A. (2010). Leakiness and size exclusion of paracellular channels in cultured epithelial cell monolayers-interlaboratory comparison. *Pharmaceut. Res*., 27, 480–489.

50. Reynolds, D.P., Lanevskij, K., Japertas, P., Didziapetris, R., Petrauskas, A. (2009). Ionization-specific analysis of human intestinal absorption. *J. Pharmaceut. Sci*., 98, 4039–4054.

51. Karlsson, J., Ungell, A.l., Grasjo, J., Artursson, P. (1999). Paracellular drug transport across intestinal epithelia: influence of charge and induced water flux. *Eur. J. Pharmaceut. Sci*., 9, 47–56.

52. Deen, W.M. (1987). Hindered transport of large molecules in liquid-filled pores. *AIChE Journal*, 33, 1409–1425.

53. Sugano, K., Yoshida, S., Takaku, M., Haramura, M., Saitoh, R., Nabuchi, Y., Ushio, H. (2000). Quantitative structure-intestinal permeability relationship of benzamidine analogue thrombin inhibitor. *Bioorg. Med. Chem. Lett*., 10, 1939–1942.

54. Kristl, A., Tukker, J.J. (1998). Negative correlation of n-octanol/water partition coefficient and transport of some guanine derivatives through rat jejunum *in vitro*. *Pharmaceut. Res*., 15, 499–501.

55. Avdeef, A., Tam, K.Y. (2010). How well can the caco{-}2/madin-darby canine kidney models predict effective human jejunal permeability? *J. Med. Chem*., 53, 3566–3584.

56. He, Y., Murby, S., Warhurst, G., Gifford, L., Walker, D., Ayrton, J., Eastmond, R., Rowland, M. (1998). Species differences in size discrimination in the paracellular pathway refracted by oral bioavailability of poly(ethylene glycol) and D-peptides. *J. Pharmaceut. Sci*., 87, 626–633.

57. Knipp, T.G., Ho, N.F.H., Barsuhn, C.L., Borchardt, R.T. (1997). Paracellular diffusion in Caco{-}2 cell monolayers: effect of perturbation on the transport of hydrophilic compounds that vary in size and charge. *J. Pharmaceut. Sci*., 86, 1105–1110.

58. Garmire, L.X., Hunt, C.A. (2008). In silico methods for unraveling the mechanistic complexities of intestinal absorption: metabolism-efflux transport interactions. *Drug Metabol. Dispos*., 36, 1414–1424.

59. Garmire, L.X., Garmire, D.G., Hunt, C.A. (2007). An in silico transwell device for the study of drug transport and drug-drug interactions. *Pharmaceut. Res*., 24, 2171–2186.

60. Grant, M.R., Hunt, C.A. An in silico analogue of *in vitro* systems used to study epithelial cell morphogenesis, Computational Methods in Systems Biology, Springer, Berlin, Heidelberg, 2006, 285–297.

61. Liu, Y., Hunt, C.A. (2006). Mechanistic study of the cellular interplay of transport and metabolism using the synthetic modeling method. *Pharmaceut. Res*., 23, 493–505.

62. Liu, Y., Hunt, C.A. (2005). Studies of intestinal drug transport using an in silico epithelio-mimetic device. *BioSystems*, 82, 154–167.

63. Heikkinen, A.T., Moenkkoenen, J., Korjamo, T. (2010). Determination of permeation resistance distribution in *in vitro* cell monolayer permeation experiments. *Eur. J. Pharmaceut. Sci*., 40, 132–142.

64. Korjamo, T., Kemilainen, H., Heikkinen, A.T., Monkkonen, J. (2007). Decrease in intracellular concentration causes the shift in K_m value of efflux pump substrates. *Drug Metabol. Dispos*., 35, 1574–1579.

65. Gertz, M., Houston, J.B., Galetin, A. (2011). Physiologically based pharmacokinetic modeling of intestinal first-pass metabolism of CYP3A substrates with high intestinal extraction. *Drug Metabol. Dispos.: the biological fate of chemicals*, 39, 1633–1642.

66. Sugano, K., Shirasaka, Y., Yamashita, S., Velicky, M., Bradley, D.F., Tam, K.Y., Dryfe, R.A. (2011). Estimation of Michaelis-Menten constant of efflux transporter considering asymmetric permeability Fraction of a dose absorbed estimation for structurally diverse low solubility compounds *In Situ* artificial membrane permeation assay under hydrodynamic control: permeability-pH profiles of warfarin and verapamil. *Int. J. Pharm*., 8, 8.

67. Sugano, K., Kansy, M., Artursson, P., Avdeef, A., Bendels, S., Di, L., Ecker, G.F., Faller, B., Fischer, H., Gerebtzoff, G., Lennernaes, H., Senner, F. (2010). Coexistence of passive and carrier-mediated processes in drug transport. *Nat. Rev. Drug Discov*., 9, 597–614.

68. Trotter, P.J., Storch, J. (1991). Fatty acid uptake and metabolism in a human intestinal cell line (Caco{-}2): comparison of apical and basolateral incubation. *J. Lipid Res*., 32, 293–304.

69. Neuhoff, S., Ungell, A.L., Zamora, I., Artursson, P. (2005). pH-Dependent passive and active transport of acidic drugs across Caco{-}2 cell monolayers. *Eur. J. Pharmaceut. Sci*., 25, 211–220.

70. Troutman, M.D., Thakker, D.R. (2003). Novel experimental parameters to quantify the modulation of absorptive and secretory transport of compounds by p-glycoprotein in cell culture models of intestinal epithelium. *Pharmaceut. Res*., 20, 1210–1224.

71. Dahan, A., Amidon, G.L. (2009). Segmental dependent transport of low permeability compounds along the small intestine due to P-glycoprotein: the role of efflux transport in the oral absorption of BCS class III drugs. *Mol. Pharm*., 6, 19–28.

72. Collett, A., Tanianis-Hughes, J., Hallifax, D., Warhurst, G. (2004). Predicting P-glycoprotein effects on oral absorption: Correlation of transport in Caco{-}2 with drug pharmacokinetics in wild-type and mdr1a(-/-) mice *in vivo*. *Pharmaceut. Res*., 21, 819–826.

73. Varma, M. V., Sateesh, K., Panchagnula, R. (2005). Functional role of P-glycoprotein in limiting intestinal absorption of drugs: contribution of passive permeability to P-glycoprotein mediated efflux transport. *Mol. Pharm*., 2, 12–21.

74. Aller, S. G., Yu, J., Ward, A., Weng, Y., Chittaboina, S., Zhuo, R., Harrell, P.M., Trinh, Y.T., Zhang, Q., Urbatsch, I.L., Chang, G. (2009). Structure of P-glycoprotein reveals a molecular basis for poly-specific drug binding. *Science (Washington, DC, U. S.)*, 323, 1718–1722.

75. Varma, M.V., Panchagnula, R. (2005). Prediction of *in vivo* intestinal absorption enhancement on P-glycoprotein inhibition, from rat *in situ* permeability. *J. Pharmaceut. Sci*., 94, 1694–1704.

76. Horie, K., Tang, F., Borchardt, R.T. (2003). Isolation and characterization of caco{-}2 subclones expressing high levels of multidrug resistance protein efflux transporter. *Pharmaceut. Res*., 20, 161–168.

77. Shirasaka, Y., Sakane, T., Yamashita, S. (2008). Effect of P-glycoprotein expression levels on the concentration-dependent permeability of drugs to the cell membrane. *J. Pharmaceut. Sci*., 97, 553–565.

78. Petri, N., Tannergren, C., Rungstad, D., Lennernaes, H. (2004). Transport characteristics of fexofenadine in the caco{-}2 cell model. *Pharmaceut. Res*., 21, 1398–1404.

79. Troutman, M.D., Thakker, D.R. (2003). Efflux ratio cannot assess P-glycoprotein-mediated attenuation of absorptive transport: Asymmetric effect of P-glycoprotein on absorptive and secretory transport across Caco{-}2 cell monolayers. *Pharmaceut. Res*., 20, 1200–1209.

80. Balakrishnan, A., Hussainzada, N., Gonzalez, P., Bermejo, M., Swaan, P.W., Polli, J.E. (2007). Bias in estimation of transporter kinetic parameters from overexpression systems: Interplay of transporter expression level and substrate affinity. *J. Pharmacol. Exp. Ther*., 320, 133–144.

81. Winne, D. (1973). Unstirred layer, source of biased Michaelis constant in membrane transport. *Biochim. Biophys. Acta*., 298, 27–31.

82. Kato, M. (2008). Intestinal first-pass metabolism of CYP3A4 substrates. *Drug Metab. Pharmacokinet*., 23, 87–94.

83. Yang, J., Jamei, M., Yeo, K.R., Tucker, G.T., Rostami-Hodjegan, A. (2007). Prediction of intestinal first-pass drug metabolism. *Curr. Drug Metabol*., 8, 676–684.

84. Fagerholm, U. (2008). Prediction of human pharmacokinetics-gut-wall metabolism. *J. Pharm. Pharmacol*., 59, 1335–1343.

85. Kadono, K., Akabane, T., Tabata, K., Gato, K., Terashita, S., Teramura, T. (2010). Quantitative prediction of intestinal metabolism in humans from a simplified intestinal availability model and empirical scaling factor. *Drug Metabol. Dispos.: the biological fate of chemicals*, 38, 1230–1237.

86. Gertz, M., Harrison, A., Houston, J.B., Galetin, A. (2010). Prediction of human intestinal first-pass metabolism of 25 CYP3A substrates from *in vitro* clearance and permeability data. *Drug Metabol. Dispos.: the biological fate of chemicals*, 38, 1147–1158.

87. Cummins, C.L., Jacobsen, W., Benet, L. Z. (2002). Unmasking the dynamic interplay between intestinal P-glycoprotein and CYP3A4. *J. Pharmacol. Exp. Ther*., 300, 1036–1045.

88. Benet, L. Z., Cummins, C.L., Wu, C.Y. (2004). Unmasking the dynamic interplay between efflux transporters and metabolic enzymes. *Int. J. Pharm*., 277, 3–9.

89. Fan, J., Maeng, H.J., Pang, K.S. (2010). Interplay of transporters and enzymes in the Caco{-}2 cell monolayer: I. effect of altered apical secretion. *Biopharm. Drug Dispos*., 31, 215–227.

90. Fisher, J.M., Wrighton, S.A., Watkins, P.B., Schmiedlin-Ren, P., Calamia, J.C., Shen, D.D., Kunze, K.L., Thummel, K.E. (1999). First-pass midazolam metabolism catalyzed by 1alpha,25-dihydroxy vitamin D3-modified Caco{-}2 cell monolayers. *J. Pharmacol. Exp. Ther*., 289, 1134–1142.

91. Hochman, J.H., Chiba, M., Nishime, J., Yamazaki, M., Lin, J.H. (2000). Influence of P-glycoprotein on the transport and metabolism of indinavir in Caco{-}2 cells expressing cytochrome P{-}450 3A4. *J. Pharmacol. Exp. Ther*., 292, 310–318.

92. Raeissi, S.D., Hidalgo, I.J., Segura-Aguilar, J., Artursson, P. (1999). Interplay between CYP3A-mediated metabolism and polarized efflux of terfenadine and its metabolites in intestinal epithelial Caco{-}2 (TC7) cell monolayers. *Pharmaceut. Res*., 16, 625–632.

93. Varma, M. V., Obach, R.S., Rotter, C., Miller, H.R., Chang, G., Steyn, S.J., El-Kattan, A., Troutman, M.D. (2010). Physicochemical space for optimum oral bioavailability: contribution of human intestinal absorption and first-pass elimination. *J. Med. Chem*., 53, 1098–1108.

94. Kusuhara, H., Sugiyama, Y. (2010). Pharmacokinetic modeling of the hepatobiliary transport mediated by cooperation of uptake and efflux transporters. *Drug Metab. Rev*., 42, 539–550.

95. Watanabe, T., Kusuhara, H., Maeda, K., Kanamaru, H., Saito, Y., Hu, Z., Sugiyama, Y. (2010). Investigation of the rate-determining process in the hepatic elimination of HMG-CoA reductase inhibitors in rats and humans. *Drug Metabol. Dispos.: the biological fate of chemicals*, 38, 215–222.

96. Watanabe, T., Kusuhara, H., Sugiyama, Y. (2010). Application of physiologically based pharmacokinetic modeling and clearance concept to drugs showing transporter-mediated distribution and clearance in humans. *J. Pharmacokinet. Pharmacodyn*., 37, 575–590.

97. Galetin, A., Gertz, M., Houston, J.B. (2010). Contribution of intestinal cytochrome p450-mediated metabolism to drug-drug inhibition and induction interactions. *Drug Metabol. Pharmacokinet*., 25, 28–47.

98. Nishimuta, H., Sato, K., Mizuki, Y., Yabuki, M., Komuro, S. (2010). Prediction of the intestinal first-pass metabolism of CYP3A substrates in humans using cynomolgus monkeys. *Drug Metabol. Dispos.: the biological fate of chemicals*, 38, 1967–1975.